Pattern Identification and Analysis in Urban Flows

by

Brent Knutson

A Dissertation Presented in Partial Fulfillment
of the Requirements for the Degree
Doctor of Philosophy

Approved November 2018 by the
Graduate Supervisory Committee:

Wenbo Tang, Chair
Ronald Calhoun
Huei-Ping Huang
Eric Kostelich
Alex Mahalov

ARIZONA STATE UNIVERSITY

December 2018

ABSTRACT

Two urban flows are analyzed, one concerned with pollutant transport in a Phoenix, Arizona neighborhood and the other with windshear detection at the Hong Kong International Airport (HKIA).

Lagrangian measures, identified with finite-time Lyapunov exponents, are first used to characterize transport patterns of inertial pollutant particles. Motivated by actual events the focus is on flows in realistic urban geometry. Both deterministic and stochastic transport patterns are identified, as inertial Lagrangian coherent structures. For the deterministic case, the organizing structures are well defined and are extracted at different hours of a day to reveal the variability of coherent patterns. For the stochastic case, a random displacement model for fluid particles is formulated, and used to derive the governing equations for inertial particles to examine the change in organizing structures due to "zeroth-order" random noise. It is found that, (1) the Langevin equation for inertial particles can be reduced to a random displacement model; (2) using random noise based on inhomogeneous turbulence, whose diffusivity is derived from k-ϵ models, major coherent structures survive to organize local flow patterns and weaker structures are smoothed out due to random motion.

A study of three-dimensional Lagrangian coherent structures (LCS) near HKIA is then presented and related to previous developments of two-dimensional (2D) LCS analyses in detecting windshear experienced by landing aircraft. The LCS are contrasted among three independent models and against 2D coherent Doppler light detection and ranging (LIDAR) data. Addition of the velocity information perpendicular to the lidar scanning cone helps solidify flow structures inferred from previous studies; contrast among models reveals the intramodel variability; and comparison with flight data evaluates the performance among models in terms of

Lagrangian analyses. It is found that, while the three models and the LIDAR do recover similar features of the windshear experienced by a landing aircraft (along the landing trajectory), their Lagrangian signatures over the entire domain are quite different - a portion of each numerical model captures certain features resembling those LCS extracted from independent 2D LIDAR analyses based on observations. Overall, it was found that the Weather Research and Forecast (WRF) model provides the best agreement with the LIDAR data.

Finally, the three-dimensional variational (3DVAR) data assimilation scheme in WRF is used to incorporate the LIDAR line of sight velocity observations into the WRF model forecast at HKIA. Using two different days as test cases, it is found that the LIDAR data can be successfully and consistently assimilated into WRF. Using the updated model forecast LCS are extracted along the LIDAR scanning cone and compare to onboard flight data. It is found that the LCS generated from the updated WRF forecasts are generally better correlated with the windshear experienced by landing aircraft as compared to the LIDAR extracted LCS alone, which suggests that such a data assimilation scheme could be used for the prediction of windshear events.

ACKNOWLEDGMENTS

Thank you to all my teachers, classmates, family, and friends.

Thank you to Debbie Olsen and Joelle Park, for their help navigating the bureaucracy and deadlines.

Thank you to Dr. Dimitrova, for your help generating the Hermoso park flow data.

Thank you to H.J.S. Fernando, Lord J.C.R. Hunt, David Carruthers, and Andrew Ellis for the many helpful discussions.

Thank you to Dr. Chan, for being willing to review this dissertation, and for the data from HKIA and insights you've given me.

Thank you to Dr. Calhoun, Dr. Huang, Dr. Kostelich, and Dr. Mahalov, for being willing to be on my committee, and their time spent.

Thank you to Dr. Tang, whose patience and understanding were never exhausted throughout this long process. It is impossible to successfully put into words how much I appreciate all that you've done for me.

We acknowledge support from the National Science Foundation (NSF) (ATM-0934592).

TABLE OF CONTENTS

LIST OF TABLES

LIST OF FIGURES

Figure Page

Figure Page

Chapter 1

INTRODUCTION

Dynamical systems ideas provide a framework to understand the qualitative behavior of solutions of ordinary differential equations by identifying distinguished regions in the phase space, called manifolds, that serve to organize the evolution and behavior of solutions to the system. In the particular case where the vector field of interest is the velocity field of a fluid, the solutions are passive particle trajectories and the phase space is the actual physical space the fluid occupies. Hence, regions in the flow that organize the actual physical movement of the fluid are identified. A fundamental issue in trying to apply these ideas directly, however, is the fact that in applications the flow is usually only known over a finite time and domain, and so most dynamical systems ideas cannot be directly applied, as many of the key ideas depend on the asymptotic limit as time approaches infinity.

Hence an entirely new framework, motivated by, but apart from, classical dynamical systems has been developed and has become a very active area of research. These ideas are collectively and generically known as Lagrangian techniques or approaches, since in fluid mechanics the frame following fluid particles is known as the Lagrangian frame. This is in contrast to the Eulerian point of view, which analyzes the flow at fixed points in space. It is claimed, and sometimes has been established, that Lagrangian methods can be more accurate and insightful in certain cases than their Eulerian counterparts, since Lagrangian measures depend on the actual motion of fluid particles, rather than the inferred motion from Eulerian measures. Since many Lagrangian methods are newly developed, it is natural to compare to the more well

established and used Eulerian methods. As computing power has increased, and as the ideas have matured, Lagrangian techniques are starting to become more common.

The main idea of conceptual interest is that of the so called Lagrangian Coherent Structure (LCS), which are material curves or surfaces that separate regions in the flow that behave qualitatively different, over some period of time. In other words, LCS are the finite analog and generalization of manifolds seen in dynamical systems. The precise definition of, and best way to find, the LCS in a given flow is a problem that hasn't been completely settled yet; many methods have been proposed. In this work, we use the Finite Time Lyapunov Exponent (FTLE), which will be defined later, to find and identify LCS since we are concerned with the boundaries of regions that are responsible for pollutant transport and flight discomfort.

Our central thesis is this: we apply the LCS framework to understand flow and transport in high leverage situations involving potential impact to human health, safety, and activity. There is a dual purpose to this. First, we further the development of Lagrangian analysis with the application of the techniques. Secondly, Lagrangian analysis brings new perspectives to understand flow. We do this in two different geographical areas: an urban neighborhood in Phoenix, Arizona and the Hong Kong International Airport (HKIA).

In the first case, we study the geometry of pollutant particle transport in the Hermoso Park region of Phoenix. Since pollutants have mass and volume they behave dynamically differently than idealized fluid particles. Assuming a spherical shape, these inertial particle dynamics can be modeled using the Maxey-Riley equations (Maxey and Riley 1983). We study the transport of such particles in both deterministic and stochastic settings in Chapter 2, which is based on work found in (Tang et al. 2012).

Chapters 3 and 4 concern windshear detection for landing aircraft at HKIA. Due

to the close proximity of the airport to Lantau island terrain induced turbulence can cause issues with landing aircraft. In (Tang, Chan, and Haller 2011a, 2011b) an LCS based analysis was introduced, using line of site velocity data measured by LIDAR at HKIA to detect windshear events along the landing corridor. Analyzing a multitude of cases across different seasons, (Kafiabad, Chan, and Haller 2013) found that the developed LCS framework was comparable and competitive with the operational methods currently implemented at HKIA, which is noteworthy due to the fact that the operational scheme uses data from a multitude of different sources, whereas the Lagrangian detection scheme uses only LIDAR data. Furthermore, the LIDAR data is only given on a two-dimensional scanning cone, and so provides only partial information about air velocity. In Chapter 3, based on (Knutson, Tang, and Chan 2015), three-dimensional numerical models are used to validate such an approach. It was found that the Weather Research and Forecasting (WRF) model provided the best agreement with LIDAR data. In Chapter 4 we implement data assimilation of the LIDAR data into the WRF model, and explore how LCS windshear detection could possibly be improved.

1.1 Mathematical Background

In this section we introduce the basics of the finite time Lyapunov exponent.

Suppose that $\boldsymbol{v}(\boldsymbol{x}, t)$ is the velocity field of a fluid, defined on the time interval $[t_1, t_2]$. Let $\boldsymbol{x}(t; \boldsymbol{x}_0, t_0)$ denote the position of a fluid particle at time t that was originally at the point $\boldsymbol{x}_0$ at time t_0, and note that we thus have

$$\boldsymbol{x}'(t; \boldsymbol{x}_0, t_0) = \boldsymbol{v}(\boldsymbol{x}(t; \boldsymbol{x}_0, t_0), t), \tag{1.1}$$

where $t \in [t_1, t_2]$ so the above equation is defined and $'$ denotes differentiation with respect to t.

Define now the flow map, $\boldsymbol{F}_{t_0}^{t_0+T}$, by

$$\boldsymbol{F}_{t_0}^{t_0+T}(\boldsymbol{x}_0) \equiv \boldsymbol{x}(t_0+T; \boldsymbol{x}_0, t_0). \tag{1.2}$$

The flow map moves the fluid particle found at location $\boldsymbol{x}_0$ at time t_0 forward to its position at the time $t_0 + T$. By results from dynamical systems theory, if we assume that $\boldsymbol{v}$ is at least C^1 then $\boldsymbol{F}_{t_0}^{t_0+T}$ will be a diffeomorphism with inverse $\left(\boldsymbol{F}_{t_0}^{t_0+T}\right)^{-1} = \boldsymbol{F}_{t_0+T}^{t_0}$. Since both $\boldsymbol{F}_{t_0}^{t_0+T}$ and $\boldsymbol{F}_{t_0+T}^{t_0}$ are smooth, we can apply the chain rule to $\boldsymbol{F}_{t_0}^{t_0+T}\left(\boldsymbol{F}_{t_0+T}^{t_0}(\boldsymbol{x})\right) = \boldsymbol{x}$ to see that $\nabla \boldsymbol{F}_{t_0}^{t_0+T}$, the derivative of $\boldsymbol{F}_{t_0}^{t_0+T}$, is an invertible matrix and that

$$\left(\nabla \boldsymbol{F}_{t_0}^{t_0+T}(\boldsymbol{x}_0)\right)^{-1} = \nabla \boldsymbol{F}_{t_0+T}^{t_0}\left(\boldsymbol{F}_{t_0}^{t_0+T}(\boldsymbol{x}_0)\right). \tag{1.3}$$

Since $\boldsymbol{F}_{t_0}^{t_0+T}$ is differentiable, we have that

$$\boldsymbol{F}_{t_0}^{t_0+T}(\boldsymbol{x}_0+\boldsymbol{h}) - \boldsymbol{F}_{t_0}^{t_0+T}(\boldsymbol{x}_0) = \nabla \boldsymbol{F}_{t_0}^{t_0+T}(\boldsymbol{x}_0)\boldsymbol{h} + o(|\boldsymbol{h}|). \tag{1.4}$$

Using the above we can see how small perturbations are advected by the flow. Letting $*$ denote the transpose of a matrix, the square magnitude of the displacement is, to leading order,

$$\begin{aligned}
\left|\boldsymbol{F}_{t_0}^{t_0+T}(\boldsymbol{x}_0+\boldsymbol{h}) - \boldsymbol{F}_{t_0}^{t_0+T}(\boldsymbol{x}_0)\right|^2 &= \left\langle \boldsymbol{F}_{t_0}^{t_0+T}(\boldsymbol{x}_0+\boldsymbol{h}) - \boldsymbol{F}_{t_0}^{t_0+T}(\boldsymbol{x}_0), \boldsymbol{F}_{t_0}^{t_0+T}(\boldsymbol{x}_0+\boldsymbol{h}) - \boldsymbol{F}_{t_0}^{t_0+T}(\boldsymbol{x}_0)\right\rangle \\
&\approx \left\langle \nabla \boldsymbol{F}_{t_0}^{t_0+T}(\boldsymbol{x}_0)\boldsymbol{h}, \nabla \boldsymbol{F}_{t_0}^{t_0+T}(\boldsymbol{x}_0)\boldsymbol{h}\right\rangle \\
&= \left\langle \boldsymbol{h}, \left(\nabla \boldsymbol{F}_{t_0}^{t_0+T}(\boldsymbol{x}_0)\boldsymbol{h}\right)^* \nabla \boldsymbol{F}_{t_0}^{t_0+T}(\boldsymbol{x}_0)\boldsymbol{h}\right\rangle.
\end{aligned} \tag{1.5}$$

The symmetric tensor

$$C_{t_0}^{t_0+T}(\boldsymbol{x}_0) \equiv \left(\nabla \boldsymbol{F}_{t_0}^{t_0+T}(\boldsymbol{x}_0)\boldsymbol{h}\right)^* \nabla \boldsymbol{F}_{t_0}^{t_0+T}(\boldsymbol{x}_0) \tag{1.6}$$

is known as the (forward) Cauchy-Green strain tensor. Since it is symmetric, all its eigenvalues must be real. Furthermore, since both $\nabla \boldsymbol{F}_{t_0}^{t_0+T}$ and $\nabla \boldsymbol{F}_{t_0}^{t_0+T}$ are invertible so too is $C_{t_0}^{t_0+T}$, hence all its eigenvalues must be non-zero. Finally, since the map $\nabla \boldsymbol{F}_{t_0}^{t_0+T}$ is invertible, for any non-zero $\boldsymbol{x}$ we must have $\nabla \boldsymbol{F}_{t_0}^{t_0+T}(\boldsymbol{x}) \neq \boldsymbol{0}$, so $\left\langle \nabla \boldsymbol{F}_{t_0}^{t_0+T}(\boldsymbol{x}), \nabla \boldsymbol{F}_{t_0}^{t_0+T}(\boldsymbol{x}) \right\rangle > 0$, and so $C_{t_0}^{t_0+T}$ is positive definite, and therefore all its eigenvalues must be strictly greater than zero. We label and order the eigenvalues as

$$0 < \lambda_1(\boldsymbol{x}_0) \leq \cdots \leq \lambda_n(\boldsymbol{x}_0). \tag{1.7}$$

In our applications, n is either 2 or 3, namely, we are analyzing two or three-dimensional flows.

The finite time Lyapunov exponent (FTLE) is defined as

$$\mathrm{FTLE}_{t_0}^{t_0+T}(\boldsymbol{x}_0) = \frac{1}{2|T|} \ln\left(\lambda_n(\boldsymbol{x}_0)\right). \tag{1.8}$$

The above work shows that the largest possible growth rate a perturbation can have is given by $\sqrt{\lambda_n(\boldsymbol{x}_0)}$, which occurs when the perturbation is aligned the the associated eigenvector of $\lambda_n(\boldsymbol{x}_0)$.

Note that the FTLE gives an upper bound on the growth rate of a perturbation, but it does not tell us what type of perturbation results; in other words, relative to a curve or surface, the FTLE does not distinguish between tangential or normal growth. There has been much work done to improve this, see for instance (Tang, Chan, and Haller 2011a; George Haller 2010; Haller and Beron-Vera 2012; George Haller 2013; Blazevski and Haller 2014; Mancho et al. 2013). A very good comparison between these approaches is given in (Hadjighasem et al. 2017). While this is a weakness of

the FTLE in identifying LCS, it is still the case that the FTLE provides, at least to this date, a strong combination of ease of computation and identification power of LCS, and is thus the method we use here to extract LCS.

Chapter 2

THE GEOMETRY OF INERTIAL PARTICLE MIXING IN URBAN FLOWS, FROM DETERMINISTIC AND RANDOM DISPLACEMENT MODELS

In our first study we examine pollutant transport in an urban neighborhood. We first analyze the deterministic case, and then examine how random noise affects transportation patterns. The work here is adapted from (Tang et al. 2012):

Published in: Physics of Fluids

Wenbo Tang, **Brent Knutson**, Alex Mahalov, and Reneta Dimitrova (2012)

We use Lagrangian measures, depicted by finite-time Lyapunov exponents, to characterize transport patterns of inertial pollutant particles formed in urban flows. Motivated by actual events we focus on flows in realistic urban geometry. Both deterministic and stochastic transport patterns have been identified, as inertial Lagrangian coherent structures. For the deterministic case, the organizing structures are well defined and we extract them at different hours of a day to reveal the variability of coherent patterns. For the stochastic case, we use a random displacement model for fluid particles and derive the governing equations for inertial particles to examine the change in organizing structures due to "zeroth-order" random noise. We find that, (1) the Langevin equation for inertial particles can be reduced to a random displacement model; (2) using random noise based on inhomogeneous turbulence, whose diffusivity is derived from k-ϵ models, major coherent structures survive to organize local flow patterns and weaker structures are smoothed out due to random motion.

2.1 Introduction

In recent decades, the fast growth of urban areas and heterogeneous use of land surfaces have generated great interest for scientists, engineers, and urban planners in understanding the physical processes associated with urban climates (Arnfield 2003; Britter and Hanna 2003; Fernando 2010; Fernando et al. 2010). In this problem, local physical processes are interconnected with synoptic and regional scale features (flow, terrain, etc.), providing neighborhood and street scales that are important for humans (Britter and Hanna 2003; Fernando et al. 2010). Fluid dynamical research focusing on urban environments provide valuable information in two directions. On the one hand, in the upscale direction, land use in urban and suburban areas creates inhomogeneity in the dynamical and thermal properties at the bottom boundary layer of the atmosphere, which in turn modifies regional and synoptic flows (Avissar and Pielke 1989; Kalnay and Cai 2003). Additionally, land surface characterization provides valuable information on pollutant sources for their long range dispersal (Civerolo et al. 2000). On the other hand, in the downscale direction, details of street architecture affects local wind and turbulence patterns driven by large, synoptic scale flows (Kastner-Klein, Berkowicz, and Britter 2004). Pollutants that affect human health, such as carbon monoxide, ozone, particulate matters (PM), and harmful materials, are highly variable within street-neighborhood scale flows (Fernando et al. 2010). Characterizing transport patterns based on resolved urban flows is thus imperative for improvements on city planning and the quality of human lives. In this chapter, we extract such patterns for both deterministic and stochastic flows in a real urban dispersion model.

In conventional studies of urban fluid dynamics, the focus is on the fluid motion and

dispersion in idealized urban street canyons or for flow past isolated /regularly spaced buildings (Sini, Anquetin, and Mestayer 1996; Kim and Baik 2001, 2004; Belcher 2005). While the studies on these models provide fundamental understandings of the phenomenology for urban flows, and are useful in a parameterization to represent land surface uses in regional-global scale models, they offer limited information in evaluating the effects of pollutant dispersion at human related scales. For operational use of urban climate forecast and warning issuances, an exact representation of the urban geometry should be considered. To emphasize our point, we note the Hermoso Park dispersion study (HPS) mandated by the state of Arizona to address policy-related questions on the well beings of residents in a legislative district in southeast Phoenix. It is claimed that the heightened respiratory illnesses in the area are related to high levels of pollutant concentrations (Fernando et al. 2010). With real applications on air quality in mind, we focus our study on extracting pollutant patterns in the HP area, driven by wind and thermal forcing measured from a meteorological tower inside the area of interest.

Pollutant particles have finite-size and dynamically the behave differently than idealized fluid particles. In the case of rigid spheres, motions of finite-size particles are captured by the Maxey-Riley equations (Maxey and Riley 1983; Auton, Hunt, and Prud'Homme 1988). Among atmospheric pollutants, the most common particles are particulate matters, characterized by their aerodynamic diameters. In particular, PM of diameter less that 10 μm (PM_{10}, mainly combustion particles) and 2.5 μm ($PM_{2.5}$, mainly organic compounds and sulfates) are of major concern due to their prevalence in the environment. For particles with small diameters (such as PM), simplifications to the Maxey-Riley equations can be made to approximate particle motions (Maxey 1987; Druzhinin 1995; Babiano et al. 2000; Ferry and Balachandar 2001; Mograbi and

Bar-ziv 2006; Haller and Sapsis 2008). Our study is based on the simplified set of equations, discussed in detail later.

As pointed out in Belcher (Belcher 2005), strong dispersion of contaminant parcels of air are induced by dividing streamlines that enhance topological dispersion. Clearly, identification of the topology of inertial particle flows will be a useful tool to locate regions of high dispersion, as well as regions of strong accumulation. In this vein, we use inertial Lagrangian coherent structures (ILCS), first described in (Sapsis and Haller 2009), to characterize inertial particle motion in the HP area. The ILCS are analogous to LCS for idealized fluid particles, sans the difference in the inertial effects on motions. We favor a Lagrangian approach, as they provide objective description of the flow topology (G. Haller 2001, 2005). As a comparison, Eulerian criteria are based on instantaneous velocity fields or their gradient invariants, which are frame dependent (Okubo 1970; Chong, Perry, and Cantwell 1990; Weiss 1991; Jeong and Hussain 1995). In the first half of our results, we use this methodology to examine the organizing patterns of PM with different diameters. Using output of street-scale wind models at different times of the day, we find the temporal variations of the organizing patterns in deterministic flows.

For previous work on ILCS, little is known on the effects of random noise on the coherent structures. The objective of obtaining stochastic ILCS is to find the most probable mixing patterns in realistic environment. In the latter half of our results, we consider an inhomogeneous random displacement mode (RDM) extension of the Maxey-Riley equations, whose randomness is based on parameterized diffusivity from resolved flow fields. We obtain stochastic ILCS for PM_{10} and $PM_{2.5}$. Their relation with the deterministic ILCS will be discussed. We are only aware of two studies on stochastic LCS for idealized fluid flows, (Olcay, Pottebaum, and Krueger 2010;

Tang, Taylor, and Mahalov 2010), neither of which considered inhomogeneous noise for inertial particles.

The rest of this chapter is organized as follows. In section 2.2, we discuss the simplified version of the Maxey-Riley equations and the corresponding random displacement extension. Using an approach in (Rodean 1996), we find that the stochastic term acts directly on the inertial equations. In section 2.3, we discuss the street-scale wind model from which we obtain background wind data and parameterized turbulence as inputs to our analyses. We also discuss numerical schemes for our analyses, as well as the computation of finite-time Lyapunov exponents (FTLE). In section 2.4, we present results for both deterministic and stochastic ILCS associated with our flow. Lastly, in section 2.5 we summarize our findings and discuss future directions.

2.2 Mathematical Formulation

2.2.1 The governing equations

To formulate the mathematical problem, we make the following physical assumptions. (1) Inertial particles are carried by background fluid particles, which conduct random position processes in inhomogeneous turbulence (i.e. , the positions for the fluid particles are governed by a RDM); (2) the random background fluid velocity affects inertial particle dynamics through viscous drag; (3) the body force term experienced by an inertial particle is modeled by a deterministic force due to Lagrangian change in velocity of a fluid particle in its position plus random noise due to randomness in fluid velocity; (4) the random excitation of inertial particle velocity due to Brownian motion is negligible as compared to randomness induced by background

eddies. Following (Rodean 1996), the RDM for background fluid particle displacement is

$$\boldsymbol{u}_f = \boldsymbol{u} + \boldsymbol{u}_{dr} + \sigma \dot{\boldsymbol{W}}_a, \tag{2.1}$$

where $\boldsymbol{u}_f$ is the random fluid particle velocity, $\boldsymbol{u}$ a deterministic fluid velocity resolved by models or measurements, $\boldsymbol{u}_{dr} = \partial \boldsymbol{K}(\boldsymbol{x})\partial/\boldsymbol{x}$ a deterministic drift velocity due to turbulence inhomogeneity, and $\sigma \dot{\boldsymbol{W}}_a$ a vector Wiener process with standard deviation $\sigma(\boldsymbol{x}, t) = \sqrt{2\boldsymbol{K}}$, dependent on local diffusivity $\boldsymbol{K}(\boldsymbol{x}, t)$. As discussed in (Rodean 1996), the drift term $\boldsymbol{u}_{dr}$ is derived exactly from a consistency condition based on the Fokker-Planck equation to enforce a well-mixed condition when random noise is inhomogeneous- see (Thomson 1987), and it is independent from the random noise term $\sigma \dot{\boldsymbol{W}}_a$. We explain the validity of RDM for background fluid in later texts.

Consider typical urban flow length scales of order 1-10 meters, the size of PM is very small, where we can safely neglect the Faxen correction term (Benczik, Toroczkai, and Tel 2002). We also follow prior studies to neglect the Basset history force term (Maxey 1987; Mograbi and Bar-ziv 2006; Haller and Sapsis 2008). Justifications for removal of the history force term for small particles have been provided in (Sapsis et al. 2011). In this asymptotic limit, the model for the motion of a single spherical particle is the following:

$$\begin{aligned} \dot{\boldsymbol{x}} &= \boldsymbol{v} \\ \boldsymbol{v} - \frac{3R}{2}\left[\frac{D(\boldsymbol{u} + \boldsymbol{u}_{dr})}{Dt} + \eta \dot{\boldsymbol{W}}_b\right] &= -\frac{1}{\epsilon}(\boldsymbol{v} - \boldsymbol{u}_f) + \left(1 - \frac{3R}{2}\right)\boldsymbol{g}, \end{aligned} \tag{2.2}$$

where $\boldsymbol{g}$ is the vector of gravity, $\boldsymbol{u}, \boldsymbol{u}_{dr}$ and $\boldsymbol{u}_f$ are from the ambient fluid velocity equation 2.1, $\eta \dot{\boldsymbol{W}}_b$ is another vector Wiener process with standard deviation η and independent from $\sigma \dot{\boldsymbol{W}}_a$, and

$$R \equiv \frac{2\rho_f}{\rho_f + 2\rho_p}, \quad St \equiv \frac{2}{9}\left(\frac{a}{L}\right)^2 Re_f, \quad \epsilon \equiv \frac{St}{R}. \tag{2.3}$$

Here, ρ_f and ρ_p are the densities of the fluid and particle, respectively; R is the density ration distinguishing neutrally buoyant particles ($R = 2/3$) from aerosols ($0 < R < 2/3$) and bubbles ($2/3 < R < 2$); a is the radius of the spherical particle; L is a characteristic length scale of the flow; the fluid Reynolds number is $Re_f = UL/\nu$, with typical large scale velocity scale U and fluid viscosity ν; time is non-dimensionalized with the characteristic time scale L/U. The first term in the square bracket of equation 2.2 is the body force experienced by a fluid particle due to deterministic background fluid particle motion, and the second term the standard deviation η characterizes fluid velocity variance (hence the entire square bracket describes stochastic body force experienced by a fluid particle in position of the inertial particle). These two terms, together with the factor $3R/2$, gives the body force experience by an inertial particle. The first term of the right hand side of this equation is the viscous drag term, where $\boldsymbol{u}_f$ is random. The second term on the right hand side is a buoyancy term. Note that, we do not use $D\boldsymbol{u}_f/Dt$ for the body force term since $\sigma\dot{\boldsymbol{W}}_a$ is not differentiable.

In the deterministic case where $\sigma = \eta = 0$ and $\boldsymbol{u}_{dr} = 0$, provided that the velocity deformation is not too strong with respect to the parameter ϵ (Sapsis and Haller 2008; Tang et al. 2009), there exists a slow manifold M_ϵ that attracts dynamics in the phase space (Haller and Sapsis 2008). The inertial equations resolve a problem on backward-tracking of trajectories due to a reverse-time numerical instability, the deterministic ILCS is then extracted based on the slow dynamics (Sapsis and Haller 2009).

For the stochastic case, we rearrange the equation for $\boldsymbol{v}$ and write in terms of the velocity fluctuation $\boldsymbol{v}_f = \boldsymbol{v} - \boldsymbol{u} - \boldsymbol{u}_{dr}$ as

$$\mathrm{d}\boldsymbol{v}_f = -\frac{\boldsymbol{v}_f}{\epsilon}\mathrm{d}t + \left(\frac{3R}{2} - 1\right)\left[D\left(\boldsymbol{u} + \boldsymbol{u}_{dr}\right) - \boldsymbol{g}\mathrm{d}t\right] + \frac{\sigma}{\epsilon}\mathrm{d}\boldsymbol{W}_a + \frac{3R}{2}\eta\mathrm{d}\boldsymbol{W}_b. \tag{2.4}$$

Notice that 2.4 is also a Langevin equation, with the Lagrangian decorrelation time scale ϵ, drift terms due to body force and buoyancy, and two random terms due to stochastic drag and body force. Based on 3D results in (Rodean 1996), the fluid velocity standard deviation $\eta_i = b_i u^\star$ and the position standard deviation $\sigma_i = 2b_i^2 u^\star/(C_0\varepsilon)^{1/2}$, both are order one quantities as far as the size parameter ϵ is concerned. Here, $C_0 = 5.7$ is a semianalytical constant, b_i an empirical constant in the ith direction, $i = 1, 2, 3$, $\varepsilon = u^{\star 3}/\mathrm{kl}$ the local energy dissipation rate estimated by the crude first-order closure, $u^\star$ the dimensionless friction velocity, $k = 0.4$ the von Karman constant, and l a local dimensionless length scale. We further simplify this expression by arguing that the first stochastic term is dominant in the regime of interest (small-size aerosols, $St \ll 1$, hence $1/\epsilon \equiv R/St \gg R$), thus we drop the last term in 2.4. We discuss choices of $b_i, u^\star$, and l in section 2.3.2.

Our equation 2.1 differs from typical Lagrangian stochastic models (LSM) (Rodean 1996; Wilson and Sawford 1996) that consider Langevin equations for fluid velocities. The problem we consider is inhomogeneous, which in the LSM approach would require many terms to deal with correlated random noise. The simplicity in $\boldsymbol{u}_f$ allows us to focus on the Langevin equation for $\vec{v}_f$. In general, LSM is more appropriate that RDM. RDM is applicable in the "far field" regime, when the time scale is much greater than the Lagrangian decorrelation scale of a fluid velocity and when the random noise is Gaussian (Rodean 1996). We are not particularly interested in reproducing a dispersion cloud for specialized release events. Instead, we explore answers to the following questions: (1) What is the most likely trajectory that an inertial particle would take in a stochastic environment? (2) What organizing structure can we obtain

from these most tenable trajectories, so we obtain an overview of regions that are more vulnerable to pollutant dispersions? We also assume Gaussian statistics for the random noise. Under these conditions we are in a regime where RDM equation 2.1 is valid. In this vein, we also study simplified version for equation 2.2. In the long-time limit, this equation should reduce to the diffusion limit, governed by a RDM (Thomson 1987; Rodean 1996), to be derived later.

We also consider stochastic back trajectories for structure extraction, with reasons give later in this section. Following earlier work on backward-time LSM, (Flesch, Wilson, and Yee 1995), we find that the consistency condition merely requires the reflection of the velocity $\boldsymbol{u} + \boldsymbol{u}_{dr}$. It is noted that (Thomson 1987; Flesch, Wilson, and Yee 1995) for turbulence in an incompressible flow, the probability density for forward-time models and backward-time models are equivalent. In addition, since the forward model and the "reversed" backward model are identical, Smith's (Smith 1957) reciprocal theorem also applies. This implies that we can simply run the backward-time RDM model to obtain the statistics on the composition of particles observed at a point $\boldsymbol{x}$ at a time t.

2.2.2 Reduction of Langevin equation to random displacement model

We reparameterize equation 2.4 in time such that $\epsilon = \alpha T$, where $\alpha \to 0$ and T is order one, a time scale felt for the long-term stochastic trajectories. Applying the methodology discussed in (Rodean 1996), we integrate equation 2.4 in time to obtain

$$\alpha[\boldsymbol{v}_f]_0^t = \int_0^t \left\{ -\frac{\boldsymbol{v}_f}{T}\mathrm{d}t + \alpha\left(\frac{3R}{2} - 1\right)[D(\boldsymbol{u} + \boldsymbol{u}_{dr}) - \boldsymbol{g}\mathrm{d}t] + \frac{\sigma}{T}\mathrm{d}\boldsymbol{W}_a \right\} \tag{2.5}$$

In the $\alpha \to 0$ limit, the leading order balance in the above equation is between

the first and third term on the right-hand side. If we further assume that on average the velocity fluctuation jump $[\boldsymbol{v}_f]_0^t$ as well as the two drift forces in the integrand are order one, over time the second term on the right-hand side supersedes the left-hand side and can be considered as a first order correction, thus

$$\int_0^t \frac{\boldsymbol{v}_f}{T}\mathrm{d}t = \int_0^t \alpha\left(\frac{3R}{2}-1\right)[D(\boldsymbol{u}+\boldsymbol{u}_{dr})-\boldsymbol{g}\mathrm{d}t]+\frac{\sigma}{T}\mathrm{d}\boldsymbol{W}_a \tag{2.6}$$

Noting that $\boldsymbol{v}_f = \mathrm{d}\boldsymbol{x}_f/\mathrm{d}t$, where $\boldsymbol{x}_f$ is the position process for the fluctuations, the left hand side can be expressed as

$$\int_0^t \frac{\boldsymbol{x}_f}{T}\mathrm{d}t = \int_0^t \alpha\left(\frac{3R}{2}-1\right)[D(\boldsymbol{u}+\boldsymbol{u}_{dr})-\boldsymbol{g}\mathrm{d}t]+\frac{\sigma}{T}\mathrm{d}\boldsymbol{W}_a \tag{2.7}$$

Differentiating with respect to t and multiplying by T and converting $\boldsymbol{v}_f$ back to $\boldsymbol{v}$ we obtain the RDM for the inertial particle displacement,

$$\frac{\mathrm{d}\boldsymbol{x}}{\mathrm{d}t} = \boldsymbol{u}+\boldsymbol{u}_{dr}+\epsilon\left(\frac{3R}{2}-1\right)\left[\frac{D(\boldsymbol{u}+\boldsymbol{u}_{dr})}{Dt}-\boldsymbol{g}\right]+\sigma\dot{\boldsymbol{W}}_a. \tag{2.8}$$

This expression converges towards an inertial equation for the slow dynamics

$$\frac{\mathrm{d}\boldsymbol{x}}{\mathrm{d}t} = \boldsymbol{u}+\epsilon\left(\frac{3R}{2}-1\right)\left[\frac{D\boldsymbol{u}}{Dt}-\boldsymbol{g}\right] \tag{2.9}$$

in the deterministic limit, first derived in (Haller and Sapsis 2008) using singular expansion. The random position process consists of the slow manifold velocity, a deterministic drift term due to inhomogeneous turbulence, and a random walk term from the RDM for background fluid particles. Note that we cannot directly use the singular perturbation approach here since $\dot{\boldsymbol{W}}_a$ is not differentiable.

2.2.3 Inertial Lagrangian coherent structures

LCS are distinguished material lines/surfaces that attract/repel local trajectories at the maximal rates (G. Haller 2000; Haller and Yuan 2000). Recently, it has become popular that FTLE be used to extract LCS. Basing on local dynamics of trajectories, FTLE offers an objective description of how nearby trajectories stretch with the background flow. As a result, local material lines that repel nearby trajectories the most is identified. Reciprocally, attractors are found as local maximizers of FTLE when trajectories are integrated in backward-time. In the first development of the theory, FTLE fields do not distinguish large stretching from shear (G. Haller 2001). This difficulty has been resolved in a recent development based on a variational theory (G. Haller 2011).

The LCS methodology was first extended to study inertial particle mixing in (Sapsis and Haller 2009), where they studied the mixing topology for inertial particles inside hurricane Isabelle. Using the singular perturbation (Haller and Sapsis 2008), the authors overcome the numerical instability of source inversion for finite-size particles. As a result, both forward-time and backward-time trajectories are computed based on the slow manifold dynamics, and coherent structures are extracted. ILCS has also been used to identify prey dynamics in jellyfish feeding (Sapsis, Peng, and Haller 2011), where the authors locate regions near a jellyfish that prey cannot escape predation.

In our context, we extract ILCS that organize pollutant particle dynamics. We use the inertial equation approach, since in forward-time we only deal with three-dimensional physical space instead of the full six-dimensional phase space, and in backward-time this is the only way to obtain back-trajectories correctly. We obtain the entire inertial particle mixing geometry for both deterministic and stochastic

environments. The deterministic case is a direct extension from our previous work (Tang et al. 2009), yet the stochastic case has not been considered before. The more general LSM formulations for inertial particle involves extra modeling, such as a modified Lagrangian decorrelation time, which is not a direct result of the Maxey-Riley equations (Csanady 1963; Sawford and Guest 1991). Using Maxey-Riley equation directly in backward-time, as demonstrated in (Haller and Sapsis 2008), results in numerical instability even for deterministic trajectories.

We address the stochastic ILCS in the following approach. With the use of RDM, we estimate the probability that a trajectory evolves in an environment with turbulent eddies. In forward-time, the concept is straightforward: we find the most likely trajectory that an inertial particle starting from $\boldsymbol{x}_0, t_0$ would end up, after some integration time T (expectation of $\boldsymbol{x}$). The most likely repelling structures is thus ILCS based on the mean trajectories. In backward-time, we find stochastic trajectories, again starting from $\boldsymbol{x}_0, t_0$. Expectation of the random trajectories show the most likely starting point for the particle occupying $\boldsymbol{x}_0$ at t_0. As mentioned earlier, this interpretation of probability is valid because of the forward-backward probability equivalence and the validity of reciprocal theorem with RDM. Attracting ILCS are then obtained, again from the mean trajectories.

2.3 Numerical Details

2.3.1 Urban wind model

We use the quick urban and industrial complex (QUIC) model developed at the Los Alamos National Laboratory to resolve street-scale urban flows at HP. The

numerical model consists of a wind model, QUIC-URB, and an inhomogeneous LSM dispersion model, QUIC-PLUME. For reasons mentioned in section 1.1, since we study the inertial dynamics based on RDM and the slow manifold, we did not use QUIC-PLUME. QUIC-URB is based on the Rockle approach (Rockle 1990), in which a mass-consistent diagnostic wind model computes the 3D flow fields around buildings. An initial wind field is prescribed based on an incident flow, and superimposed on this are various time-averaged flow effects of buildings. The QUIC-URB utilizes empirical algorithms for determining initial wind fields on the roots, in upstream recirculation zones, in the downwind cavity and wake of a single building, and in street canyons between buildings. A mass-consistent wind field is produced similar to traditional diagnostic wind models, but special treatment of boundary conditions is needed at the building walls (Pardyjak and Brown 2001; B.Singh et al. 2008).

The QUIC simulations were initiated from data collected during the HP study campaign conducted in early 2009. A 10 m meteorological tower inside the study area was instrumented with two sonic anemometers for flow, turbulence, and flux measurements and radiometers for incoming, outgoing, and net solar radiation. For more details of the field measurements and the model domain, the readers are referred to discussions and Fig. 13 in (Fernando et al. 2010).

Based on the data input, the simulations were performed on two domains: an outer domain that covered the entire HP area and an inner domain around the meteorological tower. The computation area was $4900 \times 4220 \times 280$ m^3, with 20 m horizontal and 4 m vertical resolution for the outer domain, and a $1200 \times 1050 \times 140$ m^3 area with 5 m horizontal and 2 m vertical resolution for the inner domain. Trees and vehicles were excluded and the terrain was considered flat, which is a good approximation.

2.3.2 Details of deterministic and random displacement model

The QUIC-URB outputs are dimensional variables. We use a typical length scale of a building inside the HP area, $L = 45$ m, and an appropriate velocity scale at the particular time, say, $U = 1(3)$ m/s for 6 a.m. (6 p.m.) to non-dimensionalize our problem. The Lagrangian integration time is 40 time units. Henceforth, the dimensional integration time is 30 (10) min for the two cases. We examine dynamics for both PM_{10} and $PM_{2.5}$. Since the fluid velocity scale varies, the parameter ϵ changes at different times. For example, consider $PM_{2.5}$ density to be 1000 times of air, then at 6 a.m. $\epsilon_{2.5} = 7.7199 \times 10^{-7}$, $\epsilon_{10} = 1.2352 \times 10^{-5}$, and at 6 p.m., $\epsilon_{2.5} = 2.316 \times 10^{-6}$, $\epsilon_{10} = 3.706 \times 10^{-5}$.

We have two different datasets from QUIC-URB. On January 16, 2009, one-hour averages of observational measurements were available at every hour of the day, hence allowing the study of variability of structures over time. We used velocity interpolation between two frames of data to extract ILCS based on this slowly varying unsteady flow. On February 15, 2009, one-minute averages of observational measurements were available in the morning, hence the background flow reflects better reality. We study stochastic ILCS with this dataset.

For the deterministic case, we focus on two representative hours from the data: 6 a.m., and 6 p.m. The 6 a.m. and 6 p.m. cases represent flows during the rush hours, where emission from the streets are likely to be high and they may quickly align with ILCS. In order to obtain high resolution results on ILCS, we use a grid size of 0.25 m over the entire inner domain to generate deterministic trajectories. The Lagrangian integration code is parallelized and ran on a 14 node cluster with 224 central processing units to achieve such high resolution. Trajectories are computed

using the fourth order Runga-Kutta methods from the inertial equation. Repelling (attracting) ILCS are computed from the forward-time (backward-time) integrations.

For the stochastic case, we need to compute $\boldsymbol{K}$. We only consider a diagonal diffusion tensor, where dimensionless $K_i = 2b_i^4 k u^\star l / C_0$. We use parameters implemented in QUIC-PLUME (Pardyjak and Brown 2001), where in the horizontal direction, $b_1 = b_2 = 2$ and in the vertical direction $b_3 = 1.3$. This anisotrophy reflects a vertical density stratification. The friction velocity $u^{star} = (k\Delta z/U)\partial|\boldsymbol{u}_h|/\partial z$ is based on vertical wind shear, and Δz is the smallest distance of the particle to a wall/ground/roof. l is a local length scale, taken to be the smaller of $z + z_0$ or l_{eddy}, where z is the height from the ground/roof, z_0 is the roughness length taken to be 1 m in dimensional units (Fernando et al. 2010), and $l_{eddy} = ku/|\mathrm{d}u/\mathrm{d}z|$ (Williams et al. 2004).

We use 1000 realizations for each initial condition $\boldsymbol{x}_0$. To accommodate the size of stochastic simulations, we reduce the resolution of initial conditions to $5 \times 5 \times 2$ m, and only focus on smaller regions of interest. The inertial equations are computed based on explicit Euler methods with Gaussian white noise. For comparison, we also examine for a sample initial condition, the full Maxey-Riley equations and their inertial equations. We use implicit Euler for the deterministic parts of the full Maxey-Riley equations, explicit random noise is added in the end of the time step.

In our formulations, no-slip boundary conditions are considered. This is because when particles approach the boundary, their background velocity approaches zero. As a result, particles fall to the ground due to the gravity term if the boundary condition is set to be reflective. Since there is no reason that a pollutant particle cannot stick to rough building surfaces, and the no-slip boundary condition preserves the vertical structure when particles hit the wall, we prefer using the no-slip boundary condition.

One concern of the no-slip boundary condition is that the setup makes the random

term near the wall not really Gaussian. In our RDM formulation, eddy diffusivity is based on the nearest ground or wall, hence diffusion is very limited for trajectories near buildings, and this near-wall non-Gaussianity does not affect major dynamics in the interior of the domain. A further concern is that, for an initial condition near the wall, if there is equal probability for the particle to stick to the wall or disperse away from the wall, the expectation can be nowhere near any of the high probability regions. However, consider two nearby particles, the realizations for one of them completely hit the wall, and the realizations for the other completely disperse away, the separation measured between the averaged trajectories for these particles are still large and the ILCS should still be highlighted, so we should be safe as far as ILCS are concerned.

For RDM formulation, (Wilson and Yee 2007) pointed out that a constraint on the time stepping size is needed. Following their paper, for our inhomogeneous eddy parameterization in 3D, we require a constraint on the time steeping of the RDM

$$\sqrt{2K\Delta t}\frac{1}{K}\left|\frac{\partial K_i}{\partial x_i}\right| \ll 1, \tag{2.10}$$

where $|\cdot|$ denotes the norm of the argument vector.

Finally, we use a linear extrapolation technique developed in (Tang, Chan, and Haller 2010) to deal with trajectories leaving the outer domain. The extrapolation is done in 2D horizontal surfaces. This is because with a no-slip boundary condition at $Z = 0$ and incompressibility, 3D extrapolation would leave the flow motionless. Since the resolved flow on the outer domain is almost two-dimensional and unidirectional (Fernando et al. 2010) due to the small size of buildings in nearby districts, it is not unreasonable to implement just the 2D extrapolation at every height. Between the inner and outer, and outer and extrapolated domains, we use a filter to smoothly transition velocity data, to avoid the development of spurious structures.

Note that in the initial study, (Fernando et al. 2010), density for pollutant particles is reported for two different times of the day. Their result is specific to a particular emission characteristics, which is not the main goal of our study. We focus on obtaining the flow topology, which is an overall evaluation of the patterns inside the domain of interest. High pollutant densities are expected to accumulate along attracting structures and high dispersion to associate with repelling structures of ILCS extraction.

2.3.3 Computation of FTLE and extraction of ILCS

The mathematical background of the FTLE was discussed earlier in section 1.1, henceforth we briefly outline the computation. We compute the particle displacements starting from initial condition $(\boldsymbol{x}_0, t_0)$ using the inertial equation 2.9 in the deterministic case, and equation 2.8 in the stochastic case. For the stochastic case, we compute the ensemble of realizations to obtain the mean trajectory $\mathbb{E}(\boldsymbol{x})$. Denoting the trajectory $\boldsymbol{x}(t; \boldsymbol{x}_0, t_0)$, we define the Cauchy-Green strain tensor field as

$$M_{t_0}^{t}(\boldsymbol{x}_0) \equiv \left[\frac{\partial \boldsymbol{x}(t; \boldsymbol{x}_0, t_0)}{\partial \boldsymbol{x}_0}\right]^T \left[\frac{\partial \boldsymbol{x}(t; \boldsymbol{x}_0, t_0)}{\partial \boldsymbol{x}_0}\right], \tag{2.11}$$

where $[\partial \boldsymbol{x}/\partial \boldsymbol{x}_0]^T$ denotes the transpose of the deformation gradient tensor $\partial \boldsymbol{x}/\partial \boldsymbol{x}_0$. The FTLE field, $FTLE_{t_0}^{t}(\boldsymbol{x}_0)$, is then defined as the scalar field that associates with each initial position $\boldsymbol{x}_0$ the maximal rate of stretching along $\boldsymbol{x}(t; \boldsymbol{x}_0, t_0)$,

$$FTLE_{t_0}^{t}(\boldsymbol{x}_0) = \frac{1}{2|t - t_0|} \ln \lambda_{max}(M), \tag{2.12}$$

with $\lambda_{max}(M)$ denoting the maximum eigenvalue of M.

Traditionally, ILCS boundaries are identified as the highlighters of the FTLE field. It is known that highlighters of the FTLE field alone would indicate both shear

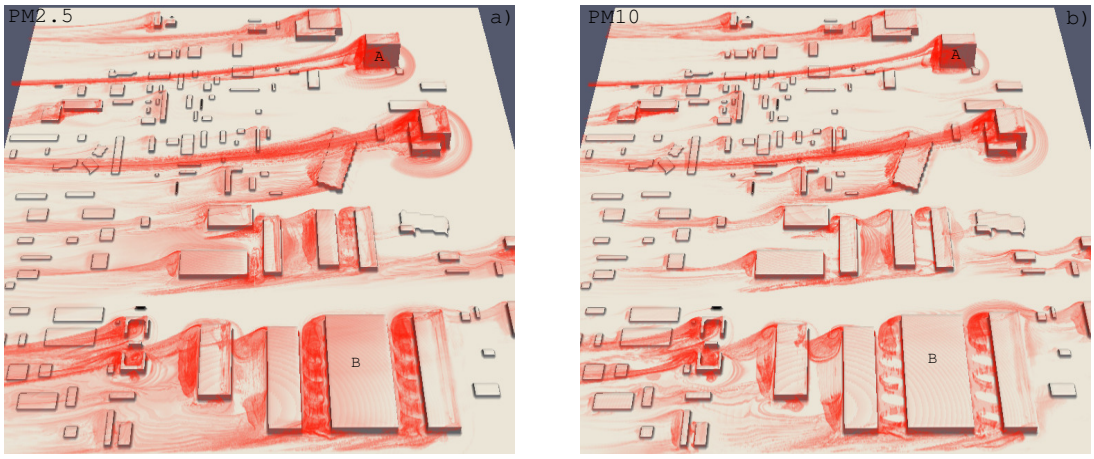

Figure 1. Three-dimensional view of backward-time ILCS at 6 AM on January 16, 2009. (a) PM2.5. (b) PM10. Note the removal of separation structures at the roof top with PM10.

and hyperbolic structures. In our current study, we only consider such highlighters in backward FTLE as major attractors, with acceptance that there might be false positives due to shear structures. We leave such decomposition processes to later studies.

2.4 Results

2.4.1 Deterministic transport

We first discuss results from the deterministic model as our baseline geometry. Figure 1 reveals the full three-dimensional view of backward-time ILCS at 6 a.m. on January 16, 2009 for $PM_{2.5}$ and PM_{10}, respectively. The region is viewed from the south. Since backward-time structures highlight attracting motion, the ILCS in Figure 1 show patterns where deterministic particles cluster. Major structures

can be identified in the wake of several big buildings in the northeast corner of the figure (e.g. building A). When the particle size is small, trajectories behave more like fluid particle trajectories. As such, recirculating bubbles at the roof top can be seen in most buildings in Figure 1 (a). The tails trailing these tall buildings indicate material surfaces which attract nearby trajectories. They highlight the converging flow structures coming from the north and south of the buildings. Also, at the foot of these buildings, shielding structures can be located where trajectories from the outside and inside of building wakes collapse. These shields are the boundaries of wakes near the buildings.

Another interesting feature in the 3D structures is located at the southeast corner of the domain, between several parallel buildings (e.g. next to building B in Figure 1 (a)). Vortices can be located inside the street canyons and they tend to fill up the entire width of the canyons. In general, vortices are typical elliptic structures that are not highlighted by FTLE. However, high values can be obtained on the edge of a vortex, where particle trajectories from different regions of the flow get entrained into the vortex. It is indeed the case here as we examine local particle trajectories (not shown). Above the vortices in the street canyon we observe structures highlighting skimming flows. Separation between the skimming flows and recirculation vortices can be seen near the roof top of the parallel buildings as a streamwise sheet structure laying on top of the spanwise rolls. In this region, three of the four street canyons have smaller width which lead to the recirculating vortex, whereas one of the street canyon (on the west) has a wider gap, resulting in no noticeable circulating structure in between the buildings.

As a comparison, in Figure 1 (b), due to the bigger size of PM_{10} particles, they fall to the roof top/ground faster, hence no roof top circulation is found. The ILCS

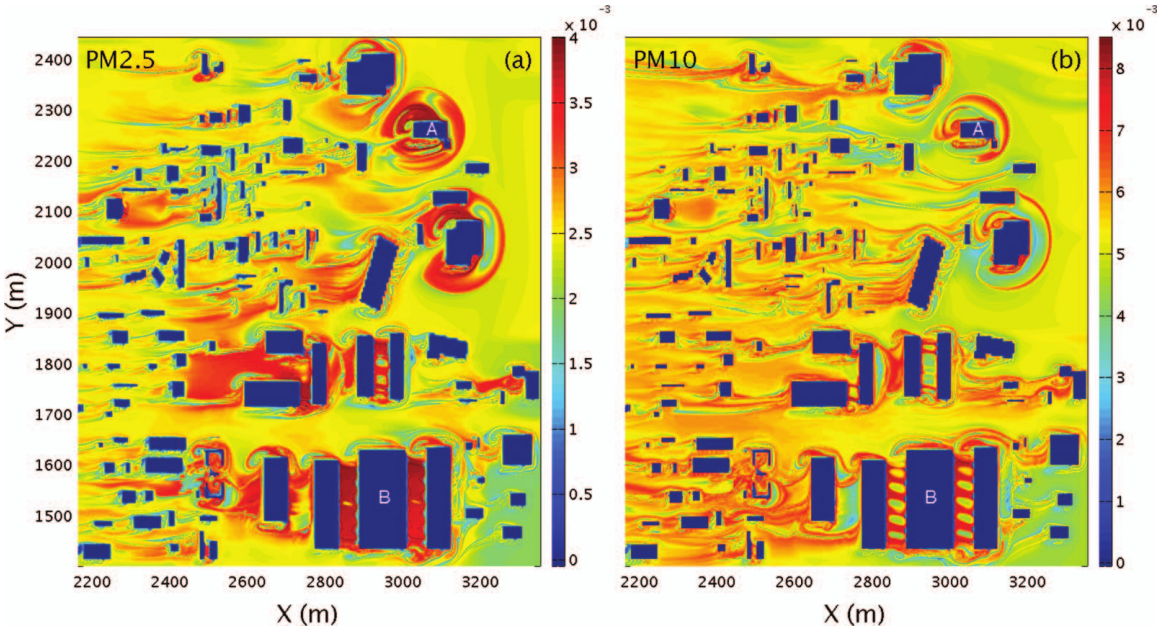

Figure 2. Attracting ILCS for deterministic dynamics evaluated at 6 AM on January 16, 2009. The two panels show structures associated with different particle sizes at $Z = 1$ m. (a) PM2.5. (b) PM10.

.

boundaries at the foot of the buildings appear to be much weaker than those in Figure 1 (a). Also, in the street canyon region the recirculating vortices seem to be less intense as compared to those structures based on $PM_{2.5}$, indicating less attraction of trajectories originating in different parts of the domain.

To understand the organizing structures at a height important to human activities, we show slices of ILCS at 1 m height, for particles of different sizes and at different times of the day. In Figure 2, the ILCS are obtained for $PM_{2.5}$ and PM_{10}. The tall building A seen in Figure 1 can be found around $X = 3100$ m, $Y = 2200$ m. The ILCS boundary upwind of A is very pronounced for both $PM_{2.5}$ and PM_{10}, but regions of strong attraction (highlighting mid-grey, red) appears to be wider for $PM_{2.5}$. This structure corresponds to the convergence of flows at the leading edge of the tall building when trajectories from the upwind direction collapse into trajectories from

the front of the building. These trajectories then move along the structure, around the sides of the building, with trajectories on the outside of the wake boundary moving downstream. Some of the trajectories are trapped inside the wake structure downwind of the building, as they get attracted to the backward-time FTLE in the trailing edge. As the PM size becomes larger, the ILCS boundaries (at $Z = 1$ m) become smaller and weaker, indicating less convergence of trajectories. This is because for larger particle sizes, trajectories initiated at this height fall to the ground too quickly, leaving little chance for attractors to form (cf. trajectory comparison initiated at $Z = 3$ in Figure 4 for different particle sizes).

Inside the street canyons next to building B, around $X = 2800 - 3100$ m and $Y = 1400 - 1800$ m, we find signatures of recirculating vortices. Clearly seen in Figure 2 (b), the cells of the recirculating vortices fill up the width of the canyon. These cells are almost indistinguishable in Figure 2 (a), probably because the vortices are reaching a vertical boundary at $Z = 1$ m.

In order to show the geometry for repellers (or separating streamlines (Belcher 2005)), so as to locate regions where high dispersion will occur, we plot the forward time ILCS in Figure 3. Again, particle sizes of $PM_{2.5}$ and PM_{10} have been shown. At this height, major structures are located downwind of the tall buildings and inside the street canyons, when the particle size is small. The structures inside the street canyon indicated the repelling geometry of the recirculating vortex. It is not too surprising that at this height, as the particle size gets larger, the structures are less complex. This is because in forward-time, most particles fall to the ground and stick to the bottom, leaving less repelling ILCS to form. As a comparison, backward-time trajectories ascend higher as time progresses (in backward-time) and separate farther, resulting in the ILCS being more distinguished.

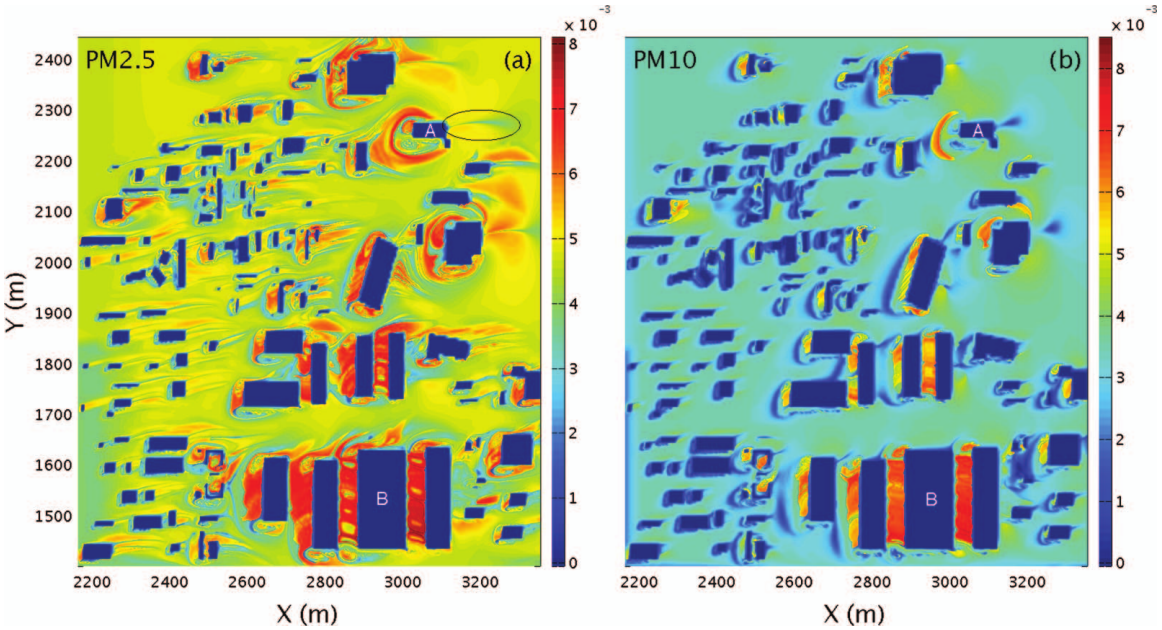

Figure 3. Repelling ILCS for deterministic dynamics evaluated at 6 AM on January 16, 2009. The two panels show structures associated with different particle sizes at $Z = 1$ m. (a) PM2.5. (b) PM10

.

We discuss structures formed around buildings A and B again for forward-time ILCS. First, in the street canyon region near building B, recirculating vortex cells are visible for both $PM_{2.5}$ and PM_{10}, corroborating with our findings from backward-time FTLE. On the other hand, the structure downwind of building A is indicative of separation among inertial particles going downstream and those trapped in the wake eddy. As particle size increases, this structure fades out, due to particle settling to the ground and so less separation is observed. Upstream of this building, there is a thin strip of low FTLE value, marked by an ellipse. High values of forward-time FTLE are expected if the incoming flow is predominantly two-dimensional and separate around the building. However, due to the low height and finite width of the building front, trajectories either fall to the ground stick to the building facade, or entrain into an eddy at the downwind edge of the building. Thus the separatrix is not well distinguished

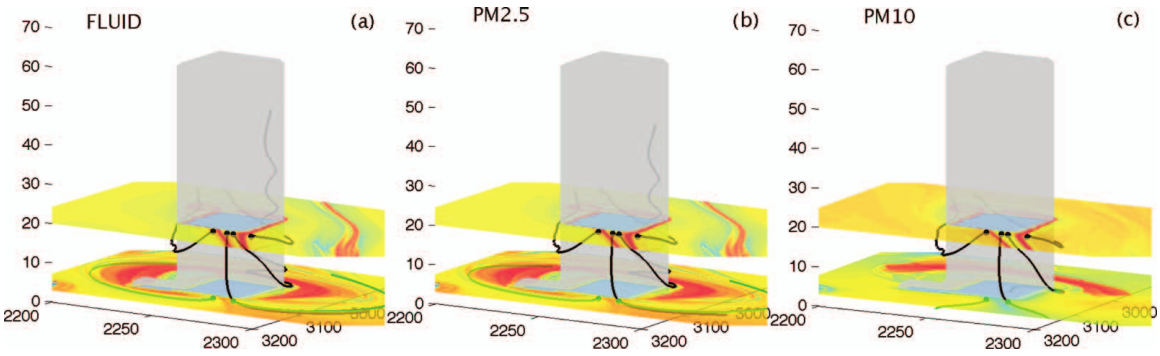

Figure 4. Particle trajectories initiated near forward-time ILCS upwind of building A. Black: released at $Z = 20$ m. Mid-grey (green): released at $Z = 3$ m. (a) Idealized fluid tracer. (b) PM2.5. (c) PM10

.

here. However, we do notice a quick change in FTLE value as one traverse along this structure, indicating entrance of a region where particles are advected far downstream. As particle size increases, this region of low separation expands, indicating more particles settling upstream of the tall building A, and similarly near other buildings.

To further support our interpretation of the weak structure upwind of building A, we show several trajectories released at the upwind side, associated with forward-time FTLE, for different particle sizes in Figure 4. We have compared three particle sizes: PM_0 (idealized fluid), $PM_{2.5}$, and PM_{10}. A common feature of the ILCS for these sizes is two highly distinguishable separatrices at $Z = 20$ m. At $Z = 3$ m, however, PM_0 and $PM_{2.5}$ show local FTLE maximum on the upwind side of the building, whereas PM_{10} shows a local FTLE minimum. We show trajectories initiated near the structures at $Z = 20$ m in black, and those initiated at $Z = 3$ m in mid-grey (green). For the black trajectories, it is clear that the two trajectories outside of the upwind structure separate around the building and advect far downstream. Trajectories initiated between the two FTLE maxima lines remain inside the building wake (although they may end up in different regions inside the wake). For the mid-grey (green) trajectories, they are

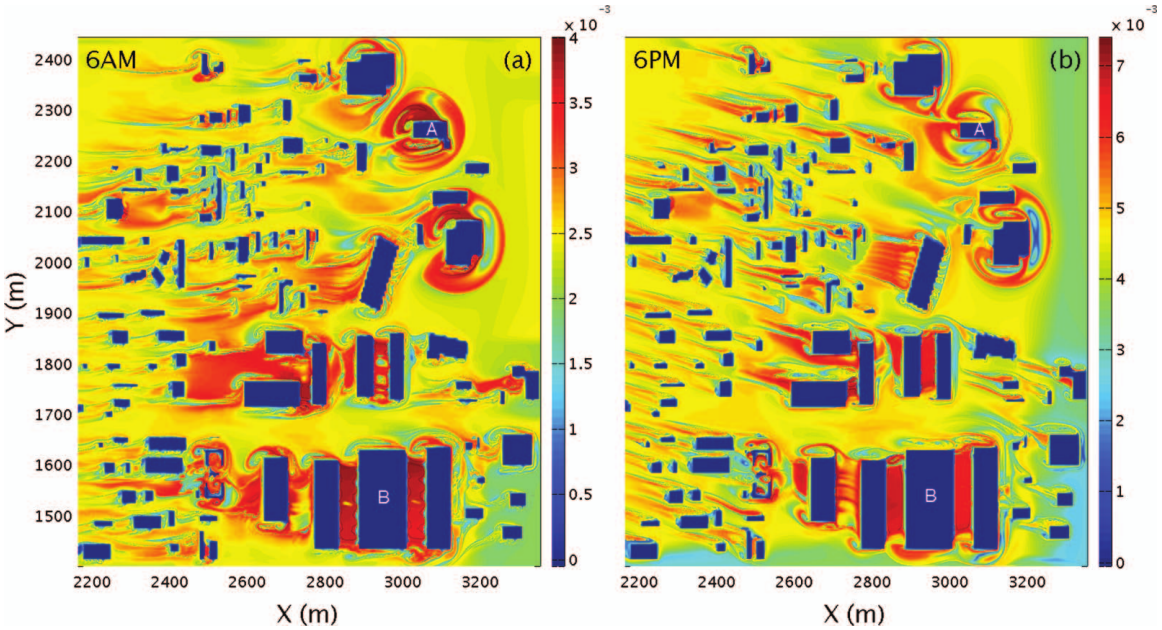

Figure 5. Comparison of backward-time FTLE for PM2.5 at two different times on January 16, 2009, at $Z = 1$ m. (a) 6 AM (b) 6 PM

initiated on the two sides of the separatrix at the upwind side of the building. Were they not falling to the ground (Figure 4 (a) and (b)), the trajectories would have moved around the building and thus a repelling topology could be found. For PM_{10}, in Figure 4 (c), the two mid-grey (green) trajectories fall to the ground too soon, leaving no chance of strong separation in this region, hence we observe the FTLE minima.

We study the temporal variation of the structures by extracting ILCS for data from two different hours, for $PM_{2.5}$. These ILCS at $Z = 1$ m are shown in Figures 5 and 6. At both times, the ambient wind appears to be predominantly from the east, thus the ILCS at both times are similar. However, the strength of the backward-time ILCS at 6 p.m. is larger than that at 6 a.m., probably due to the different incoming wind speeds. The forward-time ILCS at both times have similar strengths, probably due to the fact that they hit the ground very soon. Extraction at other times (not

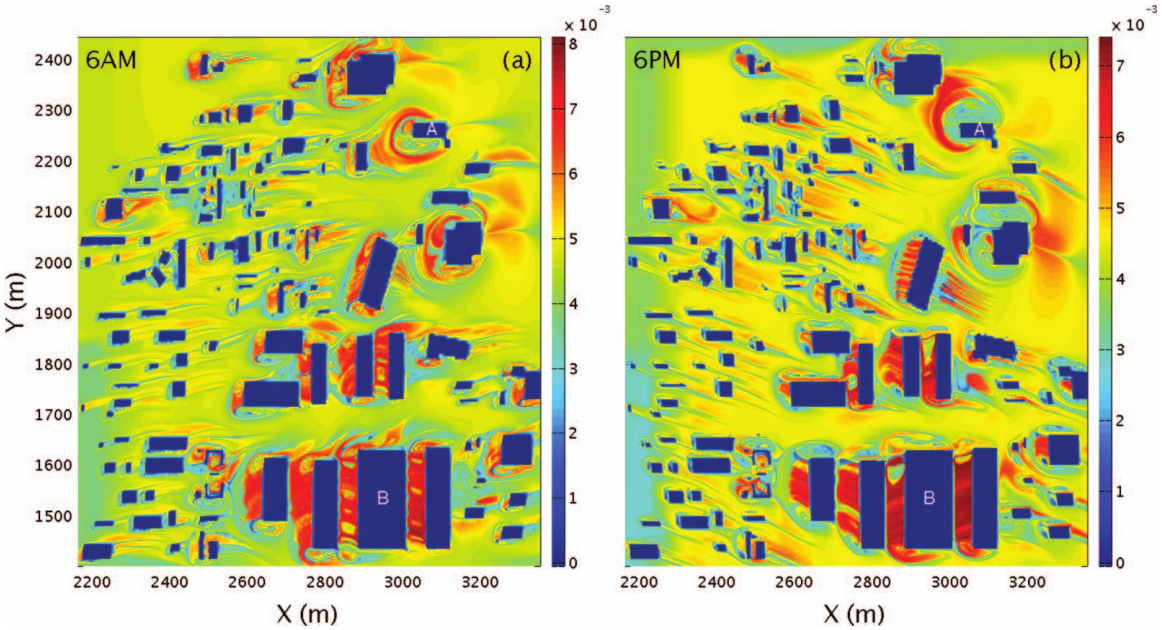

Figure 6. Comparison of forward-time FTLE for PM2.5 at two different times on January 16, 2009, at $Z = 1$ m. (a) 6 AM (b) 6 PM

shown) indicate the variation of coherent structures throughout the day. Combining the three-dimensional versions of Figures 5 and 6, one obtains the full description of the topology for deterministic inertial transport in the HP area.

2.4.2 Stochastic transport

The actual urban environment is indeed stochastic, with uncertainties in the unresolved scales possibly changing our deterministic evaluations. In this subsection, we examine random inertial particle trajectories and ILCS based on realistic random noise from turbulent eddies.

We consider the most probable trajectory for an inertial particle embedded in the stochastic environment. The random displacement model described in section

2.2.2 has been used. Coherent structures are based on the mean trajectories, with the interpretation that the stochastic ILCS is the most probable structure observed based on where inertial particles most likely go. In order to compare deterministic and stochastic models, we show in Figure 7, for a single initial condition (next to a building complex so flow has a wake structure), trajectories from both formulations in forward and backward-time. The mid-grey (red) curves in Figure 7 (a) show stochastic mean trajectories, with the dashed line in forward-time and solid line in backward-time, based on the full Maxey-Riley equations. The dark-grey (blue) curves in the same panel show stochastic mean trajectories based on the inertial equations, and the black curves show deterministic trajectories. The line styles are the same as the mid-grey (red) curves for forward and backward-time evolution. First, we find that the mean trajectories based on the slow manifold equation and full equations are almost identical in forward-time. As a comparison, the differences between stochastic and deterministic trajectories are quite pronounced. Second, we find that the backward-time stochastic trajectory based on the full equations becomes unstable very quickly in backward time. This is to be expected since equation 2.4 is strongly unstable in backward-time due to the first term on the right-hand side. For comparison between the stochastic full equations and inertial equations, we show the clustering of random realizations by particles in different colors. The mid-grey (red) particles show forward-time trajectories based on the full equations and the dark-grey (blue) particles are from inertial equations. Clearly, the patterns are comparable, leading to similar statistics for single trajectories. On the other hand, the light-grey (cyan) particles are those from inertial equations in backward-time (no realization from the full equations in backward-time survive the instability). Motivated by the fact that the two stochastic formulations result in identical mean trajectories in forward-time,

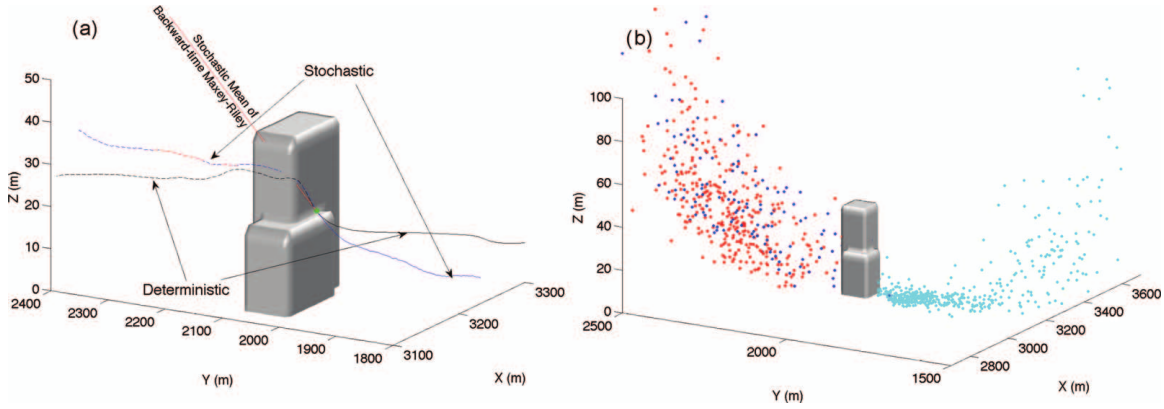

Figure 7. Comparisons among stochastic and deterministic trajectories. (a) Comparisons on the mean trajectories. Mid-grey (red): mean from full Maxey-Riley equations. Dark-grey (blue): mean from inertial equations. Black: deterministic equations. Solid: Backward-time trajectories. Dashed: Forward time trajectories. (b) Comparisons between the full equations and inertial equations for random realizations. Mid-grey (red): full equations, forward time. Dark-grey (blue): inertial equations, forward-time. Light-grey (cyan): inertial equations, backward time. Backward-time realizations with the full equations are not shown as they become unstable and leave the domain quickly

the inertial equations have only half the degrees of freedom, and the full equations blow up in backward-time, we use inertial equations as the governing equations in our computation.

Due to the computational cost for random dynamics, we only focus on regions near the tall building A in our stochastic cases. The stochastic ILCS is in terms of FTLE fields computed from the mean of the random trajectories. In Figure 8 we show the forward-time stochastic ILCS for the tall building at $Z = 2$ m, for $PM_{2.5}$. This case is based on data from February 15, 2009 at 6 a.m. when the flow is predominantly from the south. In Figure 8 (a), the deterministic ILCS is shown, as a baseline case. The wake structure is very pronounced downwind of building A. We also plot the case with eddy diffusivity, determined from our previous discussion of the models, in Figure 8 (d). This is our upper bound on stochasticity because it is valid for realistic

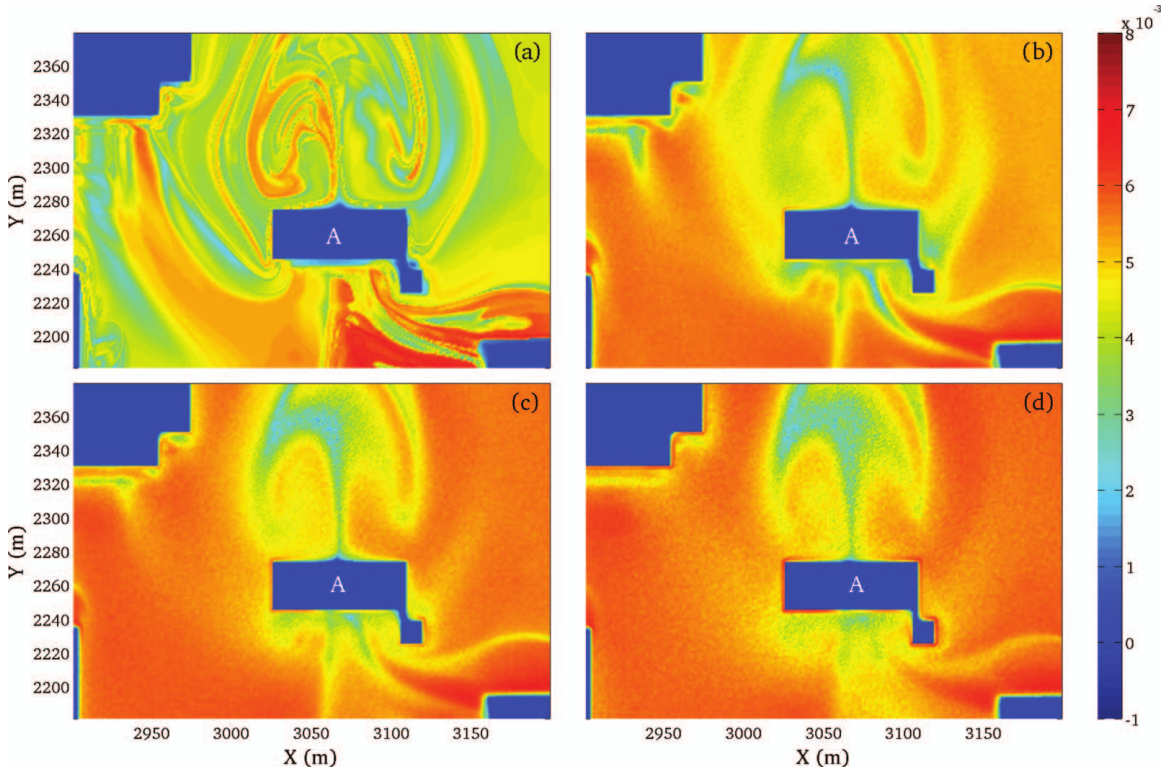

Figure 8. Forward-time stochastic ILCS near the tall building at $Z = 2$ m for PM2.5 on February 15, 2009. (a) Deterministic. (b) 0.25 of the full eddy diffusivity. (c) 0.5 of the full eddy diffusivity. (d) Full eddy diffusivity

flows. In between, in Figure 8 (b) and (c), we consider 1/4 and 1/2 of the value of the eddy diffusivity, as a proxy to understand the variation of ILCS due to strength of randomness. As seen, when randomness is progressively increased towards the full value of eddy diffusivity, the major wake structure remains quite distinguishable.

As a comparison, we also show in Figure 9 the backward-time stochastic ILCS in the same region. In the deterministic case, the mushroom-like wake structure trailing building A is clearly seen. At the southeast corner, due to the annex to building A, some closed structure is also seen as attractors. As we progressively increase stochasticity, the mushroom-like wake is still visible but fading, whereas the

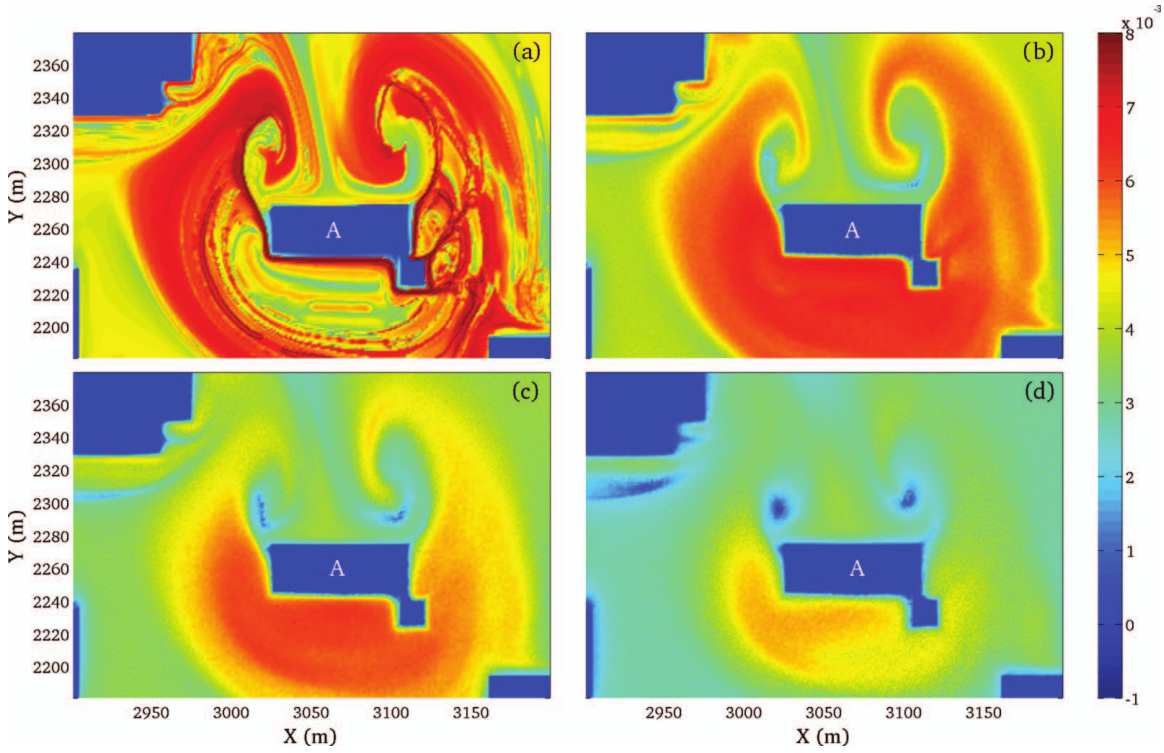

Figure 9. Backward-time stochastic ILCS near the tall building at $Z = 2$ m for PM2.5 on February 15, 2009. (a) Deterministic. (b) 0.25 of the full eddy diffusivity. (c) 0.5 of the full eddy diffusivity. (d) Full eddy diffusivity

smaller structure disappears even with 1/4 of the full stochasticity. Finally, at the full strength, only the counter-rotating vortex cell survives random perturbations.

In Table 1 we compute the correlation between the stochastic and deterministic FTLE fields to measure the variability of the ILCS by different levels of stochasticity. The correlation is computed as

$$C_{DS} = \frac{FTLE(D) * FTLE(S)}{Std[FTLE(D)] * Std[FTLE(S)]}, \tag{2.13}$$

where $FTLE(D)$ and $FTLE(S)$ are the scalar FTLE fields in the deterministic and stochastic cases, respectively. $Std[FTLE]$ denotes the standard deviation of the

Table 1. Correlation of stochastic and deterministic FTLE.

	Deterministic	Quarter	Half	Full
Forward	1	0.8463	0.8164	0.7896
Backward	1	0.8247	0.7581	0.7070

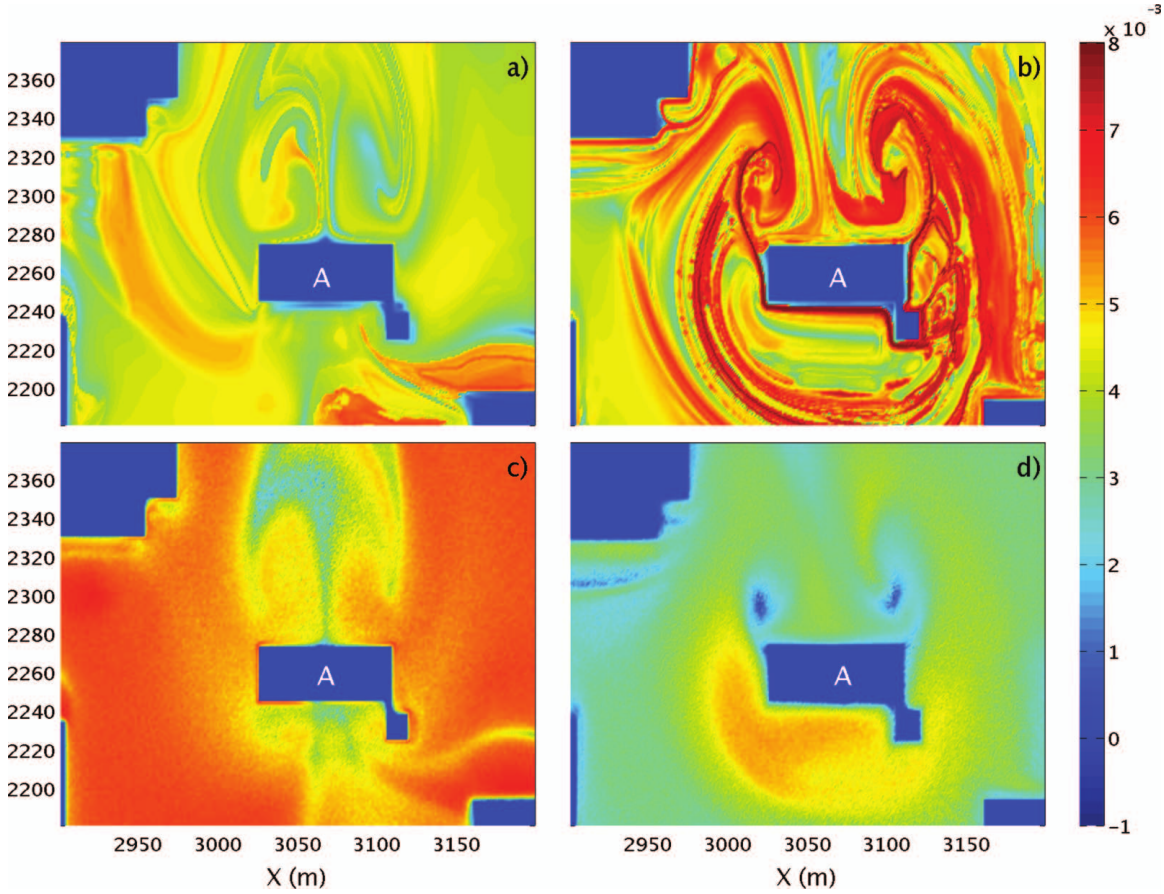

Figure 10. Comparison between deterministic and stochastic ILCS near the tall building at $Z = 2$ m for PM10. (a) Deterministic, forward-time. (b) Deterministic, backward-time. (c) Full eddy diffusivity, forward-time. (d) Full eddy diffusivity, backward-time.

scalar fields. As the stochasticity increases, the correlation decreases, but even with full stochasticity, correlation of the structures is still above 70%. This indicates the robustness of major ILCS.

We further study the variation of stochastic ILCS with respect to particle size

in Figure 10. In this figure, we compare the deterministic and fully stochastic cases directly. In the top panels, the forward-time (Figure 10 (a)) and backward-time (b) ILCS for PM_{10} are shown. Compared to the deterministic cases of $PM_{2.5}$, these ILCS are slightly less well-pronounced, but still quite well defined. For the stochastic cases, again, the major structures survive random perturbations and act as the organizing centers for nearby inertial particle trajectories.

2.5 Discussions and Conclusions

We have studied the mixing geometry for inertial particles in a realistic street-scale urban flow model. The model is focused in the Hermoso Park region in a district in Phoenix, Arizona. The interest is on how these geometry may relate to higher particulate matter density allegedly causing respiratory problems for local residents. We focus on the flow topology rather than specialized case studies because with such a geometry, we can estimate mixing patterns of pollutants from isolated release events anywhere inside the domain of interest. It also aids identification of patterns from continuous release events.

In order to objectively extract the mixing geometry, we used inertial Lagrangian coherent structures, because they offer objective description of transport patterns. For the deterministic case, the methodology is a direct application of results in (Sapsis and Haller 2009) and (Tang et al. 2009). We find the ILCS for different particle sizes and at different hours on January 16, 2009, with data initiated from measurements and flow simulated with QUIC-URB. The size effects on the structures have been discussed in detail. In particular, in the deterministic regime, as particle size becomes larger, attracting structures in the leading edge of large/individual buildings become

weaker. In addition, particle size also affects the dynamics in street canyons, in that trajectories are less likely to converge strongly, hence less mixing of the inertial particles are observed. These results provide the baseline cases for our discussions on stochastic ILCS.

For the stochastic case, we choose random displacement model, as it is simpler to analyze than Lagrangian stochastic models. The stochastic ILCS is understood in terms of the most likely trajectory an inertial particle will take as it evolves inside the urban flow with inhomogeneous random noise due to spatially dependent eddy diffusivity. The ILCS is then obtained from the mean motion. With this concept, backward-time random walk models are also meaningful, as an estimate of where a trajectory is most likely coming from in the past, so to estimate the tendency of attraction for each individual material particle. Evaluating the stochastic ILCS, we find that using eddy diffusivity based on $k - \epsilon$ model, major structures still survive to serve as the organizing centers for stochastic inertial particle transport. As we vary the strength of eddy diffusivity, a correlation with the deterministic geometry is also obtained.

Here, with the more homogenized FTLE field due to eddy diffusion, the extrema curves/surfaces (serving as ILCS boundaries) are less distinguished as their deterministic counterparts. However, bearing in mind that ILCS are regions in the flow where trajectories exhibit similar types of Lagrangian motion, we can readily identify regions in the FTLE field with similar data values as the stochastic ILCS. Hence, hyperbolic regions are highlighting patches in the FTLE field where stochastic mean trajectories are expected to separate the most, whereas elliptic regions are low-value patches where stochastic mean trajectories stay together. In terms of automated extraction of the boundaries of such structures, one would have to rely on the identification of material

lines on the steepest slopes in the FTLE field, as they mark the transition regions between most likely hyperbolic (plateaus in FTLE) and most likely elliptic (basins in FTLE) motion.

Note that the stochastic ILCS obtained with full eddy diffusivity are most robust and survive realistic disturbances, hence they are most likely to be found in a natural environment. Maps of stochastic ILCS such as those shown in Figures 8, 9, 10 can thus aid easy identification of strong elliptic or hyperbolic structures important for material transport. Subsequently, regions in the real urban environment which are most susceptible to pollutant accumulation or dispersal can be found for decision makers to take any air quality counter measures.

There are several aspects that could help improve our understanding of stochastic ILCS in a realistic urban environment. First, we have only used RDM for the stochasticity. In general, a LSM based on the Langevin equations is more suitable to account for the random nature of fluid trajectories. Conventional treatments of inertial effects are not directly using the governing Maxey-Riley equations, but an estimate of the finite synchronization time scale of inertial particles, which relates to an assumption that inertial particles travel at their settling velocities. A new formulation of the inertial dynamics based on Maxey-Riley equations with LSM (instead of RDM) on just the fluid trajectories may shed new light on stochastic inertial particle dynamics. Bearing the nicety of deterministic part of the inertial particle forces, we may use the approach outlined in this paper again for stochastic backward models. In this way, stochastic ILCS will be based on a more general formalism, and suited to more realistic environments.

Second, some careful treatments may also be needed for the boundary condition, since we are using a simple no-slip boundary condition and the results affect the

Gaussian assumption. An improved formulation may better estimate the statistics for inertial particle trajectories and bear a higher confidence in evaluating the stochastic ILCS.

Third, we the presence of coherent structures, the diffusion process inside the domain may not be Gaussian, and thus we need to consider other choices of random noises to better reflect reality. Some of these non-Gaussianity has been incorporated into QUIC-PLUME for idealized fluid tracers, and we will need to formulate carefully in the case of inertial particles.

Overall, since particle density is a linear superposition of release events, the precise knowledge of geometry will aide fast estimates on the source and fate of dispersion for pollutants, chemical spills or malicious toxin released. The use of mixing topology will aid environmental protection, mitigation, and homeland security applications. How to efficiently use ILCS in such applications will be explored in future studies.

Chapter 3

LAGRANGIAN COHERENT STRUCTURE ANALYSIS OF TERMINAL WINDS: THREE-DIMENSIONALITY, INTRAMODEL VARIATIONS, AND FLIGHT ANALYSES

The next two chapters are concerned with a Lagrangian approach windshear detection at the Hong Kong International Airport. Chapter 3 is drawn from (Knutson, Tang, and Chan 2015).

Published in: Advances in Meteorology

Brent Knutson, Wenbo Tang, and Pak Wai Chan

We present a study of three-dimensional Lagrangian coherent structures (LCS) near the Hong Kong International Airport and relate to previous developments of two-dimensional (2D) LCS analyses. The LCS are contrasted among three independent models and against 2D coherent Doppler light detection and ranging (LIDAR) data. Addition of the velocity information perpendicular to the lidar scanning cone helps solidify flow structures inferred from previous studies; contrast among models reveals the intramodel variability; and comparison with flight data evaluates the performance among models in terms of Lagrangian analyses. We find that, while the three models and the LIDAR do recover similar features of the windshear experienced by a landing aircraft (along the landing trajectory), their Lagrangian signatures over the entire domain are quite different - a portion of each numerical model captures certain features resembling those LCS extracted from independent 2D LIDAR analyses based on observations.

3.1 Introduction

A Lagrangian framework for terminal wind hazard detection near Hong Kong International Airport (HKIA) has been recently developed and locations of such disturbances have been compared against flight data (Tang, Chan, and Haller 2010, 2011a, 2011b). The approach outlined in this series of work focuses on obtaining signatures of convergence and divergence of fluid parcel trajectories based on two-dimensional (2D), near-ground velocity data retrieved from light detection and ranging (LIDAR) equipment (Chan and Shao 2007). The disturbances extracted from the Lagrangian methods are found to be in close proximity of real jolts experienced by landing aircraft. Validating with lengthy flight data over several months, it is found that this approach outperforms Eulerian measures, such as velocity fluctuation measurements (Chan and Lee 2012), as they provide better Receiver Operating Characteristic (ROC) graphs (Kafiabad, Chan, and Haller 2013; Fawcett 2006), and matches closely with an operational algorithm based on a scanning pattern the follows the actual aircraft landing trajectories (Chan, Shun, and Wu 2006).

One limitation of the aforementioned methodology is the lack of three-dimensional (3D) data from the 2D LIDAR output. Indeed this is a common limitation shared by all other methods based on 2D LIDAR data, and the Lagrangian framework outperforms traditional methods in part due to its capability to better infer the signatures transversal to the 2D plane-position-indicator (PPI) scanning cone. Variational wind retrieval algorithms in three-dimensions are also available (Sun, Flicker, and Lilly 1991; Qui and Xu 1992; Qiu et al. 2006), but they are more time-consuming and relevant to operational forecasts at HKIA, and PPI scans are only available at a few

elevation angles. Henceforth, it is beneficial to verify that sophisticated results based on 2D data are useful in operational applications.

In this study, we aim to explore to what extent the transversal signatures inferred from 2D scans represent the true 3D structures - Do we find correspondence of 3D vertical structures at the locations where 2D convergence and divergence are the strongest, at least near the center of the LIDAR scanning cone? Does this interpretation successfully extrapolate to data at the peripheral of the LIDAR scanning cone, where the vertical elevation could be over 1000 meters above mean sea level, and an argument of strong two dimensionality near ground may not apply? What extra information does 3D data reveal that is absent from 2D analyses?

Towards this end, we have generated three independent numerical simulations of the regional atmospheric flows near HKIA, for a case of strong windshear on December 27, 2009. This case corresponds to an airstream associated with a ridge of high pressure along the southeastern coast of China meeting a cold front from inland, resulting in aircraft diverting to Shenzhen because they could not land at HKIA (Chan 2012). Two of the simulations are based on numerical weather prediction models - the Regional Atmospheric Modelling System (RAMS) (Pielke, Cotton, and Walko 1992) and the Weather Research and Forecasting model (WRF) (Skamarock and Klemp 2008); the third simulation uses the FLOWSTAR package, which is analytically based and depends more on the terrain data than the physics (Carruthers, Hunt, and Weng 1988). In terms of the initialization of the simulations, the two weather forecast models are driven by global forecast system (GFS) data (Sela 1980) and use nested grids to achieve high resolution over HKIA, whereas the latter uses upstream observational data (independent from LIDAR) as the constant boundary conditions for computation of a steady state solution.

To realize our goal on validation of the 2D analyses, we make the following comparisons. Firstly, we contrast LCS among different models to obtain a full picture of the 3D flow structures. This comparison reveals the variability among models. Secondly, within each model, we compare LCS obtained from full 3D data to those derived from 2D wind fields interpolated on the LIDAR scanning cone. Two schemes are considered for the 2D data generation. One is the horizontal wind speed interpolated directly from 3D model. This wind field closely mimics the resolved model flow, so the comparison directly reflects 2D signature of a 3D field. The other uses line-of-sight (LOS) velocity from the models and goes through the 2D wind retrieval scheme (Chan and Shao 2007). This retrieved wind is then used to generate 2D LCS. This effectively mimics the procedure for LIDAR measurements-LCS generation. Consequently 2D information loss and modeling assumed in the wind retrieval scheme are tested with 3D data. Thirdly, we contrast the 3D and 2D LCS from models with 2D LCS obtained from the actual LIDAR measurements to check for any correspondence. Lastly, we compare the LCS from these analyses with data collected from a landing aircraft. This brings all models and schemes to the ultimate test for possible operational implementation.

The rest of this chapter is organized as follows. In section 3.2 we briefly review the wind retrieval, extrapolation, and LCS generation algorithms. In section 3.3 we introduce the three numerical model data sets. In section 3.4 we discuss the various comparisons among 3D, 2D, and measurement data. In section 3.5, we draw conclusions and discuss further studies underway.

3.2 Wind Retrieval and LCS Generation Algorithms

We briefly summarize the algorithms used to generate 2D wind retrieval from LIDAR scans and to extract LCS based on the retrieved data. The 2D wind retrieval algorithm for LIDAR is modified from a two-step variational method for RADAR (Qiu et al. 2006). The cost function J to be minimized is given by

$$\begin{aligned} J(u,v) =& J_1 + J_2 + J_3 + J_4 + J_5 + J_6 \\ & \sum_{i,j} W_1[(u-u_b)^2 + (v-v_b)^2] \\ & + W_2(v_r - v_r^{obs}) + W_3(\Delta x)^2 \left(\frac{\partial u}{\partial x} + \frac{\partial v}{\partial y}\right)^2 \\ & + W_4(\Delta x)^2 \left(\frac{\partial v}{\partial x} - \frac{\partial u}{\partial y}\right)^2 + W_5(\Delta x)^4 \left(\nabla^2 u + \nabla^2 v\right)^2 \\ & + \sum_n \left[W_6 \left(\frac{\partial v_r^{obs}}{\partial t} + u\frac{\partial v_r^{obs}}{\partial x} + v\frac{\partial v_r^{obs}}{\partial y} \right)^2 \right], \end{aligned} \tag{3.1}$$

where u and v are the components of the retrieved field, subscript B is the background field, generated from LIDAR radial velocity in the way described in (Qiu et al. 2006), v_r is the retrieved radial velocity, superscript obs is the observed values, i and j are the horizontal grid point, and n is the time index (three consecutive scans are used in each analysis). The weights are $W_1 = 0.1$ (after the first step retrieval), $W_2 = 1$, $W_3 = W_4 = W_5 = 0.1$, and $W_6 = 10^4$. They are chosen empirically in this paper to ensure that the constraints have proper orders of magnitude. The model-emulated LOS velocity is subject to this retrieval algorithm for emulated 2D wind and subsequent LCS analyses. For more discussions of this algorithm, the readers are referred to (Tang, Chan, and Haller 2011a; Chan and Shao 2007).

The retrieved wind is extrapolated beyond the LIDAR resolved range as a global linear flow that best fits the 2D wind retrieval (Tang, Chan, and Haller 2010). This

best reveals the nonlinearity inside the LIDAR observational domain while it avoids addition of extra nonlinearity from data outside when they are completely unknown. In terms of the current study, this extrapolation is applied to the true and emulated LIDAR data (so as to measure the performance of the 2D LCS retrieval algorithm). The numerical models have data coverage outside of the LIDAR range and those data are used in the 3D computations as they provide the true LCS pertinent to the corresponding velocity fields.

For a Cartesian grid $\mathcal{G}$ in a rectangular region, where the coordinate axes have been chosen such that the domain center corresponds to the origin, the closest linear incompressible flow which minimizes error in the Euclidean norm is

$$\boldsymbol{v}_L(\boldsymbol{x},t) = \begin{pmatrix} \frac{\langle xu_1 - yu_2\rangle}{\langle x^2+y^2\rangle} & \frac{\langle yu_1\rangle}{\langle y^2\rangle} \\ \frac{\langle xu_2\rangle}{\langle x^2\rangle} & \frac{\langle yu_2 - xu_1\rangle}{\langle x^2+y^2\rangle} \end{pmatrix} \boldsymbol{x} + \begin{pmatrix} \langle u_1\rangle \\ \langle u_2\rangle \end{pmatrix} \tag{3.2}$$

where $\langle g\rangle = \sum_{i=1}^{m}\sum_{j=1}^{n} g(x_i,y_j)/(m\times n)$ is the spatial average of a function g over the grid $\mathcal{G}$.

The global flow is constructed on the whole plane by letting

$$\boldsymbol{v} = \boldsymbol{v}_L + (\boldsymbol{u} - \boldsymbol{v}_L)f, \tag{3.3}$$

where f is a filter function that takes value 1 inside a subset of $\mathcal{G}^0$ of $\mathcal{G}$ and value 0 in the exterior of $\mathcal{G}^0$. In between we have a buffer zone of with Δ where f smoothly transitions between 1 and 0. This allows smooth trajectories to leave the LIDAR domain.

We use a common measure, the finite-time Lyapunov exponents (FTLE), to reveal the LCS field.

An auxiliary grid approach is used to approximate the FTLE field with better accuracy (Farazmand and Haller 2012). Also, trajectories near ground are allowed to slide along the surface with horizontal velocity at 10m. This helps remove structures due to the no-slip boundary conditions and better reveals the structures more relevant to airflow disturbances that affect the airport.

The FTLE field (Tang, Chan, and Haller 2011b) and its associated gradients (Kafiabad, Chan, and Haller 2013) have been used to compare LCS signatures of airflow hazard and jolts experienced from flight data. We will contrast the LCS analyzed here with flight data for the corresponding event in a similar fashion in section 3.4.

3.3 Numerical Model Data for the Windshear Event

The numerical model data based on RAMS and FLOWSTAR have been reported previously (Chan 2012; Carruthers et al. 2014), but they focus on comparisons between the headwind profile from measurements onboard a flight and in numerical predictions. Both models capture the general trend of the measured headwind profile. In this study, these two model data sets, along with a third one using WRF, are used for LCS analyses.

The RAMS model is nested within the 20 km resolution Operational Regional Spectral Model (ORSM) of the Hong Kong Observatory (HKO). RAMS was run with nested grids having spatial resolutions of 4 km, 800 m, and 200 m with two way nesting. The smallest nest is sufficient to resolve the mountains on Lantau Island, immediately south of HKIA. The Mellor-Yamada turbulence parameterization scheme

was used in the first grid and the Deardorff scheme in the other two grids. The model run started at 1200 UTC, 26 December 2009, and was carried out for 12 h.

The FLOWSTAR model is based on topographic data and meteorological inputs and generates steady-state solutions of velocity. The boundary conditions for the FLOWSTAR runs were defined using the observed 10 m wind upstream of Lantau Island and by the radiosonde ascent for midnight 27 December 2009 at King's park for the wind speed and direction, vertical temperature structure, and hence buoyancy frequency. Three cases were considered for the wind speed and direction and boundary layer height. In this study we use the data set that best matches the measured headwind profile. This corresponds to an upstream wind speed of 7.3 ms^{-1} at $z = 10$ m height, wind direction of 140°, a boundary layer height of $h_0 = 400$ m, buoyancy frequency profile $N = 0$ s^{-1} for heights $z < h_0$, $N = 0.0124$ s^{-1} for heights $z > h_0$, temperature step of 7.19° C at $z = h_0$, and surface roughness of 0.5 m. The readers are referred to (Chan 2012; Carruthers et al. 2014) for more thorough discussion of these two models.

Finally, the WRF model is initiated from GFS data and runs with nested grids having spatial resolutions of 51.2 km, 12.8 km, 3.2 km, 800 m, and 200 m with two-way nesting. The model is centered at 22.313 N and 113.92 E. In an attempt to match the high horizontal resolution, each nest also had 85 vertical levels. In the 3 coarsest grids the YSU (Yonsei University scheme) boundary layer parameterization was used, whereas in the 3 finest resolution nests the boundary layer parameterization was turned off in order to have full 3D diffusion. Full diffusion (diff_opt=2) was selected, paired with the 1.5 order TKE prediction for turbulence parameterization. Each nest used the Dudhia shortwave radiation and RRTM longwave radiation schemes. Five-layer thermal diffusion was used as the land surface option, whereas the MM5

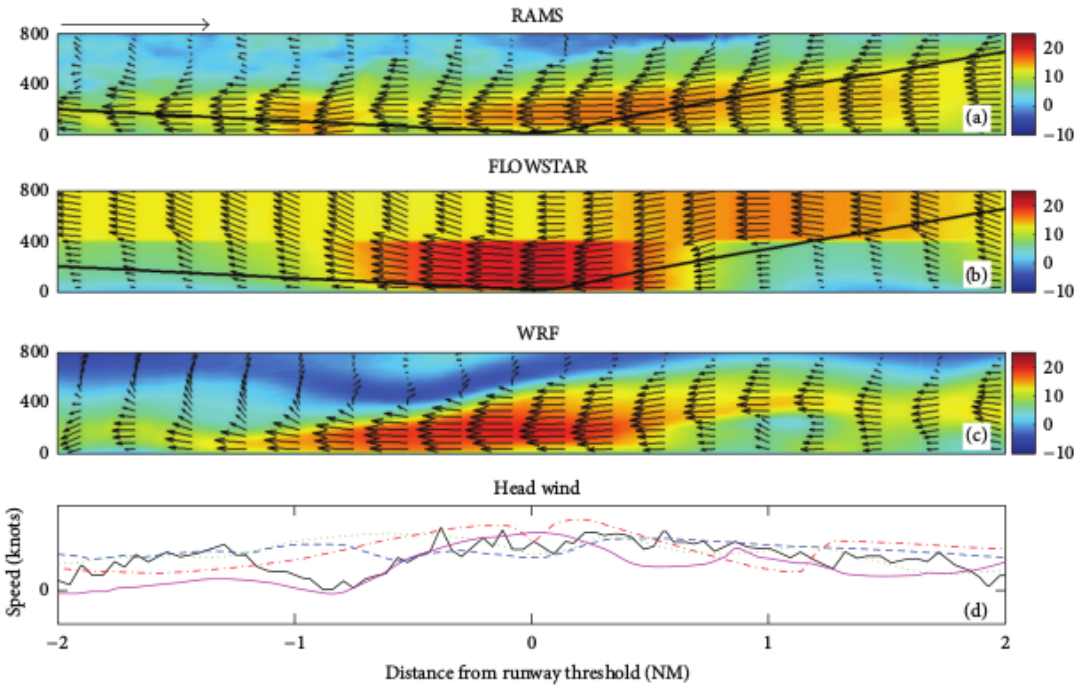

Figure 11. (a)-(c) Horizontal wind speeds (in knots) for RAMS, FLOWSTAR, and WRF, respectively, along the landing corridor. The thick black solid curve in each figure is the landing trajectory. The vector field is the plot of headwind and vertical velocity along the landing corridor, where hints of coherent structures can be seen. (d) Headwind comparison between measurements and models. Thick black solid curve: onboard measurement. Magenta curve: LIDAR measurements along the PPI scanning cone. Blue dashed curve: interpolated headwind from RAMS. Red dash-dot curve: interpolated headwind from FLOWSTAR. Green dotted curve: interpolated headwind from WRF. The black arrow above (a) indicates direction of flight.

similarity scheme was selected for the surface layer and the Kessler scheme was used for microphysics. No cumulus parameterization was used. The simulation was initiated at 1800 UTC, 26 December 2009, and ran for 6 h.

As a first comparison, we contrast some Eulerian velocity data among the models and measurements in Figure 11, for a case of missed approach. The approach is from

left to right, as indicated by the black arrow about Figure 11 (a). Figure 11 (a)-(c) how comparison of the headwind for the three numerical models along the landing corridor. The aircraft trajectory is also shown in each of the panels as the thick solid black curve. It is seen that all three models capture a region of strong headwind near the runway threshold. Flying through this patch leads to significant windshear. The two regional models appear to capture the same trend of the patch from bottom left to top right. This patch is more columnar in the FLOWSTAR data. The sharp transition in the FLOWSTAR model at 400 m indicates the height of the inversion layer. To better infer the flow topology, we use the velocity vectors projected onto the vertical plane of the landing corridor (headwind and vertical velocity). It seems that RAMS has the weakest vertical velocity in this plane; FLOWSTAR shows more wave undulation as the aircraft approaches the runway threshold, yet WRF shows a hint of flow reversal at -1 NM from the runway threshold between 300 and 500 m in altitude. This feature possibly leads to strong LCS. In Figure 11 (d), the headwind profile is shown from different data sets. In this panel, the thick black solid curve is the actual measurements of headwind onboard the landing aircraft. The magenta curve shows the headwind profile extracted from LIDAR conical scans. This data closely follows the velocity ramp from onboard measurement at about -1 nautical mile (NM) from the runway threshold. The blue dashed curve (RAMS), red dash-dotted curve (FLOWSTAR) and green dotted curve (WRF) differ from the onboard measurement further, but they do capture the general trend of the windshear (with weaker velocity gradients). A cross correlation study shows that, at the respective maxima, the LIDAR data is 71% correlated with onboard head wind measurements, followed by WRF (63%), FLOWSTAR (62%), and RAMS (56%). Lagrangian signatures of these resolved flow data are discussed in the following section.

3.4 LCS Comparisons

Before comparison with 2D data sets, we first analyze the 3D LCS structure from various models and their implications on the actual terrain-induced turbulence patches.

3.4.1 Three-Dimensional Features of LCS

The three-dimensional features of the LCS for the three data sets are shown in Figure 12. These features are highlighted with two vertical slices in the domain. One vertical slice is along the southern runway, highlighting structures the airplane experiences when landing. The other vertical slice is perpendicular to the southern runway, so features transveral to the runway can be seen. The airplane landing trajectory is shown in each of the panels as the thick black curve. Direction of flight is again marked by a red arrow in Figure 12 (a), along the vertical slice aligned with the southern runway. Relevant positions of this trajectory with the coherent structures, the Lantau Island, and the airport are readily seen. The red dots at sea surface height in each panel mark the distances for each nautical mile from the runway threshold, which is located at the lowest point of the plane trajectory. To aid in the interpretation of the coherent structures, selected fluid parcel trajectories (thin black curves with black arrows) near ground around the airport are also shown to reveal the actual atmospheric motion. These trajectories are generated from the time-dependent velocity data in each of the flow models and they interact with the airplane near the runway threshold.

Figure 12 (a) and (d) shows FTLE obtained from RAMS, (b) and (e) FTLE obtained from FLOWSTAR, and (c) and (e) FTLE obtained from WRF. The first

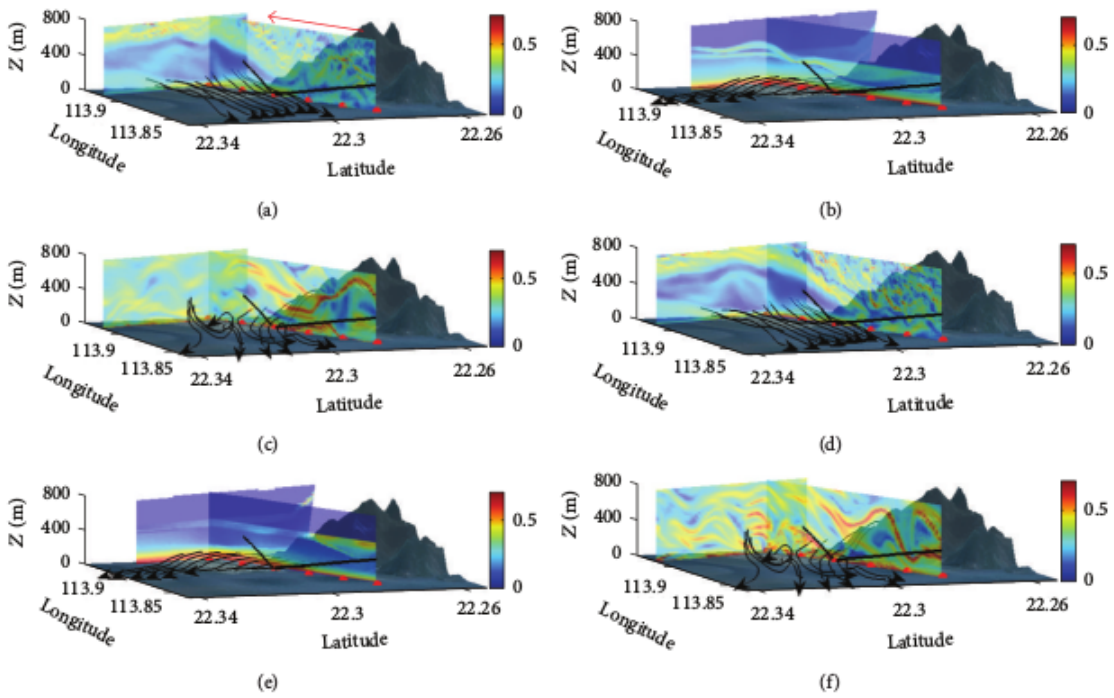

Figure 12. Lagrangian coherent structures from different data sets and their relative positions to the Lantau Island. The opaque color maps are the vertical slices of the FTLE fields along and perpendicular to the runways, intersecting at the southern runway threshold towards the west. The thick black curve in each panel is the airplane landing trajectory. The thin black curves are fluid trajectories highlighting the structures, with black arrows indicating direction of flow. The panels are: (a) RAMS, forward-time FTLE. (b) FLOWSTAR, forward-time FTLE. (c) WRF, forward-time FTLE. (d) RAMS, backward-time FTLE. (e) FLOWSTAR, backward-time FTLE. (f) WRF, backward-time FTLE. The red arrow indicates direction of flight. The red dots on sea surface level mark every nautical mile towards the runway threshold. The runway threshold is located at the lowest point of the flight trajectory.

panel for each shows the forward-time FTLE field, highlighting separation, the second shows the backward-time FTLE, highlighting attraction. The integration time for these FTLE fields is 6 minutes. This is sufficient to capture short-term flow structures that will be averaged out during long term integrations, yet important for flight safety. It is also consistent with the integration time from 2D velocity data, so the features among these data sets can be directly compared. Judging from the orientation of the structures, it can be seen that the two regional atmospheric models (RAMS and WRF) behave quite similarly, with wavy structures between 400 and 600 m altitude (cf. (a), (d), (c), and (f). The vertical slices are shown up to 800 m). Some structures are also seen near the bottom around the airport, and between 200 and 400 m relatively less separation is seen. The FLOWSTAR data carries less structures ((b) and (e)) regarding the fact that major features are seen near the bottom and around 400-500 m, with low separation in between these heights. These distinguished structures in FLOWSTAR data can be explained due to strong shear across the inversion layer.

We closely inspect the fluid particle trajectories to further interpret the structures. Consistent with the respective velocities, the RAMS ((a) and (d)) and WRF ((c) and (f)) data show easterlies/east-southeasterlies, whereas the FLOWSTAR data shows a southeasterly. In RAMS data, several streaks of waves along the runway can be identified; their nonlinear motion leads up to the corrugated patches seen near the bottom of the domain. The FLOWSTAR data shows little horizontal separation of trajectories, but some vertical motion can be identified. The WRF data is the most interesting, as several vortex rolls aligned roughly in the east-west direction can be identified, some of which cross the runway threshold.

Overall, the two regional models show good correspondence between the data, with the exception of that the vertical velocity in RAMS seems to be less than that of

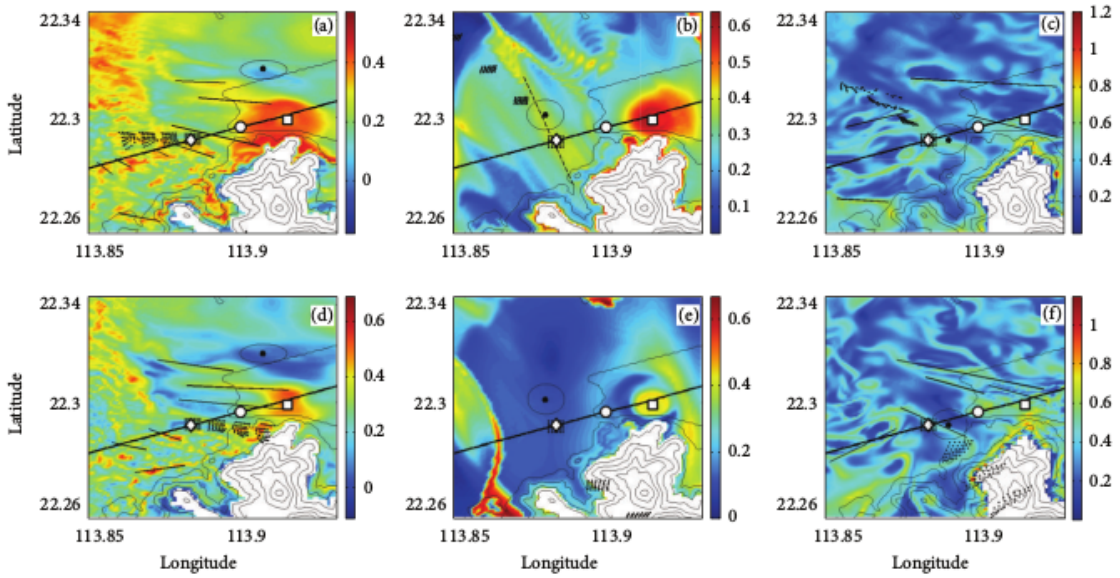

Figure 13. FTLE fields interpolated on the LIDAR scanning cone. The panels are, from left to right, data from RAMS, FLOWSTAR, and WRF, respectively. The top panels are the forward-time FTLE and the bottom panels are the backward-time FTLE. The black straight lines mark locations of great similarity in FTLE with Figure 14 , and the black circles mark locations of a few mismatches with Figure 4.

WRF. As comparison, the FLOWSTAR data show less detailed features of coherent structures, probably due to the heavily idealized assumptions.

3.4.2 Comparisons between Full and Conical LCS

We employ two schemes to contrast the LCS from fully 3D data and 2D emulated data. In the first scheme, 3D LCS are interpolated along the LIDAR scanning cone and compared to those generated from 2D velocity along the same cone. This scheme reveals whether it will be plausible to use 2D information to infer 3D structures. To further mimic the process of generating LCS from LIDAR line-of-sight (LOS) velocity, the second scheme emulates LOS velocity scans from simulation data and generates 2D wind retrieval and then finds the coherent structures. These results are also compared

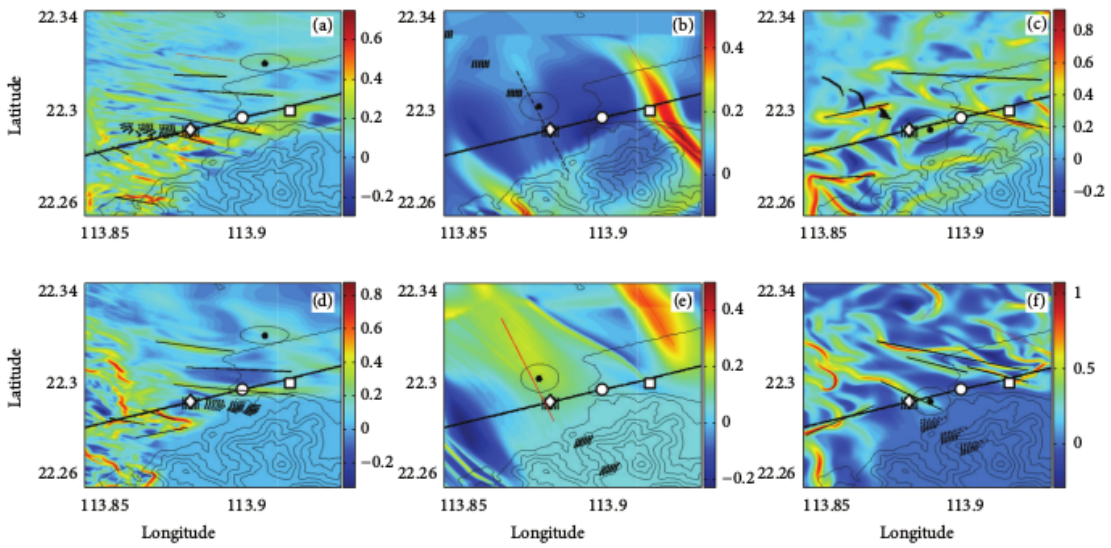

Figure 14. FTLE fields interpolated on the LIDAR scanning cone. The panels are, from left to right, data from RAMS, FLOWSTAR, and WRF, respectively. The top panels are the forward-time FTLE and the bottom panels are the backward-time FTLE. The black straight lines and the black circles mark the same locations as seen in Figure 13 for reference.

to actual LIDAR based FTLE. For easy handling of lack of data when the LIDAR scanning cone intersects with mountain topography, we use the FDFTLE algorithm (Tang, Chan, and Haller 2010) to extend the data and allow smooth integration of trajectories. This avoids artificial structures associated with trajectories running into Lantau Island. In this subsection, the three model flows are considered, and the benchmarks and the 2D LCS are approximations to these benchmarks.

We show in Figure 13 the FTLE fields interpolated along the LIDAR scanning cone. This figure serves as the reference for comparisons with approximations. The panels are similar to Figure 12, with the left, center, and right columns corresponding to RAMS, FLOWSTAR, and WRF data sets, and the top and bottom rows correspond to the forward and backward time integrations. The integration time is 6 minutes. For easy comparison and feature identification we only focus on a region immediately west

of the southern runway threshold (threshold marked by the black circle), corresponding to the smallest nest in RAMS simulation. The topography near the airport is shown as the black isocontours and the landing trajectory is shown as the thick black line. The southern LIDAR (square) and -1 NM before the runway threshold (diamond), where a strong windshear was reported, are also marked for comparison. As seen, the two regional models show similar features of flow structures, especially near the southern LIDAR, with some east-west ridge structure above the west end of the airport. This consistency could be due to both models being driven from global model data, and hence they bear similar features fro the larger nests towards the smallest nests. Further away from the airport, the WRF data shows more coherent patterns indicating more organized convergence and divergence of flow, whereas the RAMS data shows more scattered features, indicating less organized separation. The stronger coherence in WRF data could be due to the stronger vertical velocity (cf. Figure 11 and trajectory comparisons in Figure 12 giving rise to better defined vortex rolls. The FLOWSTAR data is oriented slightly towards the north-west, consistent with the incoming flow direction. The arc pattern on the left end of this data set is due to the transition of structures from below to above the inversion layer, where strong shear gives rise to a highlighting layer of separation, as seen in Figure 12 (b) and (e). Below this layer (inside the arc towards the LIDAR), some features of the forward time FTLE can still be identified (Figure 13 (b)). In all models, the strong windshear at -1 NM can be associated with coherent structures highlighted as the FTLE ridge.

To better understand the role of highlighting FTLE at -1 NM, we plot groups of black dots, indicating positions of fluid parcels every 2 minutes. These trajectories are initiated at the diamond, at 190 m elevation, where the windshear is reported. The initial height of the trajectories is determined based on the elevation of the PPI

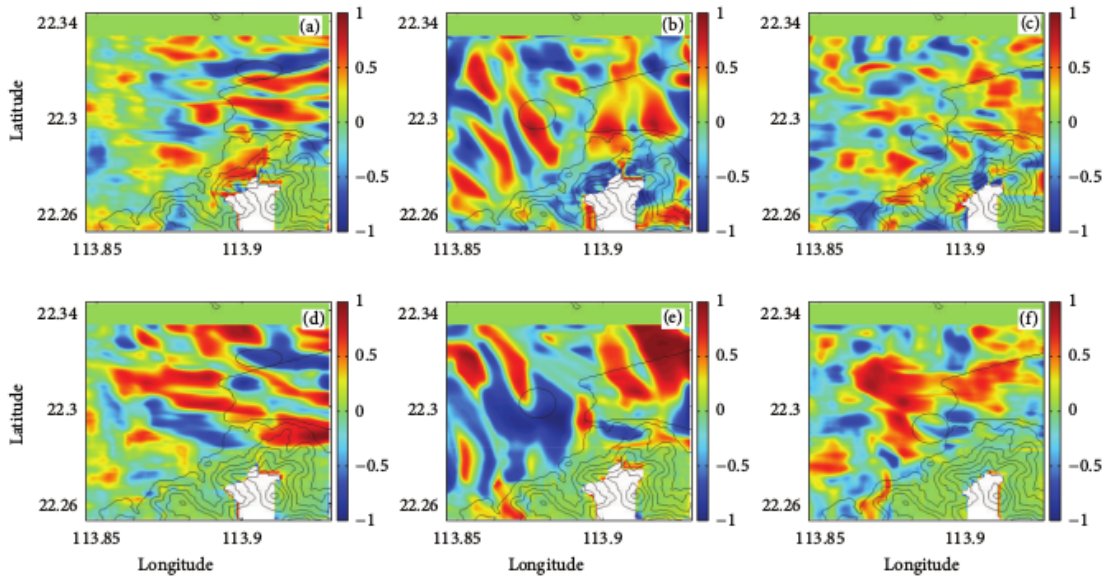

Figure 15. Localized correlation map between Figures 13 and 14. The sizes of the local regions are 1 km × 1 km patches. The black circles mark the mismatches discussed in Figures 13 and 14.

scanning cone at this location. The trajectories are integrated using the full 3D data. The deformation of these dots indicates the local nonlinear behaviors of the flow. As seen, in RAMS data in Figure 13 (a) and (d), there is trajectory separation transversal to the local structures in both forward and backward time, resulting in the FTLE ridges nearby. The forward time trajectories in FLOWSTAR data show very weak stretching associated with a low FTLE value ridge. The backward trajectories of FLOWSTAR mostly show contraction in the meridional direction and very weak separation in the zonal direction, hence giving no highlighting structure near the -1 NM location. The WRF trajectories show stretching along a local structure in forward time and attraction transversal to a local structure in backward time. As such, all FTLE behaviors are accounted for with the behaviors of the local trajectories.

In Figure 14, we show these 2D results using horizontal wind data on the PPI scanning cone. For easy comparison, the layout is precisely the same as those in

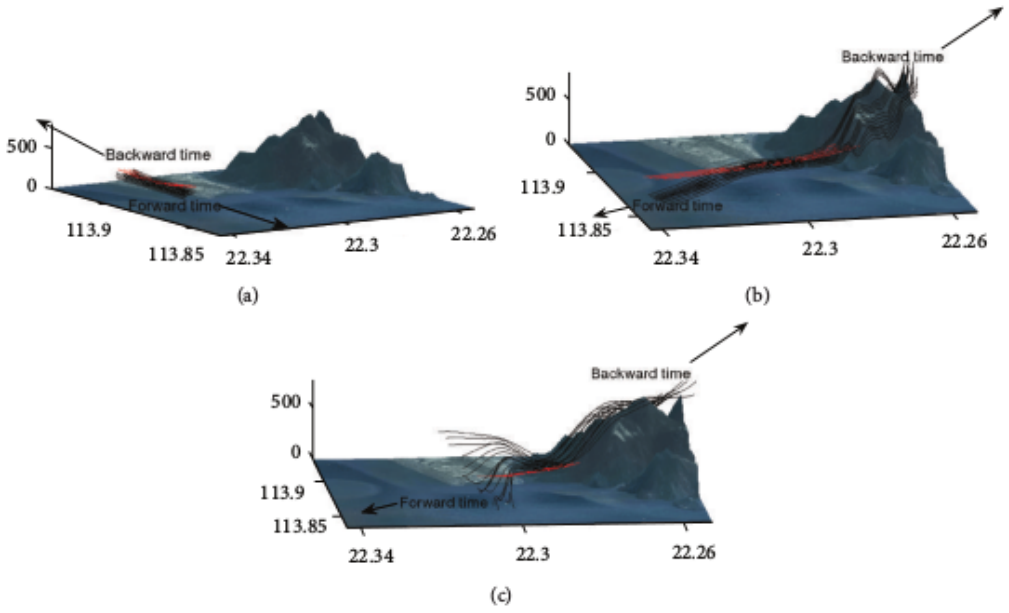

Figure 16. Trajectory comparison between 3D data and 2D data on the LIDAR cone. The panels are: (a) RAMS. (b) FLOWSTAR. (c) WRF.

Figure 13. The data sets are, left to right, RAMS, FLOWSTAR, and WRF. Plots in the top row show forward time structures and plots in the bottom row show backward time structures. Trajectories near -1 NM from runway threshold based on the 2D interpolated data are again shown to explain the local FTLE behavior and compare to those in Figure 13. It can be seen that the shapes of local deformation of the trajectories are similar to those in Figure 13.

To better quantify the match between Figures 13 and 14, we use a local correlation map. Because flow structures relevant to flight operations are relatively small, we compare features of size 1 km $\times$ 1 km. The correlation between the 3D interpolated and 2D FTLE fields of each patch of 1 km^2 is computed at each patch center and plotted in Figure 15. The layout is the same as the previous two figures for the three data sets and two directions of integration. In regions of red color, there is a match

between features, whereas in regions of blue color, there are mismatches. This leads to the question of what kind of three-dimensionality leads to the discrepancy in these two plots. Before explaining such discrepancies, we first locate regions where strong similarities can be found. The thick black line segments in Figures 13, 14 correspond to structures where correspondence can be found between 2D and 3D extraction. Such correspondence is mainly seen in RAMS and WRF data, near the LIDAR (marked by the square). This can be explained by the local two-dimensionality near the ground, around the center of the LIDAR scanning cone. At -1 NM and beyond, the LIDAR scanning cone is already at 190 m. Structures may vary strongly below the cone, resulting in the mismatch between the 3D and 3D analyses. There is a weak ridge in the 2D computation that could be related to the more pronounced ridge in 3D analyses. We use the thin dashed line to identify this possible match.

In order to understand the discrepancies in the 3D and 2D analyses, we focus on a few regions where the mismatch is pronounced. These regions are highlighted by the black ellipses in Figures 13 and 14, with centers marked by the black dots (note their correspondence in the blue regions in Figure 15). We are not concerned with the big red spot near LIDAR because it is due to vertical shear near ground arising from the no-slip boundary condition (even though we allowed trajectories to continue to flow at the speed of 10 m height, the horizontal velocity is still significantly lower than those in higher elevations). For RAMS data, the two analyses are quite similar, and hence we choose an FTLE structure that is absent in the 3D analyses yet present in the 2D analyses. This region is only about 1 NM northwest of the LIDAR; hence being able to interpret this structure helps us understand possible conflicts near 100 m elevation. For FLOWSTAR data, we choose a region immediately north of the -1 NM location. As indicated above, the match in forward time structures is with questions

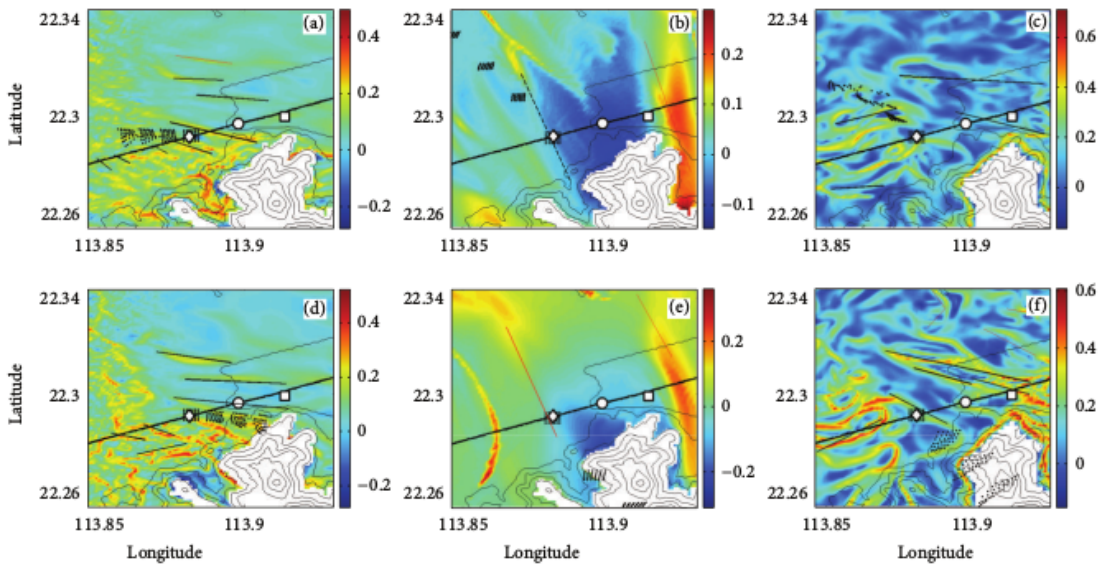

Figure 17. FTLE fields computed from just horizontal stretching. The panels are, left to right, data from RAMS, FLOWSTAR, and WRF, respectively. The top panels are the forward time FTLE and the bottom panels are the backward time FTLE.

and the backward time structure does not show much correspondence at this location. For WRF data, to the east of the -1 NM location, the 3D analyses show a structure transveral to the landing trajectory yet 2D analyses show a structure aligned with the landing trajectory. We focus on this region to see what trajectory behaviors lead to these results.

We explain the difference in the plots in Figure 16, for the three data sets. In all three panels, trajectories based on 3D data are shown in black, and trajectories based on 2D data are shown in red. The directions of flow are indicated by the text arrows. In Figure 16 (a), there is probably only weak horizontal separation in the 3D trajectories (note that the FTLE value is not 0 at this location in Figure 13 (a)). The trajectories just follow a wave undulation across the airport in the east-west

direction. Because 2D trajectories leave the domain and use linear extrapolation, it gives rise to a bit larger stretching and a local FTLE ridge. From Figure 16 (b), it is seen that trajectories in FLOWSTAR data also bear very weak horizontal separation. The ridge structure in Figure 13 (b) is mainly due to such a weak separation. The horizontal discrepancies in the backward time trajectories are better seen in Figure 13 (e) and Figure 14 (e). Both show a bit of separation in the visible domain. As the trajectories leave the domain, the 3D trajectories follow an external shear flow that has no separation (given as the upstream condition), yet the 2D trajectories again undergo a linear extrapolation, where trajectories continue to separate, giving rise to the slightly larger FTLE value seen in Figure 14 (e). The most interesting comparison is in Figure 16 (c) for WRF data. Here, a large vertical displacement is seen in the forward time trajectories. In the 3D trajectories, towards the northeast of the examined initial conditions, the trajectories go underneath those starting towards the southwest. Those starting towards the southwest pick up elevation quickly and form large separation both vertically and horizontally. In fact these trajectories are caught in a local vortex roll. The LIDAR scan sees first horizontal contraction (as the east and west trajectories flip over) at low elevation near the LIDAR and then horizontal separation in the higher elevation (as the west trajectories rotate with the vortex roll). As seen, the incorporation of the vertical stretching contributes to significant change of structure at this location.

In the context of flight operations, horizontal windshear is of more concern as it directly relates to the lift of the airplane, the vertical separation could be due to nonparallel shear leading nearby vertical trajectories into vastly different positions. The airplane is less sensitive to this kind of separation. As such, we compute a partial FTLE field, based on the separation of nearby horizontal trajectories (which

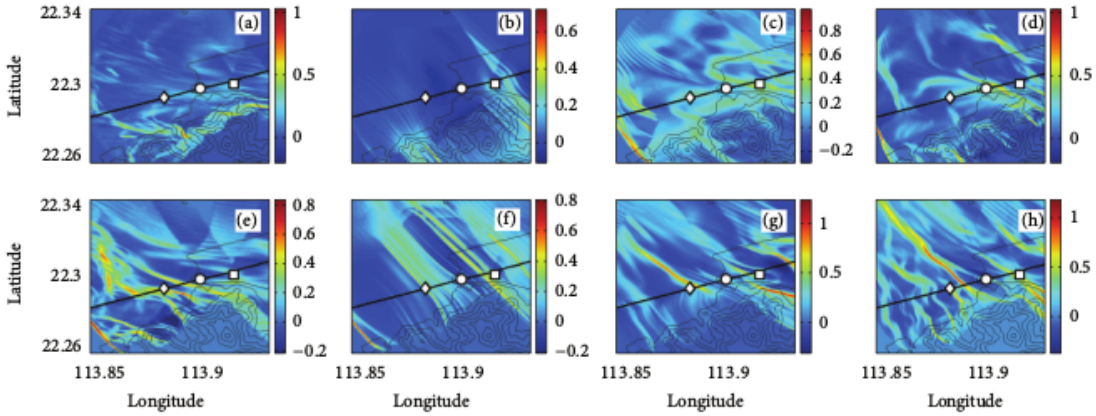

Figure 18. FTLE fields computed from LOS velocity and 2D variational retrieval. The panels are, left to right, data from RAMS, FLOWSTAR, WRF, and LIDAR, respectively. The top panels are the forward time FTLE and the bottom panels are the backward time FTLE.

are advanced with the full 3D velocity). This measure excludes the effects of direct vertical separation but does incorporate horizontal separation as the trajectories enter different elevations. Its use in atmospheric flows has been justified in (Tallapragada, Ross, and Schmale 2011). The results of this computation are shown in Figure 17. Figure 17 has the same layout as Figures 13 and 14. A most notable difference between Figures 17 and 13 is the red spots near LIDAR. They disappear in Figure 17 because the vertical shear near ground has been excluded as the FTLE computation only considered horizontal separations. As seen, these figures bear much better correspondence with the 2D analyses, especially for RAMS and FLOWSTAR data (when the vertical velocity was smaller as compared to WRF). Correspondence in WRF between Figures 14 and 17 is still better than that between Figures 13 and fig:conecomp2.

We show in Figure 18 comparison among LCS from LOS velocities. The panels are, from left to right, RAMS, FLOWSTAR, WRF, and LIDAR scan. The plots in

the top row show forward time LCS and those in the bottom row show backward time LCS. For the model data, we first compute the LOS velocity on the LIDAR scanning cone. Based on this data, we process the 2D variational retrieval outlined in section 2. The retrieved velocity is then processed with the FDFTLE algorithm. This fully emulates the cycle of realistic LIDAR retrieval that is operational at HKIA. We first contrast the LOS based 2D LCS to the previous 3D and 2D LCS results. It is quite clear that all plots compare well with the features see in Figure 13 in the respective model data sets. There is further degradation from the 3D results, but the structures near LIDAR seem to be robust even undergoing the many approximations. Those structures between the -1 NM windshear location and LIDAR seem to preserve their shape especially well.

As a comparison to real data, we also show, in Figure 18 (d) and (h), LCS extracted from LIDAR observed LOS. The WRF data seem to have the best match with LIDAR generated LCS, although FLOWSTAR shows better correspondence in the orientation of the structures. In addition, the RAMS data also has good correspondence with LIDAR around the LIDAR. It is especially interesting to note that the mismatch structure aligned with the landing trajectory in Figure 13 (c) is also present in Figure 18 (c) and (d), further ascertaining the match between the WRF data set and the benchmark.

Using cross correlation among two-dimensional data sets (Gonzalez and Woods 2007; BozorgMagham, Ross, and I. 2013) in Figure 18, we confirm that the max correlation between LIDAR and WRF is 35% for forward FTLE and 33% for backward FTLE, between LIDAR and FLOWSTAR is 13% for forward FTLE and 32% for backward FTLE and between LIDAR and RAMS is 30% for forward FTLE and 20% for backward FTLE. This is generally consistent with the visual observations. Note

that we only allow the shift in both longitudinal and latitudinal directions to be ± 1 km to ensure that the correlation is meaningfully through nearby structures.

3.4.3 Comparisons with Onboard Measurements

In (Kafiabad, Chan, and Haller 2013), it is shown that the projected FTLE gradient, defined as

$$\sigma^P = |\nabla\sigma \cdot \boldsymbol{e}|, \tag{3.4}$$

where $\boldsymbol{e}$ is the direction along the glide path, yields better Receiver Operating Characteristic (ROC) graphs as compared to the FTLE value or norm of FTLE. As such, in this subsection we contrast FTLE value σ and the projected FTLE gradient σ^P for results from the various schemes at hand. In order to provide a ROC graph, large numbers of cases need to be analyzed. Here we only focus on one reported windshear case and contrast only the backward time measures, which are more relevant to jolts experienced by the aircraft.

We show our detailed comparison in Figure 19. The left three columns of Figure 19 are from three-dimensional simulation data (RAMS, FLOWSTAR, AND WRF, resp.) and the last column is from LIDAR scans. The x-axis is the distance from the runway threshold along the glide path, and the y-axis is the relevant Lagrangian measures. The top panels are from the FTLE values σ and the bottom panels are from the projected FTLE gradients σ^P. The gradients are also scaled by 10 NM to place the curves in similar scale. In each panel, the black curve is the vertical acceleration measured onboard. As seen, there are several spikes from -1 NM towards the runway threshold, where a very large spike appears. Windshear was reported at -1 NM. In

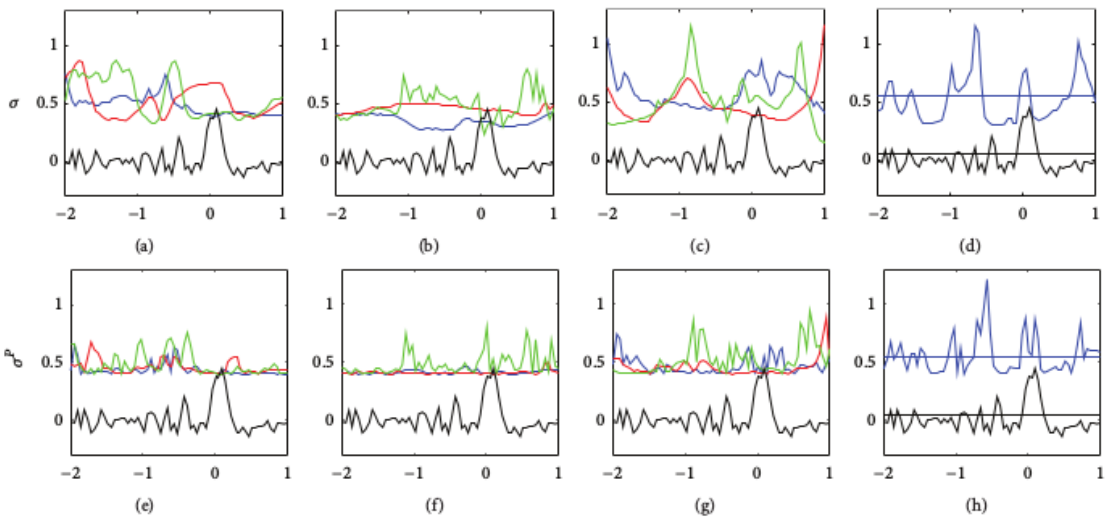

Figure 19. Lagrangian measures compared to vertical acceleration measured onboard an aircraft. From left to right, the data is from RAMS, FLOWSTAR, WRF, and LIDAR scans. Only backward time measures are computed since they are relevant to jolts experienced onboard. The top panels are the FTLE values interpolated along the glide path, and the bottom panels are the projected FTLE gradient. A strong windshear is reported at -1 NM from the runway threshold (0 in the x-axis). The black curves in each panel are vertical acceleration measured from the aircraft. For the left three columns, the blue, red, and greed curves correspond to data interpolated from the reduced FTLE, 2D FTLE, and LOS based FTLE. In the right column (from actual LIDAR data), the blue curves are LOS based FTLE.

the left three columns, the blue, red, and green curves correspond to 3D (reduced FTLE in Figure 26), 2D, and LOS based FTLE interpolations. In the right column, since only 2D information is available, the blue curves are LOS based FTLE. These curves are shifted up by 0.4 for clarity of the figure.

The RAMS data in Figure 19 (a) and (e) show consistency with the major spikes. In particular, the 3D (blue) and 2D (red) FTLE from RAMS do have (relatively small) spike at -1 NM. Although a spike is not found precisely at -1 NM for the LOS based FTLE (green) in Figure 19 (a), a major peak is found nearby. As such, in the projected gradient field σ^P (Figure 19 (e)), a spike is found at -1 NM for the green

curve. In fact, in this plot, several other spikes are identified leading up to the spike at the runway threshold, with good correspondence in the precise locations of spikes from all three schemes of FTLE extraction. As for the major peak at the runway threshold, minor spikes can be found to the right of this peak in all schemes.

The 3D (blue) and 2D (red) FLOWSTAR data in Figure 19 (b) and (f) show little correspondence with the actual vertical acceleration experienced onboard. Again, this may be due to the fact that FLOWSTAR is more driven by the topography instead of the physics, and so a precise match cannot be found. However, we still do identify spikes in the LOS based σ and σ^P fields (green) that can be related to major spikes at -1 NM and at the runway threshold.

The WRF data in Figure 19 (c) and (g) picks up the spikes at -1 NM most significantly. Both the 2D (red) and LOS based (green) σ and σ^P show spikes at -1 NM, yet the 3D (blue) and LOS based (green) σ and σ^P show spikes at the runway threshold. A minor peak can also be identified in the 3D (blue) curves around -1 NM. This minor structure can be identified near the diamond in Figure 26 (f).

Most relevant to operations, the LIDAR scan shows strong spiking behavior at -1 NM and the runway threshold, indicating the good correspondence between the two measurement data. Comparing the LOS based FTLE, it can be seen that WRF data most closely mimic those from the LIDAR in Figure 19.

To quantify the correlation among the many graphs shown, we focus on the relation between the vertical acceleration profile and the LIDAR based FTLE (the rightmost column in Figure 19), as well as the relation between the LOS based FTLE from the three models (green curves in the left three columns of Figure 19) and the LIDAR based FTLE. The first comparison shows the effectiveness of the LIDAR based algorithm for real-time forecasting, whereas the second shows the performance of the models to

observations. Note that since FTLE and vertical acceleration are two entirely different measures, one would not expect that the shape matches closely. As such, we first use the conditional probability developed in (Tang, Chan, and Haller 2011b) to quantify the effectiveness of LIDAR based FTLE in detecting actual jolts.

Consider vertical acceleration greater than $0.05g$, where g is the gravitational acceleration, being strong jolts (spikes above the black horizontal line), we look for strong FTLE ridge (> 0.15 s^{-1}) in the vicinity (150 m) of the jolts (spikes above the blue horizontal line). The justification of these parameters is given in (Tang, Chan, and Haller 2011b). For the landing approach analyzed here, we find that 1 out of 7 jolt spikes is left unaccounted for, and 1 out of 6 FTLE ridges does not correspond to a nearby jolt. Using FTLE gradient, again, 1 out of 7 jolt spikes is left unaccounted for, and 3 out of 10 FTLE ridges do not correspond to a nearby jolt. In fact, using cross correlation, the max correlation between the FTLE field and the vertical acceleration profile is 55%, whereas that between the FTLE gradient and the vertical acceleration is 57%.

We use cross correlation to measure the correlation of the model data with LIDAR. At the respective maxima, in terms of the FTLE field, the LIDAR is 24% correlated to RAMS, 39% correlated to FLOWSTAR, and 58% correlated to WRF. In terms of the gradient, the LIDAR is 23% correlated to RAMS, 19% correlated to FLOWSTAR, and 33% correlated with WRF. The high correlation between the LOS based WRF data and LIDAR as well as the high correlation in their headwind profile led us to believe that WRF best captures the details of the flow variation close to observations.

3.5 Conclusions

The recently developed Lagrangian based turbulent structure extraction methods near the Hong Kong International Airport bring forward great promise in accurate detection of airflow hazards and prompt issuance of windshear warnings. The original method is based on two-dimensional scans from light detection and ranging equipment, going through a variational retrieval step. This huge loss of information necessitates the need to validate the 2D methodology against 3D data sets to (i) verify that the 2D interpretations of 3D structure are correct; (ii) test if the Lagrangian extraction methodology does capture major flow hazards; (iii) confirm that the LIDAR based data (which has already gone through averaging in the measurements and modeling in the variation retrieval step) is useful in representing the real atmosphere; and (iv) compare with actual flight data and verify the applicability of the entire Lagrangian based methodology.

In this study, we have conducted thorough comparisons to address the aforementioned needs. Our first comparison between full 3D LCS and 2D LCS from velocity projections onto the LIDAR scanning cone indicates that there could be mismatches when the stretching rate is evaluated from the vertical separations. A reduced FTLE based on just the horizontal separation of trajectories shows good correspondence between the 3D and 2D data, at least within 2 nautical miles from the LIDAR. This confirms that our interpretation of 3D structures from 2D signatures is valid, at least close to the LIDAR where the elevation is low.

Secondly, we emulate the LCS generation process as if the 3D velocity data is the atmospheric truth. Line-of-sight (LOS) velocity on the LIDAR scanning cone is interpolated and used to generate 2D velocity via a variational retrieval technique

developed at HKIA. Our results show that, inside a 2-nautical-mile radius from LIDAR, the LOS based LCS is again comparable to the reduced FTLE. This confirms the applicability using LIDAR based LCS to interpret true atmospheric structures.

Thirdly, in order to test if the model data are truthful to real atmospheric conditions, we compare the model based LIDAR emulated LCS to true LIDAR based LCS. It is found that each model captures some feature of the true LIDAR based LCS, yet those results produced from our WRF simulation match the best with LIDAR results. The close match between WRF and truth, as well as the close relation between 3D LCS and LOS based LCS from the WRF data set, suggest that the LIDAR based LCS can be used to infer structures in the real atmosphere.

Finally, we compare the LCS results and actual jolts experienced onboard an aircraft which attempted to land at the time of our analyses. It is found that our Lagrangian indicators (most pronouncedly from WRF and LIDAR) capture well the large acceleration experienced by the aircraft. This helps establish the point of using Lagrangian measures as operational tools in the detection of safety-threatening and comfort-compromising jolts during landings.

The close match between WRF and LIDAR data brings us hope to further refine our Lagrangian methodology by improving the forecasting model data, which is undertaken in the next chapter.

Chapter 4

DATA ASSIMILATION OF LIDAR IN WRF AT THE HONG KONG INTERNATIONAL AIRPORT, WITH APPLICATIONS TO LAGRANGIAN COHERENT STRUCTURE ANALYSIS

4.1 Introduction

As mentioned in the introduction to Chapter 3, Lagrangian measures are a very promising tool in improving windshear detection for landing aircraft at the Hong Kong International Airport (HKIA). In fact, Lagrangian analysis using LIDAR data at HKIA was first carried out in (Tang, Chan, and Haller 2011a, 2011b), and further analyzed in (Kafiabad, Chan, and Haller 2013). We now use the three-dimensional variational (3DVAR) data assimilation suite in the Weather Research and Forecast (WRF) numerical weather model to incorporate the LIDAR line of sight velocity readings into the WRF forecast. After a discussion on this process, we extract LCS and compare to flight data.

4.2 WRF Model Settings

WRF was run using 6 nested domains with two-way feedback. The innermost nest had a grid spacing of 150 m while the largest nest had a grid spacing of 36.45 km, corresponding to a parent-child grid ratio of 3. The innermost nest was centered at 22.313 N, 113.92 E, the coordinates of the northern LIDAR at HKIA, and had 157 grid points in both the x and y directions, and so covered an area 23.4 km $\times$ 23.4 km.

The remaining nests each had 133 grid points in the x and y directions. 85 vertical levels were used in an attempt to match the high horizontal resolution, with a uniform spacing of about 15 m for the first 600 m of height, and then increasing in a non-linear profile typical in WRF. This uniform layer was chosen to try and fully resolve the flow within the LIDAR range.

The Thomson graupel scheme was used for microphysics, and the RRTMG scheme used for both shortwave and longwave radiation (ra_lw_physics = 4, ra_sw_physics = 4). The revised MM5 Monin-Obukohov surface layer scheme (sf_sfclay_physics = 1) was used with the unified Noah land-surface model for surface physics (sf_surface_physics = 2), together with the Yonsei University scheme for the boundary layer parameterization (bl_pbl _physics = 1). The exception to this was the sixth nest (the inner most nest) where no boundary layer parameterization was used. The Tiedke scheme was used for cumulus parameterization (cu_physics = 16), called every 5 minutes, with the exception again being the sixth nest, which had no cumulus parameterization. The horizontal Smagorinsky first order closure was used for the eddy coefficient (km_opt = 4), together full diffusion (diff_opt = 2). In the sixth nest, since the boundary layer parameterization was turned off, the 1.5 order TKE closure was chosen for the eddy coefficient (km_opt = 2). The initial conditions and boundary conditions for the outermost nest were driven by the NCEP FNL Operational Global Analysis data.

Since turbulence along the landing corridor is largely terrain driven, we further considered the model topography. The highest resolution topography data included by default in WRF has a resolution of 30 arcseconds, which is roughly about 900 m (depending on latitude). Since the finest nest has a grid spacing of 150 m, this proved to be too poorly resolved for our purposes; The Advanced Spaceborne Thermal

Emission and Reflection Radiometer Global Digital Elevation Model (ASTER DEM) data was therefore used, which provides terrain elevation every 1 arcsecond, roughly about every 30 m. For a comparison, the highest peak on Lantau Island is about 934 m. Using the default 30 arcsecond topography results in an in-model peak of 655 m, whereas using the ASTER 1 arcsecond data results in an in-model peak of 860 m, which is much closer to the true value (generally speaking steep terrain can cause numerical issues in WRF, and so the topography data is smoothed before used; we used a single pass of this smoother. There is a trade-off between losing terrain features via the smoothing and WRF requiring an unfeasible small time step due to the steep terrain). If an inner nest spacing of 200 m were to be used, the height of the in-model peak would have been 846 m. The extra computational cost of the smaller grid spacing of 150 m and the steeper terrain topography was worthwhile, since correcting the model using the LIDAR, but not incorporating enough of the driving causes of the turbulence, would have most likely only resulted in transitory changes where the forecast updates cannot be sustained between cycles.

4.3 Assimilation of LIDAR Scans into WRF

Assimilation of radar observations in the WRF model is implemented in the WRF data assimilation system (WRFDA) using both three-dimensional (3DVAR) and four-dimensional (4DVAR) variational methods (D.M. Barker et al. 2004; Huang et al. 2009; D. Barker et al. 2012; Xiao et al. 2005; Wang et al. 2013; Choi, Lim, and Lee 2013).

There are two long range LIDAR stations at HKIA, shown in Figure 20. Further information concerning these systems and their deployment at HKIA can be found in

(Shun and Lau 2002; Shun and Chan 2008; Chan and Lee 2012). We had data from both the northern and southern LIDAR stations; the northern LIDAR scans at an elevation of both 1.4° and 3°, whereas the southern LIDAR scans at 3°. We found that the northern LIDAR generally provided superior results, possibly due to the southern LIDAR being in closer proximity to Lantau Island. We used the observations from both the scanning angles from the norther LIDAR, since a typical airplane landing trajectory lies between the two scans. The LIDAR data is provided from HKIA on a grid with 100 m spacing, which was interpolated onto a grid with horizontal grid points matching that of WRF. WRFDA requires that radar observations are input with latitude/longitude coordinates to 3 decimal places; with this high resolution LIDAR data distinct data points sometimes had identical rounded coordinates, so this interpolation resolved such conflicts. This also resulted in the location of the LIDAR station to be rounded, and so they are not exact. Such details are insignificant at the length scales of typical radar assimilation, but may be worth noting in this context. Any anomalous data needed to be masked out before input into WRFDA. Depending on weather conditions, this ranged from relatively few data points to a majority of the LIDAR readings; the performance under these range of conditions will be discussed below in our case studies. Typically, though, around 5100 LIDAR observations were assimilated at each step. New LIDAR data is available for each elevation angle about every 140-150 s. Note that each complete LIDAR scan is regarded to be an observation at a single point in time.

As mentioned above, the higher resolution topography data resulted in a longer computational time, one of the consequences of which was that we could only feasibly use 3D-VAR and not 4D-VAR. 4D-VAR requires integrating the tangent linear and adjoint models forward and backward in time, respectively, and we found that we

needed to take an extremely small time step to avoid blow up. So small, in fact, that integrating forward the necessary time to incorporate even a single additional LIDAR scan took an untenable amount of time. Integrating 4D-VAR any shorter amount of time would be functionally the same as 3D-VAR.

A key component of variational data assimilation are the background and observation error statistics. WRFDA allows for the creation of background error statistics particular to the domain under consideration or the use of a default statistics file. We chose to use the default statistics information (i.e. we used the NCEP background error model). We also chose to give a lot of trust of the LIDAR data, and so tailored the observation error statistics to this end. More careful consideration of each of these points would be required for any operational implementation, but our current aim is rather to extend the analysis from Chapter 3 by matching as close as possible the WRF model to the LIDAR observations. When the generic background error statistics are used certain tuning parameters need to be set, corresponding to the length scales of different control variables. We found, through simple trial and error, a combination of that worked very well, although it is certainly possible the combination we chose is not the most optimal.

There is also the question of when to stop the iterative process that minimizes the cost function. Typically in WRFDA the stopping condition is set to be a factor that the norm of the gradient of the cost function is reduced by, for instance, stop when the norm of the gradient is, say, 10% of its original value. We instead set the number of inner loop iterations to run, finding in our cases that 1-5 iterations provided a good balance of matching the observations while at the same time keeping the flow physically realistic. Of course, with the complex interactions between the observation error statistics, the background error statistics, and the control variable

parameter settings, this number is likely very specific to our specific case. Six outer loop iterations were performed. WRFDA also allows for the automatic removal of any observations that cause too large an innovation, but we disabled this feature. We found this necessary for any improvements in regions where the WRF model performed particularly poorly as compared to the LIDAR observations, since in these regions larger innovations are necessarily required. Furthermore, any "clutter" in the LIDAR data was removed prior to running WRFDA, and so erroneous LIDAR data was not driving the large innovations.

To be very clear, most of our choices here were empirical and heuristic in nature, and would need to be reconsidered and/or refined before operational implementation. But, again, our interests here are in improving the Lagrangian analyses found in (Tang, Chan, and Haller 2011a, 2011b; Kafiabad, Chan, and Haller 2013) and Chapter 3 rather than, at this point in time, trying to setup an operational WRF forecast at HKIA.

The cycling scheme we used was the following: suppose that at time t_0 we have LIDAR data. We take the WRF model output from our innermost nest at this time as input to WRFDA. We perform the data assimilation and take the output to be the new WRF input file for that nest. We then run WRF until time t_1, the next time there is available LIDAR data, at which point WRF is stopped and assimilation performed again. The output is again copied to be the new input to WRF and the model restarted, the procedure cycling in this manner. Since the LIDAR data is localized near HKIA, we only perform data assimilation on the innermost nest; there is little point in trying to assimilation LIDAR scans, which have a maximum possible range at HKIA of about 10 km, into, say, the outermost nest whose grid spacing is

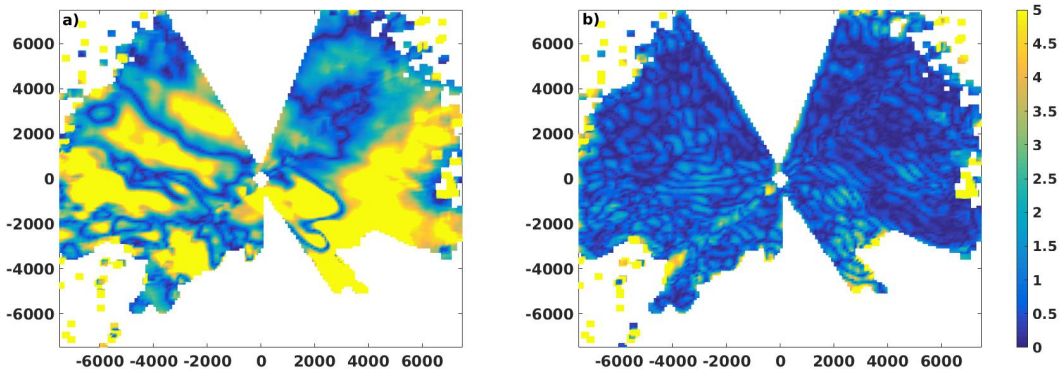

Figure 20. The magnitude of the difference in the radial velocity between WRF and 3° LIDAR on 2009-02-21 at 07:50:10. (a) No data assimilation. (b) Data Assimilation

36.45 km. Nest feedback is the only route by which the LIDAR information propagates to the other nests.

4.4 Case Studies

Two different case studies, on 2008-04-19 and 2009-02-21, were analyzed to test the data assimilation procedure described above. The days, and times chosen on these days, where chosen to correspond to available flight data; see (Tang, Chan, and Haller 2011a, 2011b), and Chapter 3, for more information.

4.4.1 2009-02-21

A high pressure ridge over the southeast coast of China caused strong easterly winds at HKIA, with rain affecting the range of the LIDAR throughout the course of the day. WRF was spun up starting at 06:00:00 and run until 07:50:10, when the data assimilation was started. This first cycle used LIDAR observations from the 3° scan.

Figure 20 shows the magnitude of the difference between the radial velocity, given by WRF, and the LIDAR observations; panel (a) corresponds to no data assimilation, panel (b) after data assimilation. As can be seen, the data assimilation results match very closely with the LIDAR scans. Such a close match is only beneficial, however, as long as the resulting flow is still physically realistic and useful. Figure 21 shows a before and after comparison of the horizontal (the vector fields) velocity together with a color plot of the vertical velocity. As before, panel (a) is the WRF model with no data assimilation, panel (b) after data assimilation. There are some immediate things to note in this comparison. First, the direction of the flow has changed subtly, with a more northward tendency than the base WRF model. This is most clearly seen in the w-component color plot, where the streaks downwind from Lantau Island have changed direction. Second, the data assimilation has resulted in a region of very strong vertical motion to the east of the landmass north of Lantau Island. There now appears to be a backflow as the air hits the landmass, rather than being carried directly over in the base WRF case. This may be a result of the slight change of the flow direction after data assimilation. It was found that such a change resulted in virtually every parameter change in WRFDA that produced a better radial velocity match with the LIDAR. With this in mind, and since this region doesn't significantly affect the forward or backward time LCS near HKIA, we decided that such a change was acceptable. Third, the flow in the region to the west of HKIA has been changed fairly significantly, in terms of structure, indicating that along the landing corridor the WRF model may now yield LCS that match even better with those produced by LIDAR alone.

The next LIDAR data was available at 07:51:10, for the 1.4° scan. This presented an interesting check for the consistency in the flow changes made by WRFDA. One

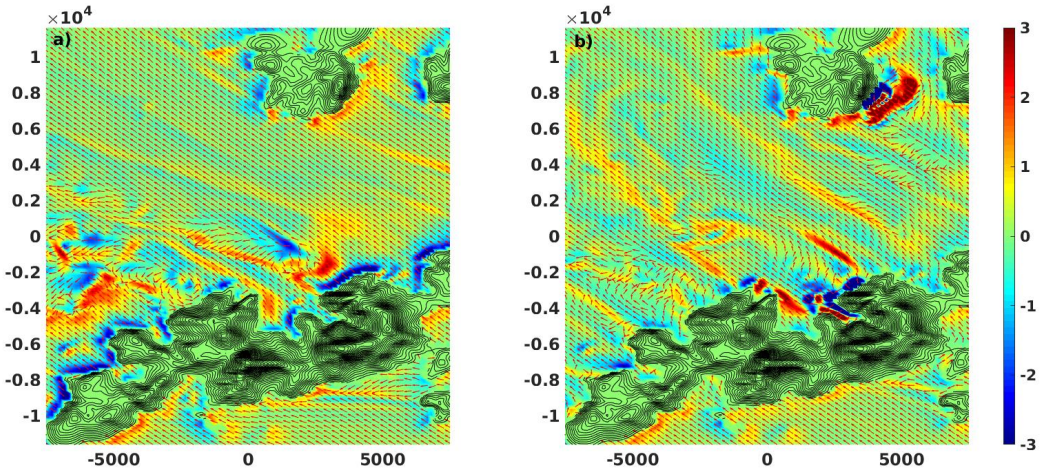

Figure 21. The horizontal velocity field at $z = 100$ m, together with a color plot of the w-component of velocity. (a) No data assimilation. (b) Data assimilation

would hope that the changes made to better match the LIDAR observations from the 3° scan at 07:50:10 would provide a forecast that would, as a baseline, better match the LIDAR observations for the 1.4° at 07:51:10. In other words, can both LIDAR scans be used to improve the WRF forecast, or will the changes made at one cycling step be undone at the next? If so, then we would need to only use one angle scan rather than both. The comparison is made in Figure 22, which shows the magnitude of the difference in the radial velocity from WRF and from the 1.4° LIDAR at 07:51:10. In panel (a), no data assimilation was performed. In panel (b), data assimilation from the 3° scan at 07:50:10 was performed, then WRF cycled until 07:51:10 - but no data assimilation was performed at 07:51:10. Finally, in panel (c), data assimilation from the 3° scan at 07:50:10 was performed, then WRF cycled and data assimilation performed at 07:51:10 using the 1.4° LIDAR observations. As clearly seen in panel (b), the changes made at 07:50:10 resulted in a more accurate forecast at 07:51:10, in other words, the changes made in WRF are consistent between the two scanning angles for the northern LIDAR. As such, it appears that it would be beneficial to

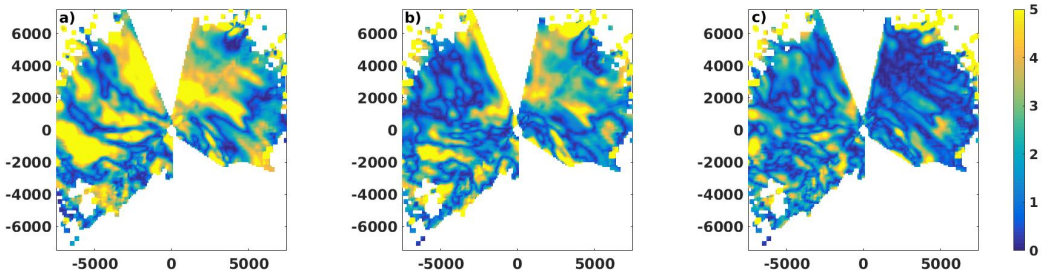

Figure 22. The magnitude of the difference in the radial velocity between WRF and the 1.4° LIDAR on 2009-02-21 at 07:51:10. (a) No data assimilation. (b) Data assimilation performed at 07:50:10 using the 3° LIDAR observations. (c) Data assimilation performed at 07:50:10 using the 3° LIDAR observations and data assimilation performed at 07:51:10 using the 1.4° LIDAR observations.

use the scans at both angles in any data assimilation implementation. We also note in Figure 22 panel (c) that while the data assimilation at 07:51:10 did reduced the error, the improvement was not as good as it was at 07:50:10, as seen in Figure 20 (b). There are two plausible explanations for this, the first being that since the LIDAR scan at 1.4° is closer to the ground there may be issues with the WRF generated flow near-ground. For instance, the lowest model level of WRF near HKIA turned out to be around 30 m. Secondly, we may be able to further tune the parameters in WRFDA to get a closer match, but in terms of operational simplicity it may be better to have a uniform choice of parameters for each scan.

4.4.2 2008-04-19

A tropical cyclone made landfall and moved inland, causing strong southerly winds. In our times of interest there was no rain, and so the LIDAR coverage is very good. WRF was spun up starting at 12:00:00, and run until the assimilation cycling started at 13:40:10.

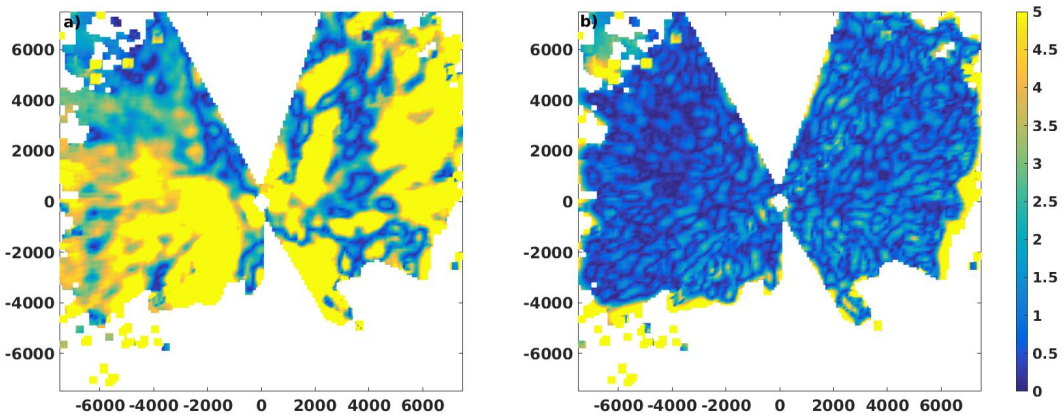

Figure 23. The magnitude of the difference in the radial velocity between WRF and 3° LIDAR on 2008-04-19 at 13:40:10. (a) No data assimilation. (b) Data Assimilation

In Figure 23 we compare the magnitude of the difference in the radial velocity between WRF and LIDAR, similar to Figure 20. We again see that our data assimilation scheme results in a radial velocity that closely matches the LIDAR observations. In Figure 24 shows a before and after comparison of the horizontal (the vector fields) velocity together with a color plot of the vertical velocity. As before, panel (a) is the WRF model with no data assimilation, panel (b) after data assimilation. This figure is similar to Figure 21 above. We first note that there are very minimal changes made to the vertical velocity, in contrast with with what we found for the 2009-02-21 case. Comparison of the flow direction between the two panels shows that there are changes made in certain regions, but the bulk flow generally has the same characteristics pre and post data assimilation.

To make a similar comparison as in the 2009-02-21 case, we next run WRF until 13:41:30, when a 1.4° scan is available. We make a similar comparison for consistency in Figure 25. Panel (a) shows the magnitude of the difference in radial velocity between WRF and LIDAR with no data assimilation, panel (b) shows the difference between

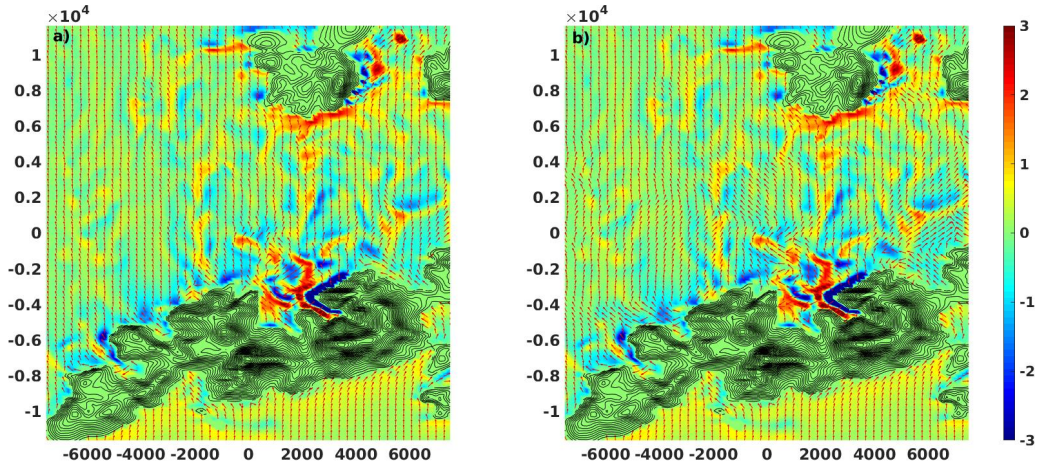

Figure 24. The magnitude of the difference in the radial velocity between WRF and 3° LIDAR on 2008-04-19 at 13:40:10. (a) No data assimilation. (b) Data Assimilation

WRF and LIDAR at 13:41:30, before performing assimilation with the LIDAR data available at that time, and panel (c) shows the difference after data assimilation of the 1.4° LIDAR scan at 13:41:30. As can be seen, the changes made in WRF are again consistent between the LIDAR scanning angles. Figure 26 shows the comparison for one more cycle, incorporating the next 3° at 13:42:40. The panel layout is the same. Again, we note the consistency between the different scanning angles, and therefore use such a cycling scheme in the comparisons done below.

4.5 Comparisons of LCS and to Onboard Flight Data

We now use our results to extract LCS, and compare to onboard flight data. In other words, how does the LIDAR data assimilation into WRF affect the correspondence between vertical accelerations and LCS. In Chapter 3 there were three comparisons made between the LIDAR LCS and LCS generated from WRF data - computing

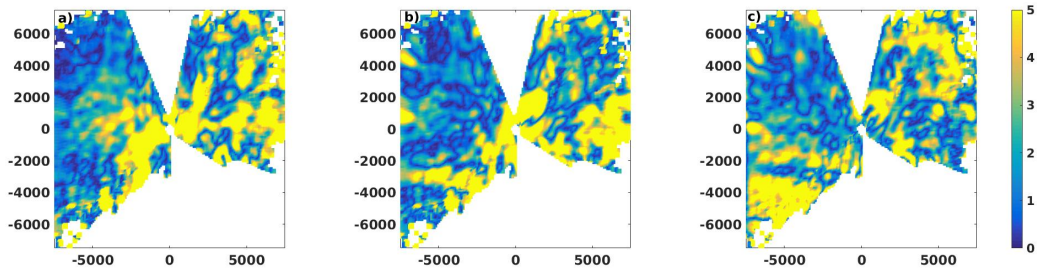

Figure 25. The magnitude of the difference in the radial velocity between WRF and the 1.4° LIDAR on 2008-04-19 at 13:41:30. (a) No data assimilation. (b) Data assimilation performed at 13:40:10 using the 3° LIDAR observations. (c) Data assimilation performed at 13:40:10 using the 3° LIDAR observations and data assimilation performed at 13:41:30 using the 1.4° LIDAR observations.

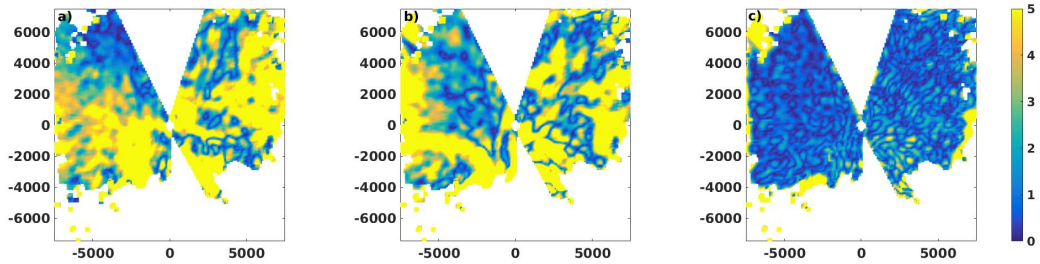

Figure 26. The magnitude of the difference in the radial velocity between WRF and the 1.4° LIDAR on 2008-04-19 at 13:42:40. (a) No data assimilation. (b) Data assimilation performed at 13:41:30 using the 1.4° LIDAR observations. (c) Data assimilation performed at 13:42:40 using the 3° LIDAR observations and data assimilation performed at 13:41:30 using the 1.4° LIDAR observations.

the full three-dimensional LCS, and then projecting onto the LIDAR scanning cone, projecting the three-dimensional wind velocity onto the LIDAR scanning cone, and then extracting the resulting two-dimensional LCS, and finally, computing the line of sight velocity from WRF onto the LIDAR scanning cone, running the two-dimensional wind retrieval algorithm, and then extracting LCS. We chose the second of these cases; if we were to run the wind retrieval algorithm after computing the line of sight velocity, we would not expect any difference from the LIDAR generated LCS, since as shown in the above section after data assimilation the line of sight velocity

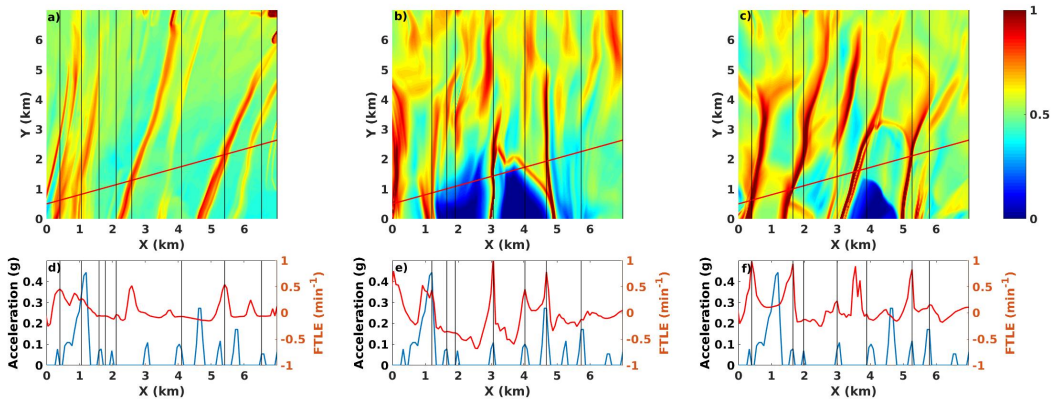

Figure 27. Airplane landing data in comparison to LCS for a missed approach at 14:03:40 on 2008-04-19. (a) Approach path superimposed on backward-time LCS based on the 3° LIDAR scan. (b) Approach path superimposed on backward-time LCS computed from WRF . (c) Approach path superimposed on backward-time LCS computed from WRF, using data assimilation. (d) Comparison between positive vertical acceleration and backward-time FTLE. Vertical acceleration measured onboard the aircraft is shown in blue, with values less than 0.05g removed. The red line is the backward-time FTLE computed from the 3° LIDAR scan, interpolated along the flight path. (e) Comparison between positive vertical acceleration and backward-time FTLE, computed in WRF. (f) Comparison between positive vertical acceleration and backward-time FTLE, computed in WRF, using data assimilation. The black vertical lines highlight locations where LCS are correlated with vertical acceleration. The origin corresponds to the northern LIDAR.

in WRF matches very closely with the LIDAR. We choose not to project the full three-dimensional LCS since we are interested in flow structures significant enough to register on the LIDAR. The integration time is 5 minutes and the finite domain extension from (Tang, Chan, and Haller 2010) was also used. Note that as argued in (Tang, Chan, and Haller 2011a, 2011b), ridges in the forward-time FTLE should generally correspond to vertical downdrafts, hence a negative vertical acceleration measured onboard the aircraft, whereas a backward-time FTLE ridge should generally correspond to a vertical updraft, ie a positive vertical acceleration measured onboard.

4.5.1 2008-04-19

The first flight we analyze is from an aborted landing at about 14:03:40. We use the 3° scan, since we have data from this scan at a time very close to the landing attempt. In Figure 27 we compare the airplane landing data with backward-time LCS. Panel (a) shows the LCS generated from LIDAR, panel (b) LCS generated from WRF, and panel (c) LCS generated from WRF, after data assimilation. In each panel, the red line indicated the landing path of the aircraft. In panels (d) through (f) we compare the corresponding FTLE with vertical acceleration measured onboard the aircraft. Panel (d) corresponds to the LIDAR FTLE, panel (e) the WRF FTLE, and panel (f) the WRF, data assimilation FTLE. We remove all vertical acceleration values less than 0.05g, as justified in (Tang, Chan, and Haller 2011b). The black vertical lines highlight locations where the LCS and vertical acceleration are correlated, with a line drawn if the corresponding peaks are within 150 m; this distance is again explained in (Tang, Chan, and Haller 2011b).

Immediately, we first note that both WRF cases yield LCS more complex than the LIDAR, as explained in Chapter 3, and as expected. Second, in comparing the LCS in the top three panels, we see that the base WRF model, in panel (b), shows structures oriented north-south, whereas the LIDAR, in panel (a), yields structures oriented more to the northeast. Something similar was seen in Chapter 3 in Figure 18, where there was also a misalignment in the LCS as compared to WRF and LIDAR. As panel (c) shows, the data assimilation is successful in aligning the flow structures to match the LIDAR LCS. This is critical, since if not, any correlation between WRF generated LCS and vertical accelerations would prove to be mostly coincidental if the flow structures are consistently misaligned along the landing paths. In other words,

data with many peaks will often show correlations, the question for us is whether the vertical accelerations measured onboard correlate to the actual LCS that cause the accelerations in WRF. For instance, in Figure 27, panel (b), at roughly (5,2), we see that a strong FTLE ridge corresponds very closely to an acceleration peak. But, comparing to the LIDAR LCS in panel (a), we see that the most likely corresponding structure should intersect the flight path at roughly (5.5,2), and so that particular LCS most likely didn't cause the specific vertical acceleration that WRF would predict. Panel (c) shows a correspondence that matches the LIDAR very closely, comparing the same FTLE ridge to its matching acceleration peak.

Further analyzing the LCS shown in panels (a) through (c) shows the effects of the data assimilation. The vertical FTLE ridge in panel (b) that starts at the point (3,0) has a break as we move vertically, whereas the same ridge in panel (c) has no such break. Comparing to the LIDAR LCS, there is no such break. On the right hand side of panel (a) we see a ridge (intersecting the x-axis at the point (5.75,0)) missing in panel (b), which is recovered by the data assimilation in panel (c). The ridge in panel (a) that starts at the point (2,0) most likely corresponds to the ridge starting at roughly (2.75,3.25) in panel (b) and the point (3,2.5) in panel (c). We note that this ridge is broken in both panels (b) and (c), an example of the data assimilation either not being able to correct the fundamental error in WRF, or the LIDAR not being able to capture the true flow LCS. We also see that the two left most ridges in panel (c) are somewhat farther apart that they are according to the LIDAR information in panel (a). However, from a qualitative perspective, it is clear that the data assimilation results in a good correspondence between the WRF and LIDAR LCS.

Moving to panels (d) through (f), we see a good correlation between FTLE peaks and vertical accelerations, as found in (Tang, Chan, and Haller 2011b; Kafiabad,

Chan, and Haller 2013). The base WRF model in (e) is impressive at first glance, but remember the fundamental structure misalignment discussed above. As a first rough analysis, the LIDAR LCS was correlated to 7 significant vertical jolts as seen in panel (d), out of the roughly 11 experienced by the aircraft during the landing attempt. After data assimilation we see in panel (f) that the WRF LCS were also correlated with 7 jolts. Recall that we consider an FTLE ridge within 150 m of an aircraft jolt as a correlated to that jolt. It is worthwhile to compare in panels (d) and (f) the jolts are are identified with LCS and those that are not. The most significant jolt is experienced by the airplane at about $x = 1.25$ km, which the LIDAR LCS picks up, but the WRFDA LCS does not. However, we see in panels (a) and (c) that the FTLE ridge that causes the jolt is likely the same (the ridge starting at roughly (1,0) in panel (a) and roughly (1.25,0) in panel (c)), so this is more of a result of our 150 m criterion, coupled with the WRF mis-alignment bias, that a fundamental issue with the WRF LCS. Furthermore, while the exact value of the FTLE is not particularly relevant in terms of the size of the experienced jolt, the size of the FTLE peak is related to the robustness of the LCS in identifying jolts. As such, the strong ridge signature in panel (f) could be considered an improvement over the LIDAR FTLE in panel (a).

Along these lines, the jolt identified at $x = 4$ in panel (d) corresponds to a very weak FTLE signature, whereas in panel (f) the signature is more pronounced. This is similar to the jolt at around $x = 6.5$ in panel (d); the FTLE ridge is so weak, there is a valid question of whether that should be considered a true correlation. WRF misses this jolt entirely in panel (f), which suggests that it may indeed be spurious. We see in panel (f) that the jolts at $x = 3$ and $x = 5.75$ are correlated with FTLE ridges, whereas with LIDAR in panel (d) they are not. There is also an FTLE ridge

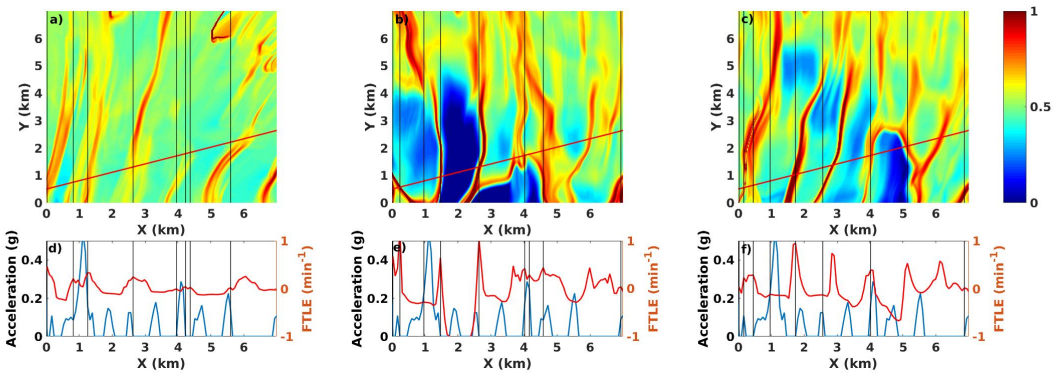

Figure 28. Airplane landing data in comparison to LCS for a missed approach at 13:46:40 on 2008-04-19. (a) Approach path superimposed on backward-time LCS based on the 1.4° LIDAR scan. (b) Approach path superimposed on backward-time LCS computed from WRF . (c) Approach path superimposed on backward-time LCS computed from WRF, using data assimilation. (d) Comparison between positive vertical acceleration and backward-time FTLE. Vertical acceleration measured onboard the aircraft is shown in blue, with values less than 0.05g removed. The red line is the backward-time FTLE computed from the 3° LIDAR scan, interpolated along the flight path. (e) Comparison between positive vertical acceleration and backward-time FTLE, computed in WRF. (f) Comparison between positive vertical acceleration and backward-time FTLE, computed in WRF, using data assimilation. The black vertical lines highlight locations where LCS are correlated with vertical acceleration. The origin corresponds to the northern LIDAR.

close to the jolt at $x = 4.75$ in panel (f) that falls just outside our 150 m threshold which is missed by the LIDAR in panel (d). After this more careful analysis, there is a very strong case that the WRFDA LCS provides an improvement in jolt detection relative to the LIDAR, at least for this particular case. Again, this is somewhat expected, since the data assimilation incorporates the LIDAR information into the full three-dimensional WRF flow, but it does illustrate the potential for the advanced prediction of jolts using WRF.

We now analyze another aborted landing in Figure 28, this time from 13:46:40. In this case, we used the 1.4° LIDAR to compare to, since a scan at that angle was closest to the landing attempt. This will also serve as a comparison between the

two scanning angles. The panels are similar as in Figure 27. We again see a similar improvement in the LCS after data assimilation. It is interesting to note, however, that a different choice of the background error scaling parameters was used in this case when the data assimilation was run. This is likely due to the fact that the 1.4° LIDAR readings are taken closer to the ground level as compared to the 3° scan. We again see that the base WRF model has a slight alignment error of the FTLE ridges, which the data assimilation corrects. Comparing the major structures, we see that 3 of those from WRF agree well with the LIDAR data. Comparing the LCS structure between the base WRF case in panel (b) and the WRF data assimilation case in panel (c), we notice that at a flight distance of greater than about 4 km from the LIDAR there is not very good agreement with any vertical jolts at all. This is likely due to the fact that the base WRF forecast yielded such misaligned structures that the corrections needed were more than the data assimilation could provide. We see a sort of horizontal connecting structure that forms a sort of arch shape (between the points (2,0) and (4.75,0) in panel (b) and between the points (3.75,0) and (5.25,0) in panel (c)). Similar structure was seen in Figure 27, a feature not seen on the LIDAR scans. We can see that the under the action of the data assimilation, the arch is moved out along the flow direction; presumably, in an ideal scenario it would "break", leaving the two unconnected streaks as seen in panel (a).

In panel (d) we see that the LIDAR extracted LCS has correspondence with 7 out of the 12 jolts, whereas after data assimilation the WRF generated LCS correlate well with 7 as well, as seen in panel (f). The major jolt at $x = 1$ appears to be better identified by LIDAR, whereas the significant jolt at $x = 4$ is better identified by WRF. While the improvement in the correspondence between the jolts and FTLE ridges in

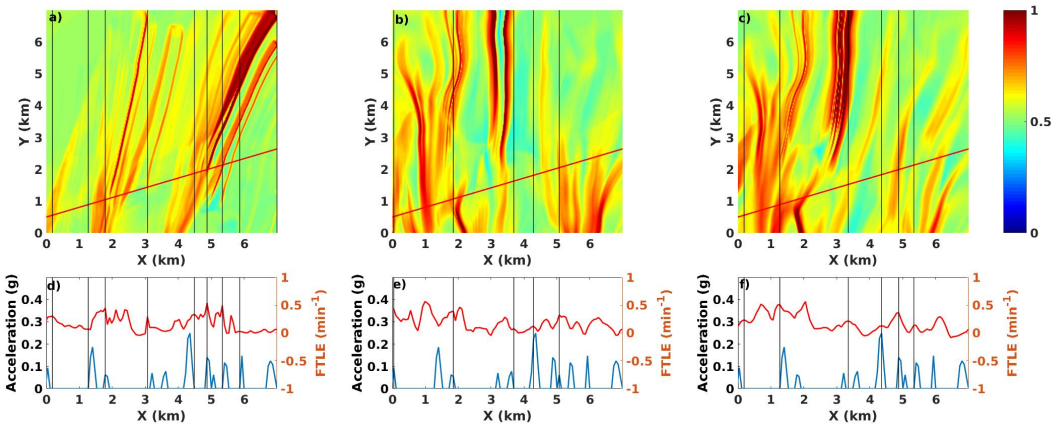

Figure 29. Airplane landing data in comparison to LCS for a missed approach at 14:03:40 on 2008-04-19. (a) Approach path superimposed on forward-time LCS based on the 3° LIDAR scan. (b) Approach path superimposed on forward-time LCS computed from WRF . (c) Approach path superimposed on forward-time LCS computed from WRF, using data assimilation. (d) Comparison between negative vertical acceleration and forward-time FTLE. Vertical acceleration measured onboard the aircraft is shown in blue, with values less than 0.05g removed. The red line is the forward-time FTLE computed from the 3° LIDAR scan, interpolated along the flight path. (e) Comparison between negative vertical acceleration and forward-time FTLE, computed in WRF. (f) Comparison between negative vertical acceleration and forward-time FTLE, computed in WRF, using data assimilation. The black vertical lines highlight locations where LCS are correlated with vertical acceleration. The origin corresponds to the northern LIDAR. Note that the vertical acceleration shown as been multiplied by -1.

WRF is not as pronounced in this case as the above case, we again see that using the WRF flow data we generally get a more robust correspondence.

We now considered the forward-time LCS, first for the aborted landing at 14:03:40. The layout in Figure 29 is as in Figures 27 and 28. Note that we have multiplied the vertical acceleration of the aircraft in panels (d) through (f) by -1 (this is done to make the comparison with the FTLE field easier visually - remember, ridges in the forward-time FTLE should correspond to downdrafts, hence minima in the vertical acceleration, and so multiplying by -1 results in a comparison of maxima to maxima). We note, as

in the backward-time cases discussed above, that the forward-time structures from WRF in panel (b) are misaligned, and that the data assimilation results in a correct to generally match the orientation of the LIDAR based LCS in panel (a). Comparing major structures, we see that the LIDAR LCS in panel (a) there appear to be two dominant "hairpin" structures rooted at around $(1.5, 0)$ and $(3.75, 0)$. There is not a particular good correspondence after data assimilation in the WRF LCS in panel (c), although we do see a hint of a match for the structure at $(3.75, 0)$. The structure intersecting the flight path at $(3, 1.5)$ in panel (a) does have good correspondence in panel (c). In panel (a) there is also a hint of a hairpin structure at $(6, 0)$, which we clearly see in panel (c).

We see in panel (d) that the LIDAR LCS correspond to 8 out of the 11 jolts experienced by the aircraft. In panel (f), we have a correspondence to 6 jolts. However, we again see some misses due to the 150 m threshold we have chosen. For instance, the jolt at about $x = 6$ is identified weakly by the LIDAR, whereas in panel (f) there is an FTLE ridge at about $x = 6.2$ that may have caused the jolt. Looking at the jolts between $x = 3$ and $x = 6$, we see that the WRFDA LCS in panel (f) we probably have a better qualitative correspondence with the FTLE peaks, having 5 fairly pronounced ridges in that range, whereas the LIDAR FTLE ridges in panel (d) are noisier, the LCS structures having been "spread" out in WRF in panel (c) as compared to panel (a). In fact, qualitatively speaking, the only mismatch in the WRF after data assimilation is the FTLE peak at about $x = 0.75$, otherwise there is a very promising general match in panel (f) between the FTLE curve and the aircraft jolts.

Figure 30 is as Figure 29, but for the landing at 13:46:40. Comparing major structures, we see that there are not many LCS structures seen in panel (a) before about $x = 1.75$ to compare to, although we do notice the structure in panel (a)

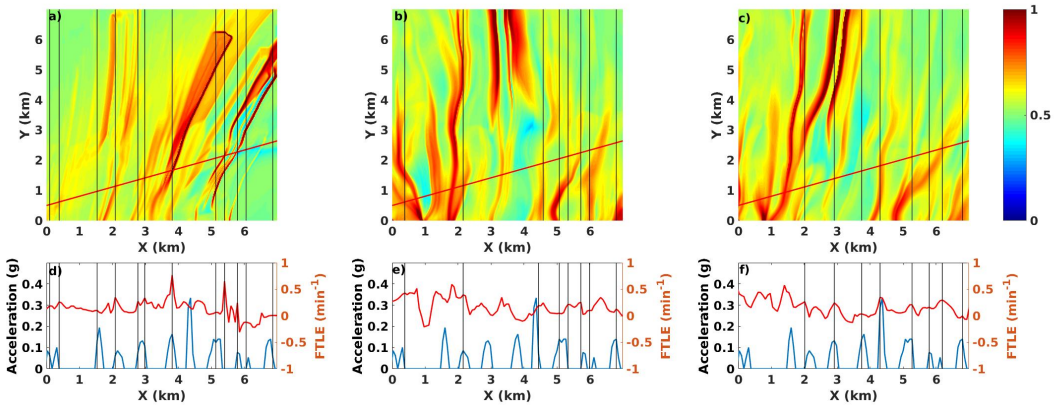

Figure 30. Airplane landing data in comparison to LCS for a missed approach at 13:46:40 on 2008-04-19. (a) Approach path superimposed on forward-time LCS based on the 1.4° LIDAR scan. (b) Approach path superimposed on forward-time LCS computed from WRF . (c) Approach path superimposed on forward-time LCS computed from WRF, using data assimilation. (d) Comparison between negative vertical acceleration and forward-time FTLE. Vertical acceleration measured onboard the aircraft is shown in blue, with values less than 0.05g removed. The red line is the forward-time FTLE computed from the 1.4° LIDAR scan, interpolated along the flight path. (e) Comparison between negative vertical acceleration and forward-time FTLE, computed in WRF. (f) Comparison between negative vertical acceleration and forward-time FTLE, computed in WRF, using data assimilation. The black vertical lines highlight locations where LCS are correlated with vertical acceleration. The origin corresponds to the northern LIDAR. Note that the vertical acceleration shown as been multiplied by -1.

starting at about $(1.5, 2.5)$ does appear in panel (c). We notice that in panel (a) we see a hairpin structure originating around (1.75,0), which is also seen in panels (b) and (c). The structures intersecting the flight path at around $x = 3$ and $x = 3.75$ in panel (a) appear also in panel (c). There is also a rough correspondence for the structure intersecting the flight path around $x = 5$ and $x = 5.5$, although the detail in the LIDAR panel is much finer than the WRF data assimilation LCS in panel (c). In panel (d) we find that the LIDAR LCS correspond to 11 of the 12 aircraft jolts, whereas the WRF data assimilation LCS correspond to 8 out of the 11, seen in panel (f).

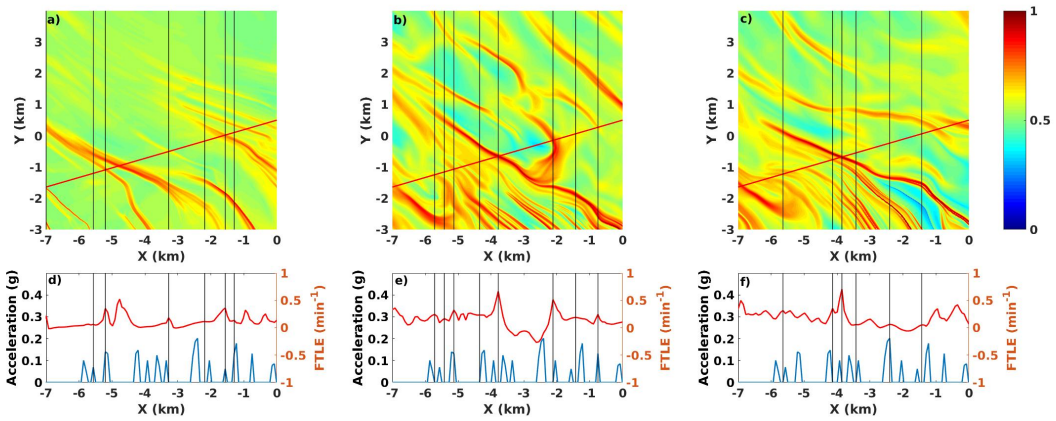

Figure 31. Airplane landing data in comparison to LCS for a successful approach at 07:52:20 on 2009-02-21. (a) Approach path superimposed on backward-time LCS based on the 3° LIDAR scan. (b) Approach path superimposed on backward-time LCS computed from WRF . (c) Approach path superimposed on backward-time LCS computed from WRF, using data assimilation. (d) Comparison between positive vertical acceleration and forward-time FTLE. Vertical acceleration measured onboard the aircraft is shown in blue, with values less than 0.05g removed. The red line is the backward-time FTLE computed from the 3° LIDAR scan, interpolated along the flight path. (e) Comparison between positive vertical acceleration and backward-time FTLE, computed in WRF. (f) Comparison between positive vertical acceleration and backward-time FTLE, computed in WRF, using data assimilation. The black vertical lines highlight locations where LCS are correlated with vertical acceleration. The origin corresponds to the northern LIDAR.

4.5.2 2009-02-21

In Figure 31 we show the backward-time LCS for a successful landing at around 07:52:20, using the 3° scanning angle. The panel organization is the same as the above. Note that at this time airplanes are landing on the northern runway from the opposite direction as the cases discussed above. Results analogous to those discussed above are seen on this day as well; we note again the general mis-alignment of the LCS structures in the base WRF LCS. After data assimilation, we see a good qualitative agreement between the LIDAR extracted LCS and the WRF generated LCS. However,

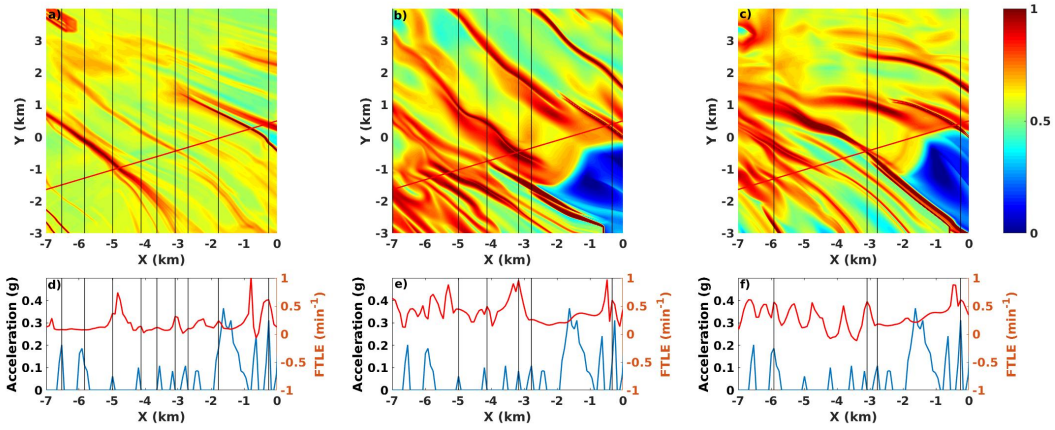

Figure 32. Airplane landing data in comparison to LCS for a missed approach at 08:37:40 on 2009-02-21. (a) Approach path superimposed on backward-time LCS based on the 1.4° LIDAR scan. (b) Approach path superimposed on backward-time LCS computed from WRF . (c) Approach path superimposed on backward-time LCS computed from WRF, using data assimilation. (d) Comparison between positive vertical acceleration and backward-time FTLE. Vertical acceleration measured onboard the aircraft is shown in blue, with values less than 0.05g removed. The red line is the backward-time FTLE computed from the 1.4° LIDAR scan, interpolated along the flight path. (e) Comparison between positive vertical acceleration and backward-time FTLE, computed in WRF. (f) Comparison between positive vertical acceleration and backward-time FTLE, computed in WRF, using data assimilation. The black vertical lines highlight locations where LCS are correlated with vertical acceleration. The origin corresponds to the northern LIDAR.

in panel (a) we see that the structures starting at the points $(-4, -3)$ and $(-2, -3)$ collapse together at roughly $(-6, -0.5)$, however in panel (c) we do not get the same intersection in the data assimilation structures. There is a good agreement in the structures that start at $(-2, -3)$. There is a faint streak starting at $(-1, -3)$ in panel (c) that corresponds to a much stronger signature originating at the same point in panel (a).

In Figure 32 we show the backward-time LCS for an aborted landing at around 08:37:40, with the same panel layout as before. We use the 1.4° LIDAR for this flight. As before, we see a good general qualitative agreement between the LIDAR LCS in

panel (a) and the post data assimilation WRF LCS in panel (c). There is a ridge in panel (c) starting at $(0, -3)$ that shows a good correspondence to the structure in panel (a) starting at roughly the same point, although the ridge is fainter as it approaches that point. Note that in panel (a) there is another structure, starting at about $(-1, -3)$ that comes very close to the aforementioned structure at about the point $(-2, -2)$, however in panel (c) the two corresponding structures do not converge. We also see generally good qualitative agreement in structures starting at the points $(-2, -3)$, $(-3, -3)$, and $(-4, -3)$. We also see that there are a lot more structures to the left of $x = -5$ in panel (c) than there are in panel (a) - there appear to be some streaks that may match, but such a correspondence may be happenstance. We again note the direction mismatch in the base WRF panel (b).

Due to the more involved LCS, making any direct comparison with the airplane jolts more tenuous in panels (d) through (f) than in the previous cases. We can see that the two jolts identified by the LIDAR in panel (d) at around $x = -6.75$ and $x = -6$ are identified fairly weakly, whereas in panel (f) one jolt is not within 150 m of any FTLE peak in WRF. However, between $x = -7$ and $x = -3$ the WRF LCS in panel (f) would be interpreted as predicting a jolt filled landing, even if the peaks are not within the threshold, which is probably a better qualitative match as compared the what the LIDAR LCS would predict in panel (d). It is worthwhile to note that the major jolt experienced at $x = -1.75$ is not technically correlated with an FTLE peak in panel (f), but a peak, very similar to the identifying peak from LIDAR in panel (d), is just outside the 150 m range.

In Figures 33 and 34 we show the corresponding forward-time structures for these two flights. We first note that in panel (a) of both figures we generally see less complex LCS than in the corresponding backward-time cases. This is most likely due to the

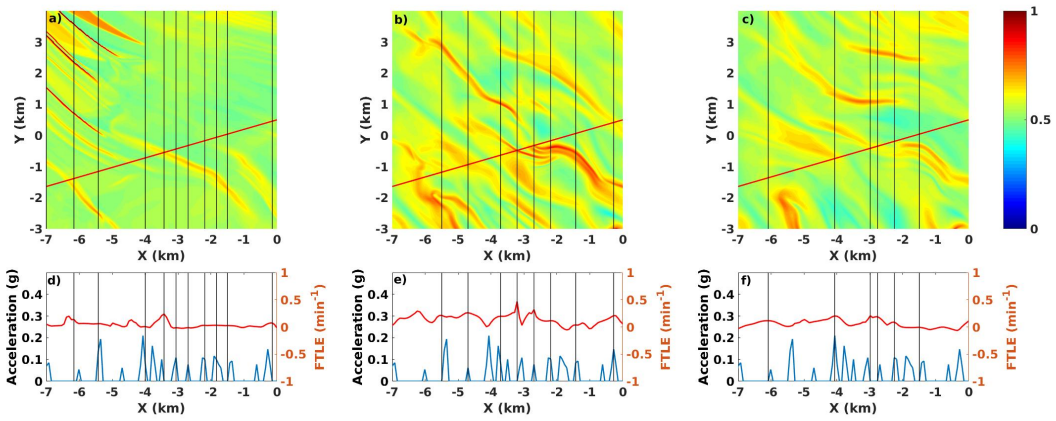

Figure 33. Airplane landing data in comparison to LCS for a missed approach at 07:52:20 on 2009-02-21. (a) Approach path superimposed on forward-time LCS based on the 3° LIDAR scan. (b) Approach path superimposed on forward-time LCS computed from WRF . (c) Approach path superimposed on forward-time LCS computed from WRF, using data assimilation. (d) Comparison between negative vertical acceleration and forward-time FTLE. Vertical acceleration measured onboard the aircraft is shown in blue, with values less than -0.05g removed. The red line is the forward-time FTLE computed from the 3° LIDAR scan, interpolated along the flight path. (e) Comparison between negative vertical acceleration and forward-time FTLE, computed in WRF. (f) Comparison between negative vertical acceleration and forward-time FTLE, computed in WRF, using data assimilation. The black vertical lines highlight locations where LCS are correlated with vertical acceleration. The origin corresponds to the northern LIDAR. Note that the vertical acceleration shown as been multiplied by -1.

fact that, due to the incoming flight direction, we are near to the edge of the LIDAR range - since the flow is coming from the southeast, the forward-time flow is relatively quickly carried away from the LIDAR velocity, and to the linear background flow. Interestingly, there is not much correlation in panels (a) and (c) in Figure 33, the data assimilation did not particularly make a significant improvement over the base WRF LCS seen in panel (b). There is a slightly better correlation in Figure 34, where we see in a panel (a) a structure starting at $(-0.5, -3)$ that has a corresponding structure in panel (c). However, the hairpin like structure in panel (a) found at $(-4.75, -3)$ has no corresponding structure in panel (c), although perhaps the left branch is visible.

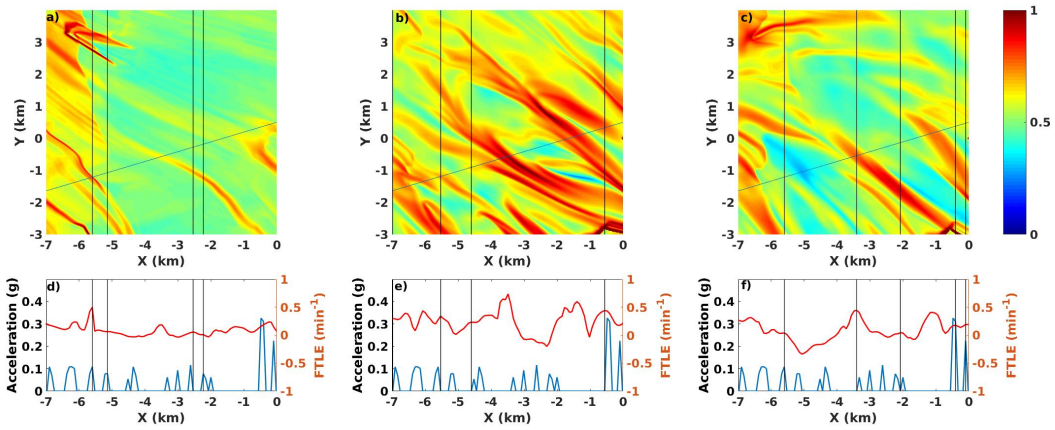

Figure 34. Airplane landing data in comparison to LCS for a missed approach at 08:37:40 on 2009-02-21. (a) Approach path superimposed on forward-time LCS based on the 1.4° LIDAR scan. (b) Approach path superimposed on forward-time LCS computed from WRF . (c) Approach path superimposed on forward-time LCS computed from WRF, using data assimilation. (d) Comparison between negative vertical acceleration and forward-time FTLE. Vertical acceleration measured onboard the aircraft is shown in blue, with values less than -0.05g removed. The red line is the forward-time FTLE computed from the 1.4° LIDAR scan, interpolated along the flight path. (e) Comparison between negative vertical acceleration and forward-time FTLE, computed in WRF. (f) Comparison between negative vertical acceleration and forward-time FTLE, computed in WRF, using data assimilation. The black vertical lines highlight locations where LCS are correlated with vertical acceleration. The origin corresponds to the northern LIDAR. Note that the vertical acceleration shown as been multiplied by -1.

Comparing the jolts in panels (d) and (f) in Figure 33, we see that many of the LIDAR correlations are for very very weak FTLE peaks, and so although there are more correlations in panel (d) as compared to panel (f), some of these may be due entirely to noise. This is similar in Figure 34.

4.6 Conclusion

We have performed data assimilation using LIDAR line of sight velocity into WRF using 3DVAR. We found that the LIDAR data from different scanning angles can be consistently incorporated into WRF and found that WRF can be cycled successfully with those observations. The improvements to the base WRF forecast made at a given time with a given scanning angle carried over at the next time and resulted in a better background forecast at the next time, using the other scanning angle. This is significant in the sense that all the available LIDAR information can be used to improve the forecast.

We made a LCS comparison between LIDAR, WRF, and WRF using data assimilation, and found that the data assimilation resulted in generally a good qualitative agreement in LCS structures between WRF and LIDAR. The base WRF LCS were found to be consistently mis-aligned. We compared to onboard flight data, and found that after data assimilation the peaks in the WRF LCS, interpolated along the airplane landing path, showed a very good general agreement with vertical accelerations, giving an overall better qualitative match as compared to LIDAR alone. This suggests the potential of using LIDAR observations and WRF together to predict windshear events. In general, the backward-time LCS showed a better correspondence as compared to the forward-time LCS. This suggests that in any operational implementation different assimilation schemes may need to be implemented for each case; in other words, two different runs of 3DVAR at each given observation time, one to extract forward-time LCS, one to extract backward-time LCS.

There are different possible future applications for using these results to improve real time windshear detection. First, there is the possibility of using WRF to predict

windshear events ahead of time. Obviously computational cost and time would be an issue that would need to be considered for feasibility. As a second possibility, using data assimilation and WRF we now have full three-dimensional wind data that would generate the LIDAR observations, data that has much more information than any three-dimensional variational retrieval scheme could hope to recreate. Generating a multitude of such datasets, and using pattern recognition techniques, one could possibly train a program to analyze two-dimensional LIDAR LCS to infer the underlying three-dimensional structures, as done in (Tang, Chan, and Haller 2011a), which can then identify any possible windshear events along the landing corridor.

Chapter 5

CONCLUSION

We have used Lagrangian coherent structures (LCS) to study the transport of inertial pollutant particles in an urban setting and to further study windshear detection at the Hong Kong International Airport (HKIA).

In Chapter 2 we found that the stochastic inertial Lagrangian coherent structures (ILCS) survive realistic disturbances, in the form of eddy diffusivity, indicating that they likely serve to organize pollutant transport in the natural environment. The ILCS therefore identify key structures which decision makers could use to find regions that are most susceptible to the dispersion or accumulation of pollutants, and the identification of such regions would be of aid in the development of any air quality counter measures devised for real life release events. As discussed in the conclusion to Chapter 2, much further work could be done here, from a more careful formulation of the stochastic differential equation modeling the movement of inertial particles, to case studies illustrating the direction application of the ideas developed.

Chapter 3 served to validate the promising Lagrangian based turbulent structure extraction methods near the Hong Kong International airport first introduced in (Tang, Chan, and Haller 2011a, 2011b), a neccesary check due to the fundamentally large loss of flow information inherent in the LIDAR scans. After comparing three numerical wind models, FLOWSTAR, RAMS, and WRF, we found that the WRF model best matched the LIDAR extracted LCS.

Therefore, in chapter 4 we used data assimilation to incorporate the LIDAR observations into the WRF forecast. This resulted in an improved forecast that yielded

LCS that closely matched the LIDAR extracted LCS, and generally outperformed the LIDAR extracted LCS in terms of agreement with onboard flight measurements. This provides a promising hope for using WRF and the LIDAR observations together to predict windshear events along the landing corridor in real-time, or, to use the improved full three-dimensional WRF forecasts to further refine the Lagrangian extraction methods, in terms of trying to better identify the flow regimes where false positives and false negatives could occur. Although the work done here was at HKIA, it is readily applicable and generalizable to any airfield that experiences terrain induced turbulence.

REFERENCES

Arnfield, A.J. 2003. "Two decades of urban climate research: a review of turbulence, exchange of energy and water, and the urban heat island." *Int. J. Climatol* 24:1–26.

Auton, T.R., J.C.R. Hunt, and M. Prud'Homme. 1988. "The force exerted on a body in invisid unsteady non-uniform rotational flow." *J. Fluid Mech.* 197:241–257.

Avissar, R., and R.A. Pielke. 1989. "A parameterization of heterogeneous land surfaces for atmospheric numerical models and its impact on regional meteorology." *Mon. Weather Rev.* 117:2113–2136.

B.Singh, B. Hansen, M. Brown, and E. Pardyjak. 2008. "Evaluation of the QUIC-URB fast response urban wind model for a cubical building array and wide building street canyon." *Environ. Fluid Mech.* 8:281–312.

Babiano, A., J.H.E. Cartwright, O. Piro, and A. Provenzale. 2000. "Dynamics of a small neutrally buoyant sphere in a fluid and targeting in Hamiltonian systems." *Phys. Rev. Lett.* 84:5764–5767.

Barker, D., X.-Y. Huang, Z. Liu, T. Auligne, X. Zhang, S. Rugg, A. Ajjaji, et al. 2012. "The Weather Research and Forecasting Model's Community Variational/Ensemble Data Assimilation System: WRFDA." *Bull. Amer. Meteor. Soc.* 93:831–843.

Barker, D.M., W. Huang, Y.-R. Guo, and Q.N. Xiao. 2004. "A Three-Dimensional (3DVAR) Data Assimilation System For Use with MM5: Implementation and Initial Results." *Mon. Wea. Rev.* 132:897–914.

Belcher, S.E. 2005. "Mixing and transport in urban areas." *Philos. Trans. R. Soc. London, Ser. A* 363:2947–2968.

Benczik, I.J., Z. Toroczkai, and T. Tel. 2002. "Selective sensitivity of open chaotic flows on inertial tracer advection: Catching particles with a stick." *Phys. Rev. Letter.* 89.

Blazevski, Daniel, and George Haller. 2014. "Hyperbolic and Elliptic Transport Barriers in Three-Dimensional Unsteady Flows." *Physica D.*

BozorgMagham, A.E., S.D. Ross, and Schmale I. 2013. "Real-time prediction of atmospheric Lagrangian coherent structures based on forecast data: an application and error analysis." *Physica D: Nonlinear Phenomena* 258:47–60.

Britter, R.E., and S.R. Hanna. 2003. "Flow and dispersion in urban areas." *Annu. Rev. Fluid Mech.* 42:469–496.

Carruthers, D.J., A. Ellis, J.C.R. Hunt, and P.W. Chan. 2014. "Modeling of wind shear downwind of mountain ridges at Hong Kong international airport." *Meteorological Applications* 21:94–104.

Carruthers, D.J., J.C.R. Hunt, and W.S. Weng. 1988. *A computational model of stratified turbulent airflow over hills - flowstar I.* 481–492. Springer.

Chan, P.W. 2012. "A significant wind shear event leading to aircraft diversion at the Hong Kong international airport." *Meteorological Applications* 19:10–16.

Chan, P.W., and Y.F. Lee. 2012. "Application of short-range lidar in wind shear alerting." *Journal of Atmospheric and Oceanic Technology* 29:207–220.

Chan, P.W., and A.M. Shao. 2007. "Depiction of complex airflow near Hong Kong International Airport using a Doppler LIDAR with a two-dimensional wind retrieval technique." *Meteorologische Zeitschrift* 16:491–504.

Chan, P.W., C.M. Shun, and K.C. Wu. 2006. *Operational lidar-based system for automatic windshear alerting at the Hong Kong international airport.* American Meteorological Society.

Choi, Yonghan, Gyu-Ho Lim, and Dong-Kyou Lee. 2013. "Radar Radial Wind Data Assimilation Using the Time-Incremental 4D-Var Method Implemented to the WRFDA System." *Tellus A* 65.

Chong, M.S., A.E. Perry, and B.J. Cantwell. 1990. "A general classification of three-dimensional flow field." *Phys. Fluids A* 2:765–777.

Civerolo, K.L., G. Sistla, S.T. Rao, and D.J. Nowak. 2000. "The effects of land use in meteorological modeling: implications for assessment for future air quality scenarios." *Atmos. Environ.* 34:1615–1621.

Csanady, G.T. 1963. "Turbulent diffusion of heavy particles in the atmosphere." *J. Atmos. Sci.* 20:201–208.

Druzhinin, O.A. 1995. "On the two-way interaction in two-dimensional particle-laden flows: the accumulation of particles and flow modification." *J. Fluid Mech.* 297:49–76.

Farazmand, M., and G. Haller. 2012. "Computing Lagrangian coherent structures from their variational theory." *Chaos* 22.

Fawcett, T. 2006. "An introduction to ROC analysis." *Pattern Recognition Letters* 27:861–874.

Fernando, H.J.S. 2010. "Fluid dynamics of urban atmospheres in complex terrain." *Annu. Rev. Fluid Mech.* 42:365–389.

Fernando, H.J.S., D. Zajic, S. Di Sabatino, R. Dimitrova, B. Hedquist, and A. Dallman. 2010. "Flow, turbulence, and pollutant dispersion in urban atmospheres." *Phys. Fluids* 22.

Ferry, J., and S. Balachandar. 2001. "A fast Eulerian method for disperse two-phase flow." *Int. J. Multiphase Flow* 27:1199–1226.

Flesch, T.K., J.D. Wilson, and E. Yee. 1995. "Backward-time Lagrangian stochastic dispersion models and their applications to estimate gaseous emissions." *J. Appl. Meteorol.* 34:1320–1332.

Gonzalez, R.C., and R.E. Woods. 2007. *Digital Image Processing.* Prentice Hall.

Hadjighasem, A., M. Farazmand, D. Blazevski, G. Froyland, and G. Haller. 2017. "A critical comparison of Lagrangian methods for coherent structure detection." *Chaos.*

Haller, G. 2000. "Finding finite-time invariant manifolds in two-dimensional velocity fields." *Chaos* 10:99–108.

———. 2001. "Distinguished material surfaces and coherent structures in 3D fluid flows." *Physica D* 149:248–277.

———. 2005. "An objective definition of a vortex." *J. Fluid Mech.* 525:1–26.

———. 2011. "A variational theory of hyperbolic Lagrangian coherent structures." *Physica D* 240:574–598.

Haller, G., and T. Sapsis. 2008. "Where do inertial particles go in fluid flows." *Physcia D* 237(5):573–583.

Haller, G., and G. Yuan. 2000. "Lagrangian coherent structures and mixing in two-dimensional turbulence." *Physica D* 147:352–370.

Haller, George. 2010. "A variational theory of hyperbolic Lagrangian Coherent Structures." *Physica D.*

Haller, George. 2013. "Do Finite-Size Lyapunov Exponents Detect Coherent Structures?" *Chaos.*

Haller, George, and Francisco J. Beron-Vera. 2012. "Geodesic theory of transport barriers in two-dimensional flows." *Physica D.*

Huang, Xiang-Yu, Xiao Qingnong, Dale M. Barker, Xin Zhang, John Michalakes, Wei Huang, Tom Henderson, et al. 2009. "Four-Dimensional Variational Data Assimilation for WRF: Formulation and Preliminary Results." *Monthly Weather Review* 137:299–314.

Jeong, J., and F. Hussain. 1995. "On the identification of a vortex." *J. Fluid Mech.* 285:69–94.

Kafiabad, H.A., P.W. Chan, and G. Haller. 2013. "Lagrangian detection of wind shear for landing aircraft." *Journal of Atmospheric and Oceanic Technology* 30:2808–2819.

Kalnay, E., and M. Cai. 2003. "Impact of urbanization and land-use change on climate." *Nature (London)* 423:528–531.

Kastner-Klein, P., R. Berkowicz, and R. Britter. 2004. "The influence of street architecture on flow and dispersion in street canyons." *Meteorol. Atmos. Phys.* 87:121–131.

Kim, J.J., and J.J. Baik. 2001. "Urban Street-canyon flows with bottom heating." *Atmos. Environ.* 35:3395–3404.

———. 2004. "A numerical study of the effects of ambient wind direction on flow and dispersion in urban street canyons using the RNG k-ϵ turbulence model." *Atmos. Environ.* 38:3039–3048.

Knutson, B., W. Tang, and P.W. Chan. 2015. "Lagrangian Coherent Structure Analysis of Terminal Winds: Three-Dimensionality, Intramodel Variations, and Flight Analyses." *Advances in Meteorology.*

Mancho, Ana M., Stephen Wiggins, Jezabel Curbelo, and Carolina Mendoza. 2013. "Lagrangian descriptors: a method for revealing phase space structures of general time dependent dynamical systems." *Communications in Nonlinear Science and Numerical Simulation.*

Maxey, M.R. 1987. "The motion of small spherical particles in a cellular flow field." *Phys. Fluids* 30:1915–1928.

Maxey, M.R., and J.J. Riley. 1983. "Equation of motion for a small rigid sphere in a nonuniform flow." *Phys. Fluids* 26:883–889.

Mograbi, E., and E. Bar-ziv. 2006. "On the asymptotic solution of the Maxey-Riley equation." *Phys. Fluids* 18.

Okubo, A. 1970. "Horizontal dispersion of floatable trajectories in the vicinity of velocity singularities such as convergencies." *Deep-Sea Res.* 17:445–454.

Olcay, A.B., T.S. Pottebaum, and P.S. Krueger. 2010. "Sensitivity of Lagrangian coherent structure identification to flow field resolution and random errors." *Chaos* 20.

Pardyjak, E.R., and M.J. Brown. 2001. *Evaluation of a fast response urban wind model - Comparison to single building wind tunnel data.* Vol. No. LA-UR-01-4028. Los Alamos National Laboratory Report.

Pielke, R.A., W.R. Cotton, and R.L. Walko. 1992. "A comprehensive meteorological modeling system - RAMS." *Meteorology and Atmospheric Physics* 49:69–91.

Qiu, C.J., A.M. Shao, S. Liu, and Q. Xu. 2006. "A two-step variational method for three-dimensional wind retrieval from a single Doppler radar." *Meteorology and Atmospheric Physics* 91:1–8.

Qui, C-J., and Q. Xu. 1992. "A simple adjoint method of wind analysis for single-Doppler data." *Journal of Atmospheric and Oceanic Technology* 9:588–598.

Rockle, R. 1990. "Bestimmung der Stomungsverhaltnisse im Bereich komplexer Bebauungsstrukturen." *Vom Fachbereich Mechanik, der Technischen Hochschule Darmstadt* Ph.D. Dissertation.

Rodean, H.C. 1996. *Stochastic Lagrangian Models for Turbulent Diffusion.* American Meteorological Society.

Sapsis, T., and G. Haller. 2008. "Instabilities in the dynamics of neutrally buoyant particles." *Phys. Fluids* 20.

———. 2009. "Inertial particle dynamics in a hurricane." *J. Atmos. Sci.* 66:2481–2492.

Sapsis, T., N.T. Ouellette, J.P. Golub, and G. Haller. 2011. "Neutrally bouyant particle dynamics in fluid flows: Comparison of experiments with Lagrangian stochastic models." *Phys. Fluids* 23.

Sapsis, T., J. Peng, and G. Haller. 2011. "Instabilities of prey dynamics in jellyfish feeding." *Bull. Math Biol.* 73:1841–1856.

Sawford, B.L., and F.M. Guest. 1991. "Lagrangian statistical simulations of the turbulent motion of heavy particles." *Boundary-Layer Meteorol.* 54:147–166.

Sela, J.G. 1980. "Spectral modeling at the national meteorological center." *Monthly Weather Review* 108:1279–1292.

Shun, C.M., and P.W. Chan. 2008. "Applications of an Infrared Doppler Lidar in Detection of Wind Shear." *Journal of Atmospheric and Oceanic Technology* 25:637–655.

Shun, C.M., and S.Y. Lau. 2002. "Implementation of a Doppler Light Detection and Ranging (LIDAR) System for the Hong Kong International Airport." *10th Conference on Aviation, Range and Aerospace Meteorology of the American Meteorological Society (AMS), Portland, Oregon.*

Sini, J.F., S. Anquetin, and P.G. Mestayer. 1996. "Pollutant dispersion and thermal effects in urban street canyons." *Atmos. Environ.* 30:2659–2677.

Skamarock, W.C., and J.B. Klemp. 2008. "A time-split nonhydrostatic atmospheric model for weather research and forecasting applications." *Journal of Computational Physics* 227:3465–3485.

Smith, F.B. 1957. "The diffusion of smoke from a continuous elevated point-source into a turbulent atmosphere." *J. Fluid Mech.* 2:49–76.

Sun, J., D. Flicker, and D. Lilly. 1991. "Recovery of three dimensional wind and temperature fields from simulated Doppler radar data." *Journal of the Atmospheric Sciences* 48:876–890.

Tallapragada, P., S.D. Ross, and D.G. Schmale. 2011. "Lagrangian coherent structures are associated with fluctuations in airborne microbial populations." *Chaos* 21.

Tang, W., P.W. Chan, and G. Haller. 2010. "Accurate extraction of LCS over finite domains, with applications to flight data analyses over Hong Kong International Airport." *Chaos* 20.

———. 2011a. "Lagrangian coherent structure analysis of terminal winds detected by lidar. Part I. Turbulence structures." *Journal of Applied Meteorology and Climatology* 50:325–338.

Tang, W., P.W. Chan, and G. Haller. 2011b. "Lagrangian coherent structure analysis of terminal winds detected by lidar. Part II. Structure evolution and comparison with flight data." *Journal of Applied Meteorology and Climatology* 50:2167–2183.

Tang, W., G. Haller, J.J. Baik, and Y.H. Ryu. 2009. "Locating an atmospheric contamination source using slow manifolds." *Phys. Fluids* 21.

Tang, W., B. Knutson, A. Mahalov, and R. Dimitrova. 2012. "The geometry of inertial particle mixing in urban flows, from deterministic and random displacement models." *Physics of Fluids.*

Tang, W., J. Taylor, and A. Mahalov. 2010. "Lagrangian dynamics in stochastic inertial-gravity waves." *Phys. Fluids* 22.

Thomson, D.J. 1987. "Criteria for the selection of stochastic models of particle trajectories in turbulent flows." *J. Fluid Mech.* 180:529–556.

Wang, Hongli, Juanzhen Sun, Xin Zhang, Xiang-Yu Huang, and Thomas Auligne. 2013. "Radar Data Assimilation with WRF 4D-Var. Part I: System Development and Preliminary Testing." *Monthly Weather Review* 141:2224–2244.

Weiss, J. 1991. "The dynamics of enstrophy transfer in 2-dimensional hydrodynamics." *Physica D* 48:273–294.

Williams, M.D., M.J. Brown, B. Singh, and D. Boswell. 2004. *QUIC-PLUME Theory Guide.* Vol. No. LA-UR-04-0561. Los Alamos National Laboratory Report.

Wilson, J.D., and B.L. Sawford. 1996. "Review of Lagrangian stochastic models for trajectories in the turbulent atmosphere." *Boundary-Layer Meteorol.* 78:191–210.

Wilson, J.D., and E. Yee. 2007. "A critical examination of the random displacement model of turbulent diffusion." *Boundary-Layer Meteorol.* 125:399–416.

Xiao, Qingnong, Ying-Hwa Kuo, Juanzhen Sun, Wen-Chau Lee, Eunha Lim, Yong-Run Guo, and Dale M. Barker. 2005. "Assimilation of Doppler Radar Observations with a Regional 3DVAR System: Impact of Doppler Velocities on Forecasts of a Heavy Rainfall Case." *Journal of Applied Meteorology* 44:768–788.

APPENDIX A

PERMISSION FORM

All the co-authors of the papers adapted for Chapters 2 and 3 have given their permission for their use.